



저작자표시-비영리-변경금지 2.0 대한민국

이용자는 아래의 조건을 따르는 경우에 한하여 자유롭게

- 이 저작물을 복제, 배포, 전송, 전시, 공연 및 방송할 수 있습니다.

다음과 같은 조건을 따라야 합니다:



저작자표시. 귀하는 원저작자를 표시하여야 합니다.



비영리. 귀하는 이 저작물을 영리 목적으로 이용할 수 없습니다.



변경금지. 귀하는 이 저작물을 개작, 변형 또는 가공할 수 없습니다.

- 귀하는, 이 저작물의 재이용이나 배포의 경우, 이 저작물에 적용된 이용허락조건을 명확하게 나타내어야 합니다.
- 저작권자로부터 별도의 허가를 받으면 이러한 조건들은 적용되지 않습니다.

저작권법에 따른 이용자의 권리는 위의 내용에 의하여 영향을 받지 않습니다.

이것은 [이용허락규약\(Legal Code\)](#)을 이해하기 쉽게 요약한 것입니다.

[Disclaimer](#)

공학박사 학위논문

**Development of Radioluminescent Liposomal
Nanoplatfrom for Radioisotope Induced
Photodynamic Therapy**

방사성 동위원소 유도 광역학 치료를 위한 방사성
발광 리포솜 나노플랫폼 개발

2022년 1월

서울대학교 융합과학기술대학원

융합과학부 방사선융합의생명전공

이우승

Development of Radioluminescent Liposomal Nanoplatfrom for Radioisotope Induced Photodynamic Therapy

지도 교수 임형준

이 논문을 공학박사 학위논문으로 제출함
2022년 1월

서울대학교 융합과학기술대학원

융합과학부 방사선융합의생명전공

이우승

이우승의 공학박사 학위논문을 인준함
2022년 1월

위 원 장 박 원 철 (인)

부위원장 임 형 준 (인)

위 원 이 학 중 (인)

위 원 이 강 원 (인)

위 원 손 상 준 (인)

Abstract

Development of Radioluminescent Liposomal Nanoplatfrom for Radioisotope Induced Photodynamic Therapy

Wooseung Lee

Program in Biomedical Radiation Sciences

Graduate School of Convergence Science and Technology

Seoul National University

Photodynamic therapy (PDT) is an effective anti-cancer strategy with a higher selectivity and fewer adverse effects than conventional therapies and is conducted by a photosensitizer (PS) and a light which can excite the photosensitizer to remove the target tumor tissues locally through reactive oxygen species (ROS) production. However, shallow tissue penetration depth of light has hampered the widespread clinical utility of PDT. Recently, reports have indicated that Cerenkov luminescence-induced PDT may overcome the tissue penetration limitation of conventional PDT. On the contrary, the effectiveness of this method is controversial because of its low luminescence intensity.

In Part I (Chapter 2), we developed a radiolabeled DTPA chelated Eu^{3+} (Eu-DTPA) / photosensitizer (PS) loaded liposome nanoplatfrom (Eu/PS-lipo) that utilizes ionizing radiation from radioisotopes for effective in vivo imaging and radioluminescence-induced PDT. Eu-DTPA was loaded onto the liposome for the scintillation of ionizing radiation and showed an approximately seven-fold higher radioluminescence intensity than that of Eu_2O_3 nanoparticles, which are commonly

used scintillating nanoparticles. We utilized Victoria blue-BO (VBBO) as a PS and observed an efficient luminescence resonance energy transfer between Eu-DTPA and VBBO (efficiency = 0.78). Furthermore, ^{64}Cu labeled Eu lipo demonstrated a strong radioluminescence with a two-fold higher intensity than the Cerenkov luminescence from free ^{64}Cu . In our radioluminescence liposome nanoplatform, radioluminescence energy transfer (RET) showed a six-fold higher energy transfer efficiency to VBBO than Cerenkov luminescence energy transfer (CLET). ^{64}Cu labeled Eu/VBBO lipo (^{64}Cu -Eu/VBBO lipo) showed a substantial tumor uptake of up to 19.3 %ID/g by enhanced permeability and retention (EPR) effects, as revealed by in vivo positron emission tomography. Finally, the PDT using ^{64}Cu -Eu/VBBO lipo demonstrated significantly higher in vitro and in vivo therapeutic effects than Cerenkov luminescence-induced PDT using ^{64}Cu -VBBO lipo.

In Part II (Chapter 3), An improvement study was conducted to minimize damage to normal organs, which is a potential limitation of the previously developed liposome nanoplatform (^{64}Cu -Eu/VBBO lipo). A combinatorial PDT system using two types of nanoprobe was devised for effective PDT: 1) liposome nanoplatform without radioisotope (Eu/VBBO lipo) and 2) ^{177}Lu -antibodies (trastuzumab and cetuximab). The radioluminescence in the combinatorial PDT system showed an approximately 6-fold higher intensity than the Cerenkov luminescence of ^{177}Lu alone. Furthermore, the energy transfer efficiency of ^{177}Lu -induced radioluminescence from Eu^{3+} to VBBO was confirmed according to the amounts of Eu^{3+} and VBBO (maximum energy transfer efficiency = 0.48 with Eu^{3+} : 0.8 mg and VBBO: 2.56 μg). Eu/VBBO lipo and antibodies showed significant tumor uptake by passive or active targeting in a mouse cancer model based on in vivo imaging studies. In vivo PET imaging using ^{64}Cu radiolabeled Eu/VBBO lipo and Ctx showed significant tumor

uptake up to 17.1% ID/g and 25.1% ID/g by passive and active targeting, respectively. In vitro PDT effect with combinatorial PDT system showed about 3.5-fold higher than high dose of ^{177}Lu -trastuzumab treatment (67% vs. 19%). Finally in vivo PDT was performed using combinatorial PDT system. Even though in vitro studies were clearly validated, the in vivo PDT effect was insignificant. More research is warranted to find the exact cause of the difference between in vitro and in vivo experiments and to improve in vivo efficacy of this new treatment method. Although there is room for improvement in studies for effective therapeutic effects on tumors and minimization of damage to normal organs, this study envisions a great opportunity for broad clinical application of PDT by establishing the radioluminescence liposome nanoplatfrom which has high tumor targeting, and efficient energy transfer capability from radioisotopes.

Keywords: Photodynamic therapy, Radioluminescence, Scintillation, Europium, Liposome, Positron emission tomography

Student Number: 2018-38662

Abstract	i
Contents	v
Figure legends	vi

Contents

Chapter 1. Introduction	1
1.1 Photodynamic therapy (PDT)	1
1.2 Limitation of conventional PDT	6
1.3 Radition induced PDT	9
1.4 Research objectives	14
 Chapter 2. Europium-DTPA Loaded Radioluminescence Liposome Nanoplatform for Effective Radioisotope-Mediated Photodynamic Therapy	 16
2.1 Background	16
2.2 Experimental method	19
2.3 Results and discussion	27
2.4 Summary	57
 Chapter 3. Photodynamic Therapy Induced by a Combination of Scintillating Liposome and Radiolabeled Antibody	 58
3.1 Background	58
3.2 Experimental method	62
3.3 Results and discussion	71
3.4 Summary	96
 Chapter 4. Conclusion	 97
References	100
 Abstract in Korean	 114

Figure legends

Figure 1.1 Treatment process of photodynamic therapy (PDT).	1
Figure 1.2 Physical mechanism of ROS from photosensitizer (reproduced from Hwang, et al.).	2
Figure 1.3 PDT photosensitizer approval timeline for cancer indications (reproduced from Li, et al.).	3
Figure 1.4 Recent results from clinical trials using photosensitizers (reproduced from Park, et al.).	4
Figure 1.5 Applications and advantages of PDT.	5
Figure 1.6 Generation of photosensitizers (reproduced from Lucas, et al.).	7
Figure 1.7 Penetration depths comparison of irradiated lights for PDT (reproduced from Gurcan, et al.).	8
Figure 1.8 Recent studies about radiation induced PDT.....	9
Figure 1.9 Recent studies of radiation induced PDT.	10
Figure 1.10 Radioactive decay of radioisotope	11
Figure 1.11 Two representative radioisotopes for these studies.	12
Figure 2.1 Radiopharmaceutical-excited fluorescence imaging (REFI) by utilizing Eu_2O_3	17
Figure 2.2 Schematic diagram of Eu/PS loaded radioluminescence liposome nanoplatfrom synthesis and experimental design.....	28
Figure 2.3 Stability test of nanoparticles under various physiological conditions (PBS, human serum, and cell media (RPMI 1640). No visible aggregates of the liposomes were observed in all 3 solutions.....	29
Figure 2.4 Characterization of Eu lipo and Eu/PS lipo.	30

Figure 2.5 Luminescence spectra between Eu^{3+} and PSs.	30
Figure 2.6 Radiolabeling efficiency of radiolabeled liposomes.	31
Figure 2.7 Radioluminescence and radioluminescence energy transfer.	32
Figure 2.8 Fluorescence images of 4 different forms of Eu included NPs.	33
Figure 2.9 Radioluminescence test with different Eu^{3+} concentrations and activities of $^{99\text{m}}\text{Tc}$	34
Figure 2.10 Radioluminescence imaging and quantitative comparison with various Eu NPs in the presence of $^{99\text{m}}\text{Tc}$ (1 mCi) ($n = 3$, mean \pm s.d.)	35
Figure 2.11 Quantitative analysis of Eu lipo by characteristic X-ray fluorescence detection with one point detector and CZT 2D imaging detector	37
Figure 2.12 Quantitative analysis of Eu lipo, VBBO lipo, and Eu/VBBO lipo by characteristic X ray fluorescence detection.	38
Figure 2.13 Quantitative comparison of RL and CL with ^{64}Cu radiolabeled liposomes under the different emission region filters	40
Figure 2.14 ROS generation test with $^{99\text{m}}\text{Tc}$	41
Figure 2.15 ROS generation test and in vitro radioisotope-induced photodynamic therapy.	44
Figure 2.16 In vivo PET imaging and quantitative analysis for assessment of passive targeting efficiency of ^{64}Cu -Eu/VBBO lipo	46
Figure 2.17 In vivo PET imaging for blood pool circulation and passive targeting efficiency of ^{64}Cu -VBBO lipo.	47
Figure 2.18 Delivery efficiency profile of various nanoparticles for in vivo targeting to the target tumor region.	49
Figure 2.19 Delivery efficiencies of the nanoparticles with or without targeting moiety.	50

Figure 2.20 In vivo photodynamic therapy.....	52
Figure 2.21 Blood test for the toxicity evaluation of the Eu/VBBO lipo.....	54
Figure 2.22 Quantitative analysis of the Eu in major organs at 2 and 14 days with ICP-MS.	55
Figure 3.1 Previous developed radiolabeled nanoplatform and biodistribution images.	59
Figure 3.2 In vivo nuclear medicine imaging of radiolabeled antibody.....	60
Figure 3.3 Schematic diagram.....	71
Figure 3.4 Hydrodynamic size measurement, stability, and radiostability tests of Eu/VBBO lipo.....	73
Figure 3.5 Radiolabeling efficiency and radiostability of Ctx.	74
Figure 3.6 In vitro specific targeting efficiencies of Tz.	77
Figure 3.7 In vitro specific targeting efficiencies of Ctx.....	78
Figure 3.8 Radioluminescence (RL) and radioluminescence energy transfer (RET) imaging of combinatorial therapeutic system.	80
Figure 3.9 In vitro ROS production imaging and effective in vitro PDT effect of combinatory therapeutic system.....	83
Figure 3.10 In vivo fluorescence imaging of Eu/VBBO lipo and Tz.....	85
Figure 3.11 In vivo fluorescence imaging of Eu/VBBO lipo and Ctx.....	87
Figure 3.12 In vivo PET imaging and quantitative analysis of ⁶⁴ Cu-Eu/VBBO lipo.	88
Figure 3.13 In vivo PET imaging and quantitative analysis of ⁶⁴ Cu-Ctx.	90
Figure 3.14 In vivo SPECT/CT imaging and quantitative analysis of ¹⁷⁷ Lu-Ctx.....	91
Figure 3.15 In vivo PDT of combinatorial PDT system.....	93

Chapter 1. Introduction

1.1 Photodynamic therapy (PDT)

Photodynamic therapy (PDT) utilizes two non-toxic components, the photosensitizer (PS) and visible light, to eliminate cancer cells. Visible light at a specific wavelength can excite PS to generate reactive oxygen species (ROS) that can kill cancer cells. PDT is in the spotlight as one of the next generation anti-cancer therapeutics because it is non-invasive, has fewer side effects, and has been proven to be effective for early stage cancer treatment^{1,2}. It is currently used in the clinic for the treatment of various types of malignant diseases, including early-stage esophageal cancer, lung cancer, head and neck cancer, and skin cancer^{3,4}. PDT in cancer treatment is mainly treated through two procedures (**Figure 1.1**)⁵.

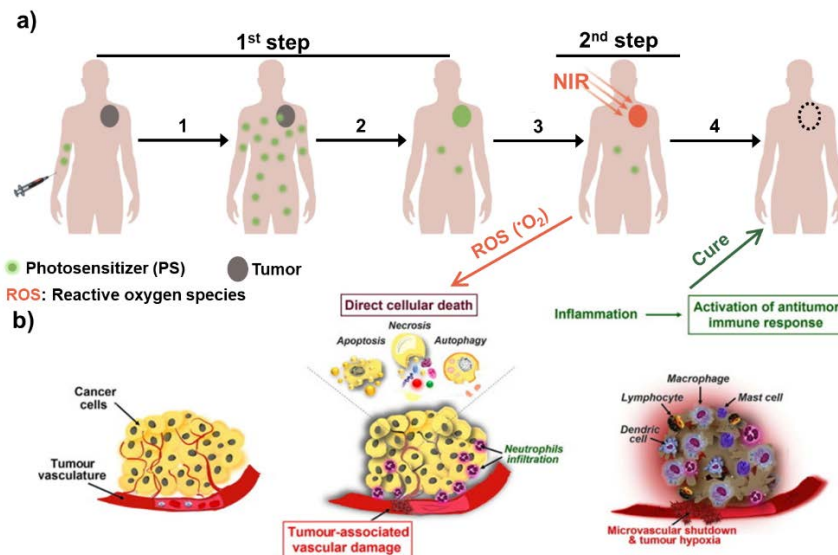


Figure 1.1 Treatment process of photodynamic therapy (PDT). a) 2-step process of PDT in the presence of photosensitizer and irradiated laser (ex. NIR laser). 1: PS administration, 2: PS accumulation to a tumor, 3: Laser irradiation, and 4: Tumor

ablation and cure (reproduced from Li, et al.). b) PDT procedure at the cellular level after treatment (reproduced from Li, et al.)⁵.

The first process refers to the target to the treatment target tumor site through in vivo injection of PS used as a PDT treatment. The next procedure refers to the process of inducing direct cell death by ROS generated from the PS by irradiating light with a specific wavelength band that the PS can absorb directly and locally on the tumor site where the PS is integrated.

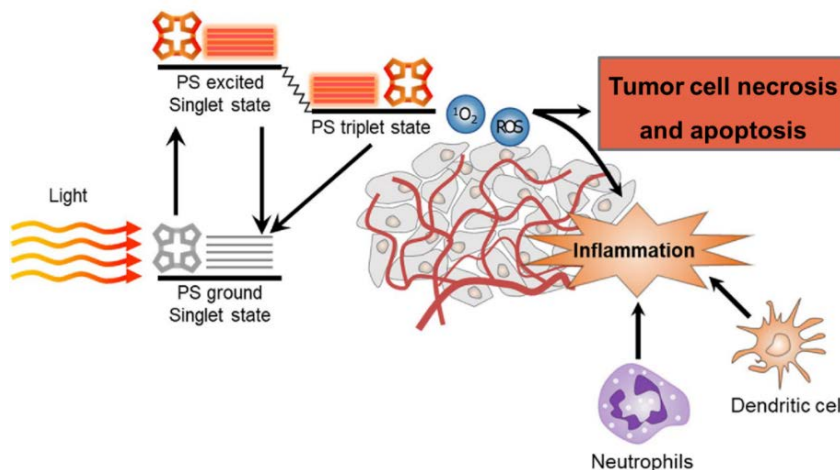


Figure 1.2 Physical mechanism of ROS from photosensitizer (reproduced from Dąbrowski, et al.)⁶.

When PS is irradiated with light energy in a wavelength band that can be absorbed, PS in the ground state is changed to an excited state. After that, the PS of the unstable excited state generates ROS in the process of going through an intermediate triplet state to return to the ground state. When this ROS generation occurs in a tumor, it

causes apoptosis or necrosis of cancer cells, and the inflammation that occurs in this process induces immune cell recruitment (**Figure 1.2**)⁶.

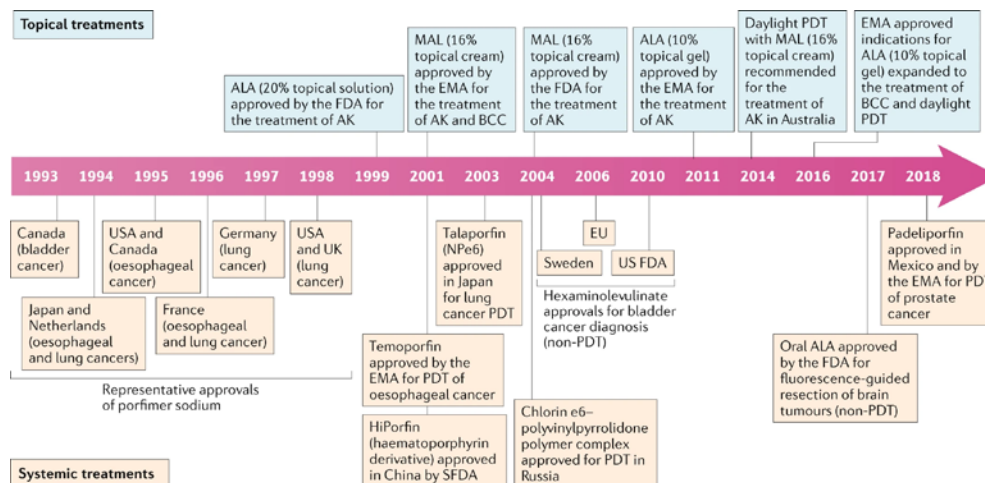


Figure 1.3 PDT photosensitizer approval timeline for cancer indications

(reproduced from Li, et al.)⁵.

PS, an essential component of PDT, has been developed for local or systemic treatment of cancer over the past 20 years (**Figure 1.3**)⁵. Several PSs such as Photofrin, Temoporfin, 5-Aminolevulinic acid (5-ALA), and Verteporfin have recently been tried in clinical trials or have been approved by the US Food and Drug Administration (FDA) as drugs for PDT (**Figure 1.4**)⁷.

Photosensitizer	Other Name (s)	Indications	Clinical Trial
Photofrin	Porfimer sodium	Esophageal cancer, endobronchial cancer, high-grade dysplasia in Barrett's esophagus	FDA-approved PDT drug
Photofrin	Porfimer sodium	Clinical trials (phases I-II) for various cancers	NCT00054002 NCT00003788 NCT00118222 NCT00322699 (Completed ¹)
Temoporfin	Foscan	Head and neck cancer	-
Temoporfin	Foscan	Clinical trials (phase II)	NCT00003856 (Unknown ²)
5-Aminolevulinic acid	5-ALA	Malignant gliomas	For the guiding agent, not therapeutics
Talaporfin	Mono-L-aspartyl chlorin e6, Laserphyrin	Lung cancer	Approved in Japan
Verteporfin	Visudyne	Age-related macular degeneration, subfoveal choroidal neovascularization	Clinical trials for macular degeneration (NCT02081339)

Figure 1.4 Recent results from clinical trials using photosensitizers (reproduced from Park, et al.)⁷.

PDT with the PS for cancer therapy has several advantages such as minimal invasiveness than surgical treatment, repeatable therapy, little or no scarring after the therapy, and cost effectiveness than other cancer therapy (**Figure 1.5 b**)⁸. PDT has also been applied in a wide range of applications, such as vascular damage and removal associated with fungi, acne, viruses, bacteria, cancer, and disease (**Figure 1.5 a**)⁹.

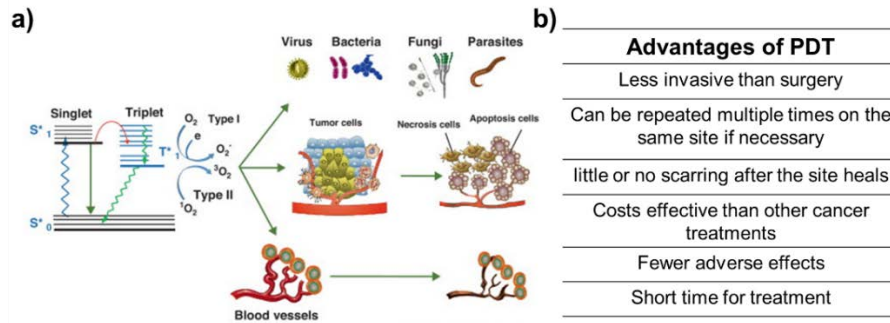


Figure 1.5 Applications and advantages of PDT. a) Various applications of PDT (reproduced from Yin, et al.)⁹. b) Several advantages of PDT (reproduced from Calixto, et al.)⁸.

1.2 Limitation of conventional PDT

PDT has two major limitations in cancer treatment: 1) the physicochemical properties of the photosensitizer and 2) the penetration depth of the light source irradiated to PS. PS has been developed in various forms depending on its physicochemical properties (**Figure 1.6**)^{10, 11}. For the 1st-generation of PS, various types of derivatives (ex. Hematoporphyrin) have been developed based on porphyrin, a family of iron ion chelating heme groups in hemoglobin. These 1st-generation PSs have problems such as severe agglomeration in aqueous solution, low selectivity to a target site, and skin photosensitivity to cause skin damage. In the case of the 2nd-generation PS, molecules that improved the low solubility problem in aqueous solution of the first-generation were developed. 2nd-generation PSs were developed in a structure in which functional groups were added to backbone molecules such as chlorin, phthalocyanine, and porphyrin to increase solubility in aqueous solutions. In addition, PS with high hydrophilicity such as 5-ALA, methylene blue, and toluidine blue are also included in the second generation. However, the second-generation PS has a disadvantage in that it has a low targeting ability to the tumor site due to rapid renal clearance after injection into the body because of its high solubility in water.

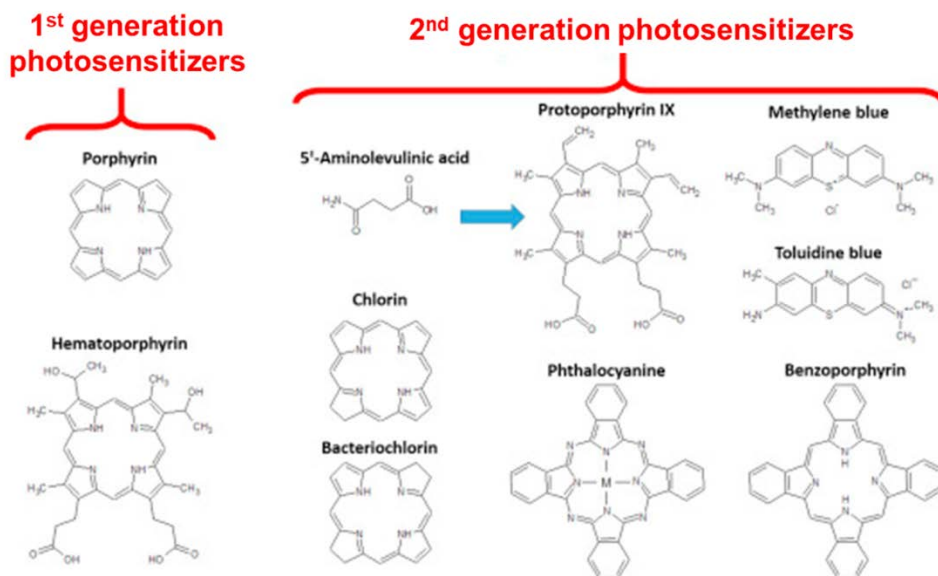


Figure 1.6 Generation of photosensitizers (reproduced from de Freitas, et al.)¹⁰.

Photodynamic therapy is not widely utilized in the clinical setting because of the limited tissue penetration depth of light and modest tumor targeting ability of PS (**Figure 1.7**)^{12, 13}. The light used for PDT mainly uses red visible light or near-infrared light for the therapeutic effect of PS injected into the body. Since the penetration depth of light used in PDT is less than 1 cm from the skin, the photodynamic therapeutic effect is insufficient for a large cancer or a cancer deep in the body.

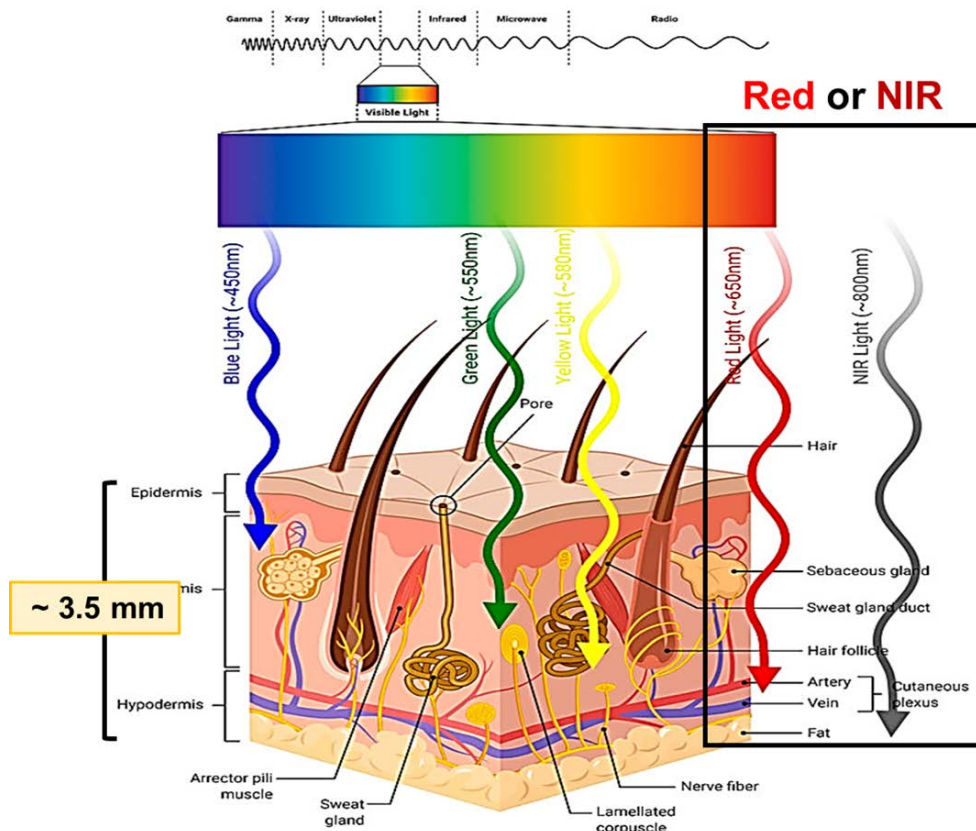


Figure 1.7 Penetration depths comparison of irradiated lights for PDT

(reproduced from Gurcan, et al.)¹³.

1.3 Radiation induced PDT

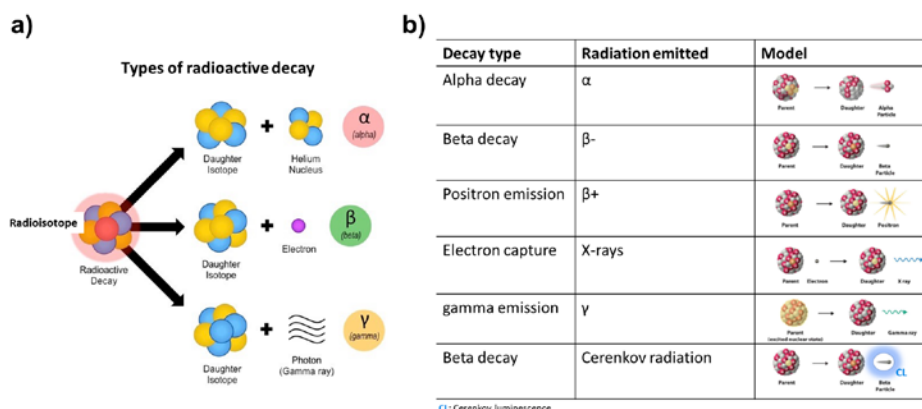


Figure 1.8 Radioactive decay of radioisotope a) Radioactive decay types of radioisotopes. b) Different types of ionizing radiations. (reproduced from chemwiki.ucdavis.edu)¹⁴.

To overcome the limitations of the tissue transmittance of irradiation light for PDT, research on radiation-induced PDT has been intensively studied in recent years.

Ionizing radiation is high energy from radioisotopes, which contains subatomic particles with sufficient energy to ionize atoms by separating electrons from atoms¹⁴. A radioisotope is an alternative form of an element on the periodic table that has the same number of protons but a different number of neutrons. The radioisotope is unstable and decays at a constant rate to form the more stable daughter isotope. During radioactive decay such as alpha, beta, and gamma decay, various forms of high-energy ionizing radiation are emitted (**Figure 1.8 a**). β^+ rays generated through positron emission decay are used for positron emission tomography (PET) imaging, and X-rays emitted by electron capture decay are used for radiation therapy or imaging. Cerenkov radiation generated through beta decay emits Cerenkov

luminescence, which is visible light only for high-energy particles (**Figure 1.8 b**)¹⁵,

¹⁶.

Radioisotope	Half life ($t_{1/2}$)	Decay Mode
⁶⁴ Cu	12.7 hours	β^+ (19%) (Positron for PET imaging) γ (43%) β^- (38%) (Therapy)
¹⁷⁷ Lu	6.65 days	γ (22%) (SPECT/CT imaging) β^- (78%) (Therapy)

Figure 1.9 Two representative radioisotopes for these studies.

In this study, two major radioisotopes, ⁶⁴Cu and ¹⁷⁷Lu, were used. ⁶⁴Cu is a radioisotope with a half-life of 12.7 hours and has the characteristics of enabling PET imaging by emitting about 19% of positrons. ¹⁷⁷Lu has a half-life of about 6.65 days, β^- rays are emitted through 78% of beta decay, and is a representative radioisotope used for treatment. It also emits 22% of gamma rays, enabling single-photon emission computerized tomography (SPECT) (**Figure 1.9**).

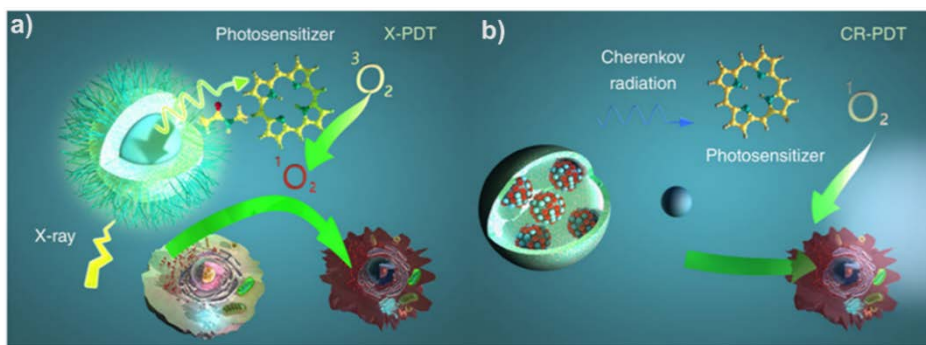


Figure 1.10 Recent studies about radiation induced PDT. a) X-ray induced PDT and b) Cerenkov luminescence induced PDT by radioisotope (reproduced from Cline, et al.)¹⁷.

Recently, X-ray induced PDT was suggested to overcome the limitation of tissue penetration depth of light (**Figure 1.10 a**)^{17, 18}. Instead of using an external visible light source, ionizing radiation can be used to generate visible light through nanoparticles (NP) containing scintillating materials, such as Europium (Eu) and Terbium (Tb)¹⁸⁻²⁰. Wang et al. demonstrated X-ray induced PDT by using the Eu doped $SrAl_2O_4$ nanoparticle (**Figure 1.11 a**)²¹. The Eu ions played a crucial role as a scintillator transferring the energy from X-ray to PS (MC540 was used as a PS for this study). Therefore, the strong luminescent effect of Eu^{3+} by radioisotopes is an essential and a major element for PS to act as a scintillator providing light energy to generate ROS. However, X-ray induced PDT may not be feasible in the clinical setting because the additional X-ray irradiation can only be applied to a limited number of lesions for a short period of time, and could be harmful to normal tissue¹⁹. The Eu doped $SrAl_2O_4$ nanoparticle invented by Wang et al. was synthesized based on solid materials such as $SrAl_2O_4$ for the core part, dense silica, and mesoporous

silica for the shell layers. Because of the utilizing these solidified materials, the study had the limitation of in vivo biosafety.

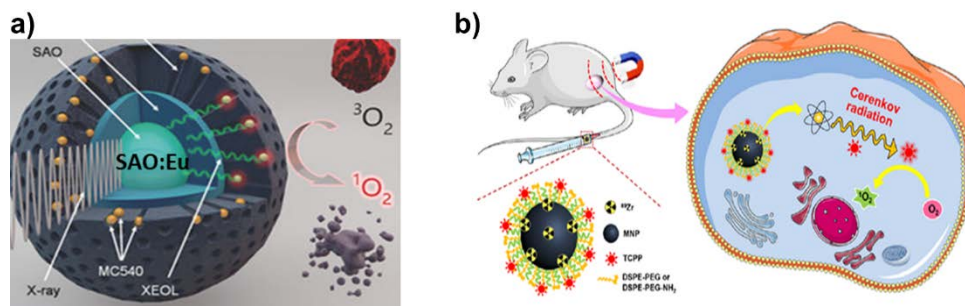


Figure 1.11 Recent studies of radiation induced PDT. a) X-ray induced PDT using radioluminescence from SAO:Eu@mSiO₂ NPs (reproduced from Wang, et al.)²¹. b) Cerenkov luminescence induced PDT using ⁸⁹Zr labeled magnetic nanoparticles (reproduced from Ni, et al.)²².

Meanwhile, Cerenkov luminescence emitted from particle radiation can also be used for induction of PDT in place of X-ray irradiation (**Figure 1.10 b**)^{17, 23-25}. This radioisotope mediated PDT has advantages over X-ray induced PDT in that it can treat multiple target lesions after intravenous injection and does not need an external beam irradiation²⁵. Recently, Ni et al. reported that Cerenkov-induced PDT using ⁸⁹Zr labeled magnetic NPs with porphyrin molecules exhibited excellent therapeutic effects (**Figure 1.11 b**)²². However, Cerenkov luminescence is very dim, thus the clinical efficacy of this method is questionable; the energy of Cerenkov luminescence from ¹⁸F comprises of less than 0.006% of the total energy released from the radioisotope²⁶. Furthermore, a broad emission wavelength of Cerenkov luminescence could be a source of ineffective energy transfer to PS²⁷. In addition, previous studies have utilized hard-core NPs for the enhancement of PDT efficacy¹⁸,

^{23, 24, 28-31}, which have the disadvantage of a low targeting efficiency that mainly stems from the non-specific interaction with serum proteins and recognition by reticuloendothelial system³². The hard-core NPs may also be toxic because they are chemically stable and difficult for lysosomes of the tissue macrophage system to digest^{33, 34}.

1.4 Research objectives

The goal of this study is to develop a nanoplatform for radiation-induced PDT using radioluminescence.

In Chapter 2, we developed a radiolabeled, Eu and PS co-loaded liposome nanoplatform for radioisotope mediated in vivo imaging and PDT with the intention of combining the advantages of X-ray- and Cerenkov-induced PDT. We tried to overcome the limitation of X-ray-induced PDT by utilizing radioisotopes as an energy source, and the dim Cerenkov luminescence intensity by adding scintillating materials. First, diethylenetriamine pentaacetic acid (DTPA) chelated Eu^{3+} (Eu-DTPA) was loaded in the liposome for scintillation of ionizing radiation. Unlike previous approaches that utilized hard-core NPs with lanthanide doping for X-ray-induced PDT, we used a liposome nanoplatform to ensure better biocompatibility³⁵.³⁶ Furthermore, PS was loaded in the lipid bilayer of the liposome and ^{64}Cu was labeled onto the surface of the liposome to induce radioluminescence from Eu-DTPA. As a result, ionizing radiation from the labeled radioisotope interacted with Eu-DTPA and produced radioluminescence, the energy of which could be transferred to the PS to produce ROS for PDT. In addition, positron, radioluminescence, and characteristic X-ray from the nanoplatform enabled multimodal imaging. The advantages of using radioluminescence over Cerenkov luminescence for PDT were then evaluated by comparing the radiolabeled PS loaded liposome nanoplatforms with and without Eu-DTPA loading.

In Chapter 3, we improved our previous radioluminescent liposome nanoplatform for more effective radioluminescence induced PDT. We demonstrated to develop a combinatorial PDT system using two nanoprobess by separating a radioisotope from

the previously studied radiolabeled nanoliposome platform (^{64}Cu -Eu/VBBO lipo). The antibody was selected as a radioisotope carrier because of its high active targeting ability on tumors and low accumulation in normal organs. Two combinatorial nanoprobe were designed as follows: 1) Eu/VBBO lipo (radioisotope-induced PDT performer) and 2) ^{177}Lu -antibody (PDT initiator). The liposome loaded with Eu^{3+} and VBBO without radiolabelling was verified by demonstrating the dispersion stability under the physiological conditions and uniformity of hydrodynamic size. The specific binding ability of trastuzumab (Tz) and cetuximab (Ctx), which were used as antibodies, was confirmed by confocal fluorescence microscopy and flow cytometry for cancer cell lines with specific overexpressed proteins for each antibody. In the combination of ^{177}Lu -labeled antibody and Eu/VBBO lipo, the same radioluminescence effect as in the radiolabeled nanoplateform of previous studies occurred and luminescence imaging was performed to determine whether energy transfer to PS is effective. Furthermore, the superiority of the two combinatorial PDT systems based on radioluminescence imaging was evaluated by comparing them with a high dose ^{177}Lu -labeled antibody through ROS generation and in vitro/in vivo studies.

Some of the contents of this introduction were excerpted from the following published paper (Lee, Woosung, et al. "Europium-diethylenetriaminepentaacetic acid loaded radioluminescence liposome nanoplateform for effective radioisotope-mediated photodynamic therapy." ACS nano 14.10 (2020): 13004-13015.).

Chapter 2. Europium-DTPA Loaded Radioluminescence Liposome Nanopatform for Effective Radioisotope- Mediated Photodynamic Therapy

2.1 Background

Europium (Eu) belongs to rare earth metals and is one of the metal elements corresponding to High-Z metals. The Eu is known as a material that emits red fluorescence (λ_{em} : 590 ~ 630 nm, λ_{max} : 615 nm) by ultraviolet rays (λ_{ex} : 300 ~ 400 nm) in the form of metal ions (Eu^{3+}) or metal oxides (Eu_2O_3). Küçük et al. conducted imaging studies in mice through the phenomenon that light emission occurs even by ionizing radiation other than ultraviolet rays (**Figure 2.1**)³⁷. In that study report, it was verified that Eu^{3+} of Eu_2O_3 mainly reacts to gamma rays to cause radioluminescence. In vivo imaging was performed for comparison between Cerenkov luminescence (CL), which is radioisotope self-luminescence by Cerenkov radiation, and radioluminescence (RL) by Eu_2O_3 . (**Figure 2.1 g**)

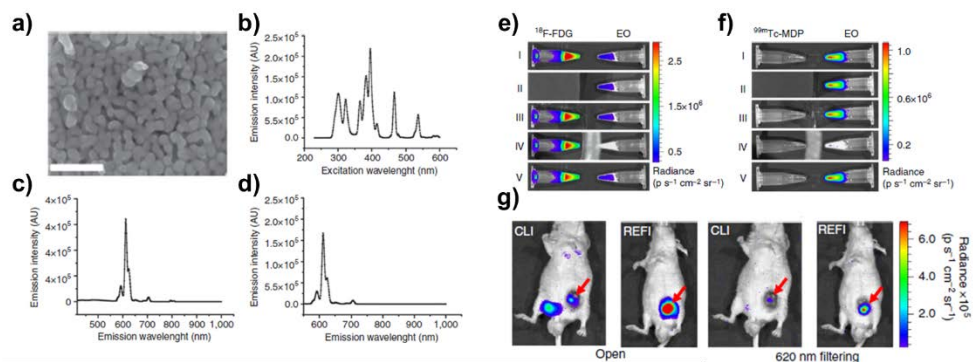


Figure 2.1 Radiopharmaceutical-excited fluorescence imaging (REFI) by utilizing Eu_2O_3 . a) SEM image of Eu_2O_3 . b) Excitation wavelength of Eu_2O_3 . c)-d) Emission spectra of Eu_2O_3 . Radioluminescence imaging with e) ^{18}F -FDG and f) $^{99\text{m}}\text{Tc}$ -MDP of Eu_2O_3 . I: Normal view, II: Black box (blocking CL), III: Al foil (blocking β^+), IV: Pb torus (blocking γ), and V: Normal view. g) Luminescence imaging comparison between CLI and REFI (Left: open filter and right: 620 nm filter) (reproduced from Küçük, et al.)³⁷.

It was demonstrated that RL has a much stronger signal than CL. Ultraviolet light (400 nm and 535 nm) in the excitation wavelength band was irradiated using Eu_2O_3 nanoparticles of about 100 nm or less (**Figure 2.1 a-b**). It was confirmed that fluorescence in the red wavelength band was emitted by the two irradiation lights (**Figure 2.1 c-d**). ^{18}F -FDG and $^{99\text{m}}\text{Tc}$ -MDP were used to determine whether Eu_2O_3 was radioactively emitted by radioisotopes (**Figure 2.1 e-f**). Specific emission of radiation was confirmed while shielding ionizing radiation emitted from each radioisotope. In the case of in vivo imaging, it was verified that RL in the combination of ^{18}F -FDG and Eu_2O_3 was superior to CL from ^{18}F -FDG. Based on this previous report, it was suggested that RL, which is stronger than CL by Eu^{3+} , is an

essential element for the development of nanoparticles for ionizing radiation-induced PDT as a scintillator that transfers energy to the photosensitizer.

Therefore, in this study, we conducted experiments on the development of a nanopatform for RL-mediated PDT using radioisotopes and the performance ability for cancer treatment. In the case of the nanopatform, development and research were conducted with a liposome-based nanoparticle structure for a high biocompatibility, cancer-targeting efficacy, and high circulation ability in vivo. Chelated Eu^{3+} for the high RL intensity and VBBO selected as a PS were co-embedded into the liposome (Eu/VBBO lipo), and spherical morphology and uniformity of the liposome was characterized. Effective RL and RL energy transfer were validated by ^{64}Cu labeling onto the surface of the Eu/VBBO lipo. ROS production and followed by in vitro PDT were further conducted based on the RL imaging study. Finally, in vivo PDT was performed with the ^{64}Cu labeled Eu/VBBO lipo to demonstrate the cancer treatment effect.

2.2 Experimental methods

2.2.1 Materials

Cholesterol, Europium chloride $\cdot 6\text{H}_2\text{O}$, Rose bengal, victo-ria blue-BO, Europium oxide ($< 150\text{ nm}$), and diethylene-triaminepentaacetic acid (DTPA) were purchased from Sigma-Aldrich (Missouri, USA). 1,2-distearoyl-sn-glycero-3-phosphocholine (DSPC) and 1,2-distearoyl-sn-glycero-3-phosphoethanolamine-N-[amino(polyethylene glycol)-2000] (DSPE-PEG(2000)-NH₂) were purchased from Avanti Polar Lipid, Inc (Alabama, USA). 1,2-distearoyl-sn-glycero-3-phosphoethanolamine (meyhoxy(polyethyleneglycol)-5000) (DSPE-mPEG(5000)) was purchased from Creative PEGWorks (North Carolina, USA). Chlorin e6 was purchased from Cayman Chemical (Michigan, USA). Dimethyl sulfoxide (DMSO) was obtained from DAEJUNG CHEMICALS & METALS Co., Ltd (Busan, Korea). 2-(p-Isothiocyanatobenzyl)-1,4,7-triazacyclononane-N,N',N'',-triacetic acid trihydrochloride ((p-SCN-Bn)-NOTA) was also purchased by FUTURECHEM (Seoul, Korea).

2.2.2 Instruments

All sizes of Eu/PS liposomes were measured using a dynamic light scattering instrument (DLS, ZETASIZER Nano ZS, Malvern Instrument Ltd., Worcestershire, UK). The TEM images of the liposomes were obtained using a Transmission Electron Microscope (TEM, TALOS L120C, FEI company, Oregon, USA) to confirm their morphologies and sizes. Fluorescence and absorbance signals were obtained using a microplate reader (SYNERGY H1, BioTek, Vermont, USA). For in vitro and in vivo Cerenkov and radioluminescence imaging, the in vivo imaging

system (IVIS 100, Perkin Elmer, Massachusetts, USA) was used. The PET images were acquired by a PET scanner (GENISYS4, Sofie Bioscience, California, USA) after intravenous injection of ^{64}Cu labeled Eu lipo, VBBO lipo and Eu/VBBO lipo in tumor bearing mice.

2.2.3 Eu^{3+} chelation with Diethylenetriaminepentaacetic acid (DTPA): Eu-DTPA complex

$\text{EuCl}_3 \cdot 6\text{H}_2\text{O}$ and DTPA were dissolved in distilled water and 0.5 M NaOH solution, respectively. After dissolution and mixing with equal molar ratios, a solution together with Eu^{3+} and DTPA was adjusted to neutral pH and filtered by the size exclusion chromatographical method.

2.2.4 Eu-DTPA and photosensitizer (PS) loaded liposome preparation

A facile self-assembly method with phosphatidylcholine (PC) series and cholesterol was used for making a liposome structure. Phosphatidylcholines, 1,2-Distearoyl-sn-glycero-3-phosphocholine (DSPC), 1,2-distearoyl-sn-glycero-3-phosphoethanolamine-N-[methyl(polyethylene glycol)-5000] (ammonium salt) (DSPE-PEG(5000)- CH_3), and cholesterol were dissolved in chloroform at a 6.6:1.3:1.6 molar ratio. Subsequently, the PS was added in a lipid pre-mixture. Chloroform in the lipid phase solution was evaporated with a rotary evaporator until a transparent lipid thin layer coated the bottom of the *vial*. Following evaporation, the lipid layer was vacuumed for 12 h to remove the remaining residual chloroform inside the layer. Europium-DTPA complex solution was added to the lipid layer *vial* and sonicated to form multilamellar vesicles (MLVs). The MLVs solution was subjected to additional ultrasonication for 10 min. Then, a transparent liposome

solution was filtered with a 0.2- μ m pore syringe filter and 30 K molecular weight cut-off (MWCO) tube for further studies.

2.2.5 Characterization of Eu/PS lipo with TEM and DLS

Europium/PS lipo was acquired by the TEM to confirm its morphology. For cryo-TEM imaging, the liposome was diluted with PBS solution before sample preparation onto a grid. The hydrodynamic size of the liposome was measured by the DLS instrument.

2.2.6 Radiolabeling of Eu and Ps embedded liposome (Eu/PS lipo) for in vivo imaging

For radiolabeling, 1,4,7-Triazacyclononane-1,4,7-triacetic acid (NOTA) was utilized as a chelator and 1,2-distearoyl-sn-glycero-3-phosphoethanolamine-N-[amino(polyethylene glycol)-2000] (ammonium salt) (DSPE-PEG(2000)-amine) was reacted with 2-(p-Isothiocyanatobenzyl)-1,4,7-triazacyclononane-N,N',N''-triacetic acid trihydrochloride ((p-SCN-Bn)-NOTA) overnight. The NOTA modified DSPE-PEG (2000) was added to the lipid pre-mixture before the transparent lipid layer was prepared. This step was the same as the Eu/PS lipo preparation procedure. For the radiolabeling, radioisotope solution was adjusted to pH 5 using 0.5~1 M HCl solution and was mixed with NOTA modified Eu/PS lipo at 37°C for 30 min. After the reaction, a radioisotope labeled Eu/PS lipo was eluted using a PD-10 column to purify it from unchelated free radioisotopes. To travel up-ward onto an ITLC-SG paper, 2 μ L of radiolabeled lipo-some was loaded. The radioisotope was read onto the paper by measuring its radioactivity signal.

2.2.7 In vitro stability test of Eu/PS lipo

Stability tests of liposomes loaded with Eu and PSs were conducted in PBS, human serum, and cell media (RPMI 1⁶⁴0) for 7 d. These lipo series were evaluated by measuring their sizes with DLS for up to 14 d to prove their stabilities in 3 different kinds of physiological conditions.

2.2.8 Eu³⁺ quantification analysis by K-shell X-ray fluorescence (XRF) detection system

The K-shell XRF detection system consisted of an external polychromatic X-ray source (X-RAD 320, Precision X-ray Inc., North Branford, CT, USA), a cadmium telluride (CdTe) detector for X-ray spectroscopy (X-123CdTe, Amptek Inc., Bedford, USA), and a cylindrical lead collimator. Six Eu-DTPA samples with different concentrations were used to obtain a linear relationship between the concentrations of Eu³⁺ and the amount of K-shell XRF photons emitted from Eu-DTPA. The concentrations of the samples were 0.058 wt/v %, 0.116 wt/v %, 0.233 wt/v %, 0.465 wt/v %, 0.93 wt/v %, and 1.86 wt/v %. Each sample was irradiated for 1 min by 140 kVp X-rays and the amount of photon counts of the most dominant XRF peaks (K α 1 peak of 41.5 keV and K α 2 peak of 40.9 keV) from the measured X-ray spectra by the CdTe detector were quantified. The measurement was repeated 5 times for each sample. The calibration curve showed a good linear fit between the concentration and the amount of XRF photons counts (*i.e.*, $R^2 = 0.9989$). The XRF photon counts emitted from Eu³⁺ in Eu lipo series were measured by the K-shell XRF detection system five times for each sample and the concentrations of Eu³⁺ were estimated using the calibration curve.

2.2.9 Radioluminescence test with ^{64}Cu radioisotope

Radioluminescence imaging was demonstrated with liposomes under different conditions (^{64}Cu -Eu lipo, ^{64}Cu -Eu/VBBO lipo, free ^{64}Cu , ^{64}Cu -VBBO lipo, Eu/VBBO lipo, and PBS) by measuring radioluminescence intensity with in vivo imaging system (IVIS). For the control group PBS was used in this study. The images were acquired at different wavelength spectra (open, green, and red emission spectrum filters). Quantitative analysis of radioluminescence (RL), Cerenkov luminescence (CL), RL energy transfer (RET), and Cerenkov luminescence energy transfer (CLET) efficiencies were calculated based on the ROI values with IVIS imaging as follows:

$\text{CLET} = 1 - \text{CL}_2 / \text{CL}_1$, where CL_1 is luminescence intensity of free ^{64}Cu , and CL_2 is luminescence intensity of ^{64}Cu -VBBO lipo.

$\text{RET} = 1 - \text{RL}_2 / \text{RL}_1$, where RL_1 is luminescence intensity of (^{64}Cu -Eu lipo – free ^{64}Cu), and RL_2 is luminescence intensity of [^{64}Cu -Eu/VBBO lipo + (free ^{64}Cu - ^{64}Cu -VBBO lipo)], note that RET was adjusted for influence of CLET.

2.2.10 ROS generation with the radioisotope-induced radioluminescence

The degree of ROS generation by radiolabeled liposomes with radioisotope triggered radioluminescence by Eu was determined. In 96-well black microplates 100 μL of free ^{64}Cu , ^{64}Cu -VBBO lipo, and ^{64}Cu -Eu/VBBO lipo were arranged with different ^{64}Cu activities (0, 30, 100, and 200 μCi). Tris-HCl buffer solution (pH 8.0 and 10 mM) was added to activate ROS measurable reagent and 2 μL of SOSG solution (1 μM) was added to each well. The fluorescence intensity of the SOSG reagent at its excitation wavelength ($\lambda_{\text{ex}} = 494 \text{ nm}$) was measured in each well. The

free ^{64}Cu was used as a control group. An increase degree of ROS generation was calculated to fluorescence intensity ratio between liposomes with and without ^{64}Cu .

2.2.11 In vitro ROS production

To confirm the ROS productive cells, Eu/VBBO lipo and ^{64}Cu -Eu/VBBO lipo (^{64}Cu activity: 100 μCi) were treated to the cells and incubated for 24 h. After the incubation, cells were stained with 5 μM of the fluorescent probe (CellROX[®] Oxidative Stress Reagents, Invitrogen[™]) for 20 min at 37°C and the nucleus of the cell was co-stained with 10 μM of Hoechst 33342 (Invitrogen[™]). The stained cells were washed with DPBS 3 times and fixed with 4% PFA for 30 min, which had also been washed with DPBS 3 times. After the washing steps, the fluorescence levels of the fixed cells were observed by fluorescence optical microscopy (Cell Observer, Carl Zeiss, Oberkochen, Germany).

2.2.12 Preparation of tumor model

All animal experiments were performed in accordance with the Institutional Animal Care and Use Committee, Seoul National University Hospital. FaDu tumor bearing Balb/c nude mice were utilized for in vivo stable and passive tumor targeted PET imaging. The FaDu cell line (105 cells/20 μL PBS) was injected subcutaneously into the right thigh. The tumor grown mice PET imaging was performed when the implanted tumor reached a required size (mean diameter: 5~10 mm).

2.2.13 In vivo tumor targeted PET imaging of ^{64}Cu labeled liposomes

^{64}Cu labeled VBBO lipo and Eu/VBBO lipo were per-formed in vivo imaging with FaDu tumor models. Approximately 200 μL of ^{64}Cu labeled VBBO lipo or

Eu/VBBO lipo (~70 μCi respectively) were injected intravenously into the FaDu tumor bearing mice. The PET scan images were acquired at different time points (0, 2, 12, 24, and 48 h) using PET scanner (GENESYS4). The ROI values were calculated and analyzed for the major organs (heart, liver, spleen, and muscle), including tumor regions with PET images using MIM software for Quantitative analysis. A time activity curve was fitted based on %ID/g at each time point and Tumor targeting efficiency was calculated by comparing the tumor to other organs (heart, muscle, and liver).

2.2.14 In vitro photodynamic therapy with ^{64}Cu labeled liposomes

The head and neck cancer FaDu cell line was cultured with Dulbecco's modified Eagle's medium (DMEM), 10% fetal bovine serum (FBS), and 1% penicillin/streptomycin and incubated at 37°C at 5% CO_2 . Once the cell line was covered with about 90% of cell culture in the flask, cells were seeded into 96-well culture plates for cell viability tests (10^4 cells per well) and incubated at 37°C and 5% CO_2 overnight. After removal of media, ^{64}Cu labeled Eu lipo, VBBO lipo, and Eu/VBBO lipo were added to each well with a different activity (0, 10, 30, and 100 μCi). The control group was cells without any treatment of liposomes. Control and experimental groups were incubated for 24 h. The MTT assay was conducted after all the media and liposomes were re-moved. Cell viability was determined by measuring the absorbance of each well ($\lambda_{\text{abs}} = 540 \text{ nm}$).

2.2.15 In vivo photodynamic therapy with ^{64}Cu labeled liposomes

^{64}Cu -Eu/VBBO lipo, ^{64}Cu -VBBO lipo, Eu/VBBO lipo, and normal saline were injected intravenously to the FaDu tumor model mice, respectively (Eu^{3+}

concentration: 5.3 μmol and VBBO concentration: 6.25 μM). For the radioisotope-induced PDT, each liposome was radiolabeled with ^{64}Cu of 500 μCi activity. Tumor growth follow-ups were conducted for 14 d by acquiring tumor images and measuring the tumor sizes at different time points (0, 2, 8, and 14 days). After the PDT, a tumor in each group was paraffin sectioned and H&E staining was conducted for tumor tissue imaging.

2.3 Results and discussion

2.3.1 Study scheme

Our radioluminescence liposome nanoplatfrom for PDT was designed to load Eu-DTPA in the hydrophilic core, PS in the hydrophobic lipid bilayer, and radioisotopes on the surface of the liposome. Rose Bengal (RB), Victoria blue-BO (VBBO), and chlorin e6 (Ce6) were tested for PSs. Europium-DTPA loaded liposome (Eu lipo), Eu-DTPA, and PS co-loaded liposome (Eu/RB lipo, Eu/VBBO lipo, Eu/Ce6 lipo) were prepared by self-assembly with phosphatidylcholine (PC) derivatives and cholesterol. Europium lipo, VBBO lipo, and Eu/VBBO lipo were radiolabeled using ^{64}Cu (^{64}Cu -Eu lipo, ^{64}Cu -VBBO lipo, ^{64}Cu -Eu/VBBO lipo), and they were tested for their radioluminescence effect and ROS generation ability. Subsequently, ^{64}Cu -Eu/VBBO lipo was tested for in vitro and in vivo PDT and in vivo positron emission tomography (PET) imaging was conducted with ^{64}Cu -Eu/VBBO lipo to determine its biodistribution and passive targeting efficiency in the mouse xenograft tumor model. The radioluminescence and ROS generation mechanism of our nanoplatfrom for PDT can be explained as a 3-step event: First, Eu-DTPA emits radioluminescence in red visible spectrum ($\lambda_{\text{em}}= 615 \text{ nm}$) by the labeled radioisotopes. Then the radioluminescence energy from the Eu-DTPA is transferred to the PS. Finally, PS emits ROS by radioluminescence energy transfer (RET) to kill tumor cells (**Figure 2.2**).

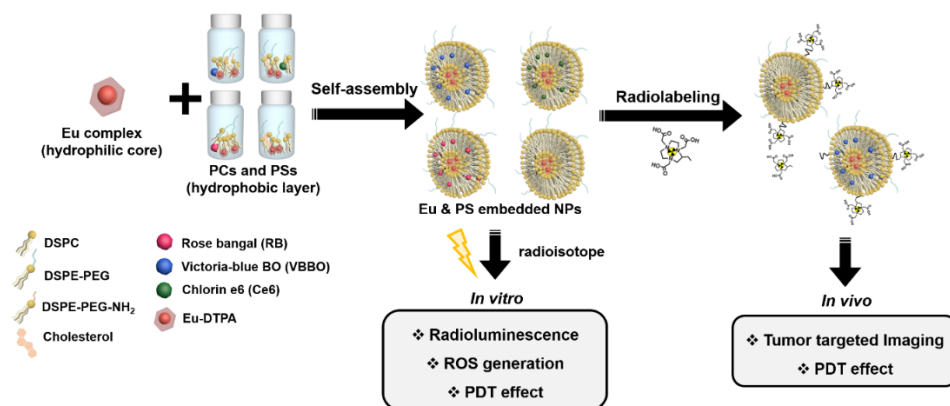


Figure 2.2 Schematic diagram of Eu/PS loaded radioluminescence liposome nanoplatform synthesis and experimental design.

2.3.2 Size and radiochemical stability of radiolabeled Eu/PS lipo

The spherical shape and uniform size distribution of Eu/VBBO lipo were revealed by transmission electron microscopy (TEM) (**Figure 2.4 a**). Hydrodynamic sizes of Eu lipo, Eu/RB lipo, Eu/Ce6 lipo, and Eu/VBBO lipo were 76.65 ± 22.88 , 76.35 ± 26.58 , 77.09 ± 27.64 , and 78.14 ± 27.93 nm, respectively (**Figure 2.4 b**). The stabilities of the liposome nanoplatform in various physiological solutions (phosphate buffered saline (PBS), human serum, and cell media) were assessed to determine the feasibility of in vivo utilization of the liposome nanoplatform.

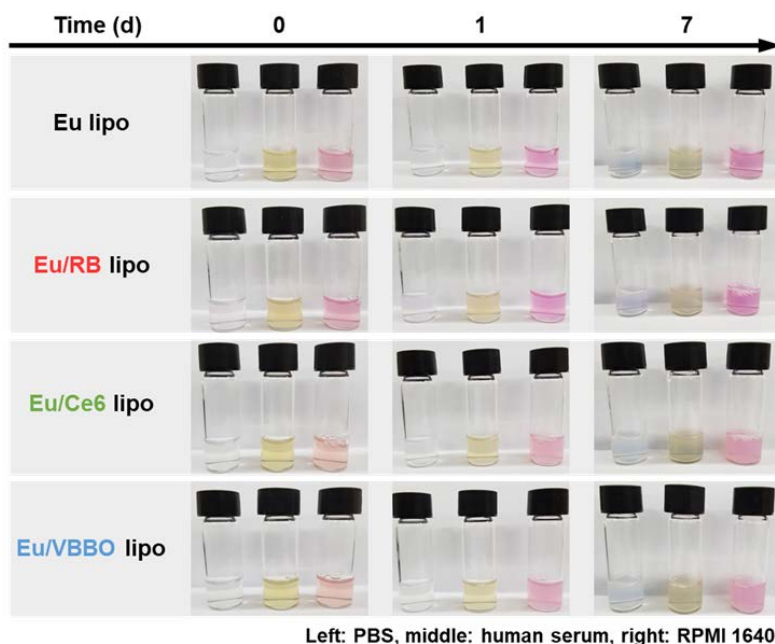


Figure 2.3 Stability test of nanoparticles under various physiological conditions (PBS, human serum, and cell media (RPMI 1640)). No visible aggregates of the liposomes were observed in all 3 solutions.

There were no visible aggregates or precipitates when used in the physiological solutions for 7 d (**Figure 2.3**). Additionally, the hydrodynamic sizes of the liposome nanoplatform were stable for 14 d, which showed high in vitro stability of the nanoplatform (**Figure 2.4 c**). In further experiments, VBBO was chosen for the PS because it had the best matched absorbance wavelength ($\lambda_{\text{abs}} = 615 \text{ nm}$) among the tested PSs with an emission wavelength of Eu ($\lambda_{\text{em}} = 615 \text{ nm}$) (**Figure 2.5**).

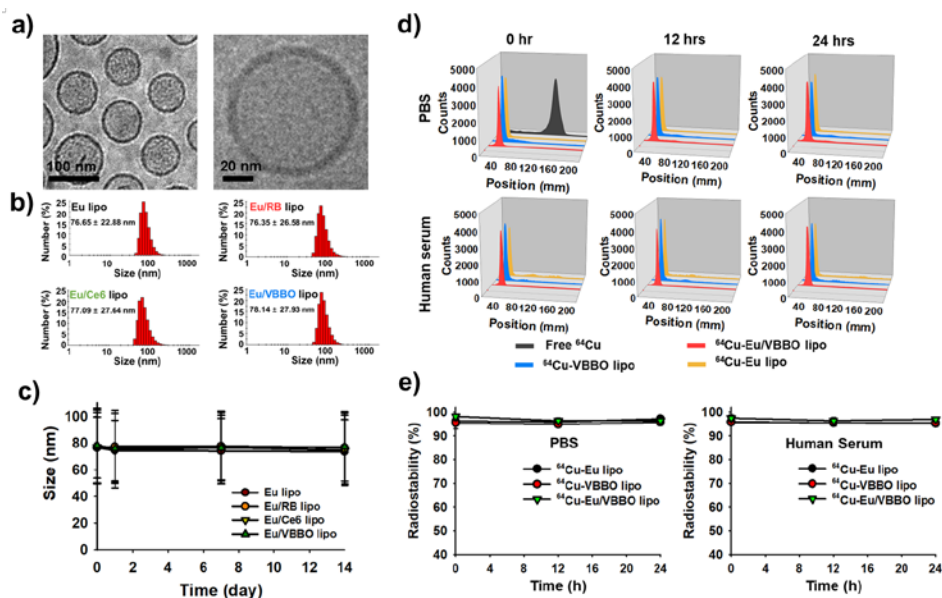


Figure 2.4 Characterization of Eu lipo and Eu/PS lipo. a) TEM images of Eu/VBBO lipo with low (left) and high magnifications (right), respectively. b) Hydrodynamic sizes of Eu lipo and Eu/PS lipo ($n = 6$, mean \pm s.d.). c) Stability test of Eu lipo and Eu/PS lipo in PBS for 14 d ($n = 6$, mean \pm s.d.). d) and e) Radiolabeling stability test in PBS and human serum solutions ($n = 6$, mean \pm s.d.). Eu: Eu-DTPA, PS: photosensitizer, RB: rose bengal, Ce6: chlorin e6, VBBO: victoria blue-BO.

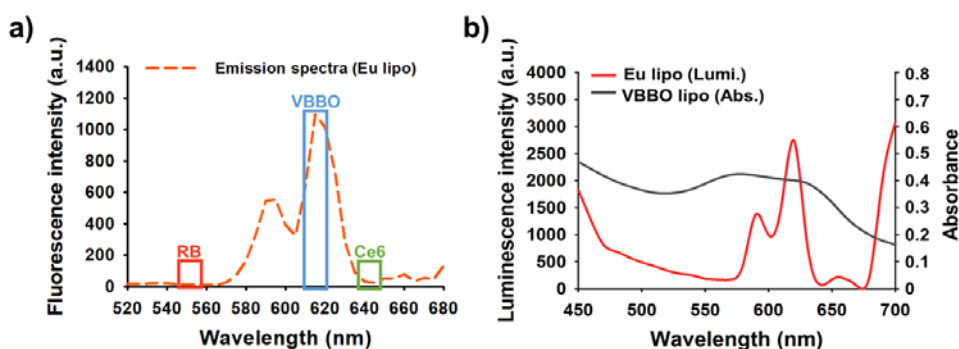


Figure 2.5 Luminescence spectra between Eu³⁺ and PSs. a) Spectra overlap profiles of RB, VBBO, and Ce6 with emission of Eu³⁺ (Absorb-ance peaks of PSs: RB: rose bengal, VBBO: victoria blue-BO, Ce6: chlorin e6).

RB ($\lambda_{\text{max}} = 550 \text{ nm}$), VBBO ($\lambda_{\text{max}} = 615 \text{ nm}$), and Ce6 ($\lambda_{\text{max}} = 640 \text{ nm}$)). b) Spectra of Eu^{3+} emission and VBBO absorbance.

The radiolabeling efficiencies of ^{64}Cu -Eu lipo, ^{64}Cu -VBBO lipo, and ^{64}Cu -Eu/VBBO lipo were $96.2 \pm 1.68\%$, $95.3 \pm 2.33\%$, and $98.1 \pm 0.68\%$ in PBS, respectively (**Figure 2.6**). The radiochemical stabilities were over 95% for up to 24 h in PBS and human serum (**Figure 2.4 d-e**). Thus, the radiolabeled Eu/PS loaded radioluminescence liposome nanoplatform was very stable in physiological solution in terms of size and radiochemistry profile, which suggesting that in vivo utilization of the nanoplatform would be effective.

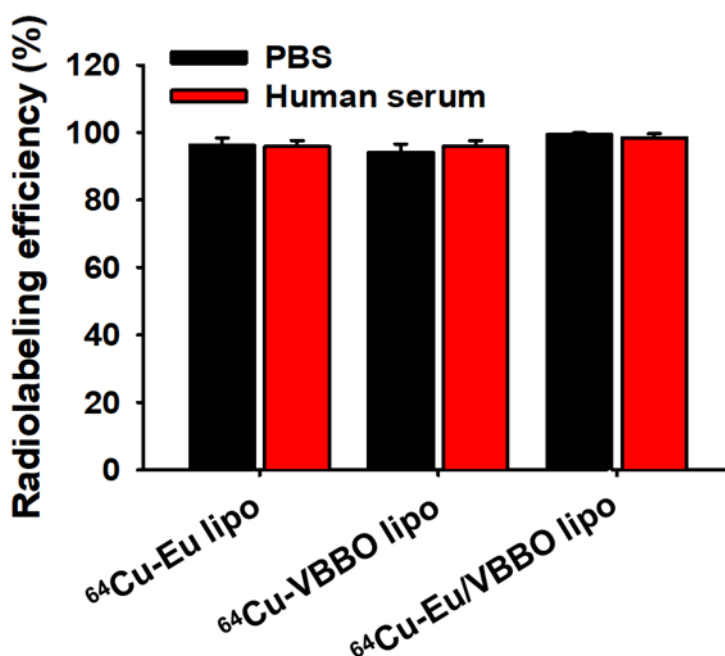


Figure 2.6 Radiolabeling efficiency of radiolabeled liposomes. Radiolabeling efficiency test with ^{64}Cu -Eu lipo, ^{64}Cu -VBBO lipo, and ^{64}Cu -Eu/VBBO lipo in PBS and human serum, respectively.

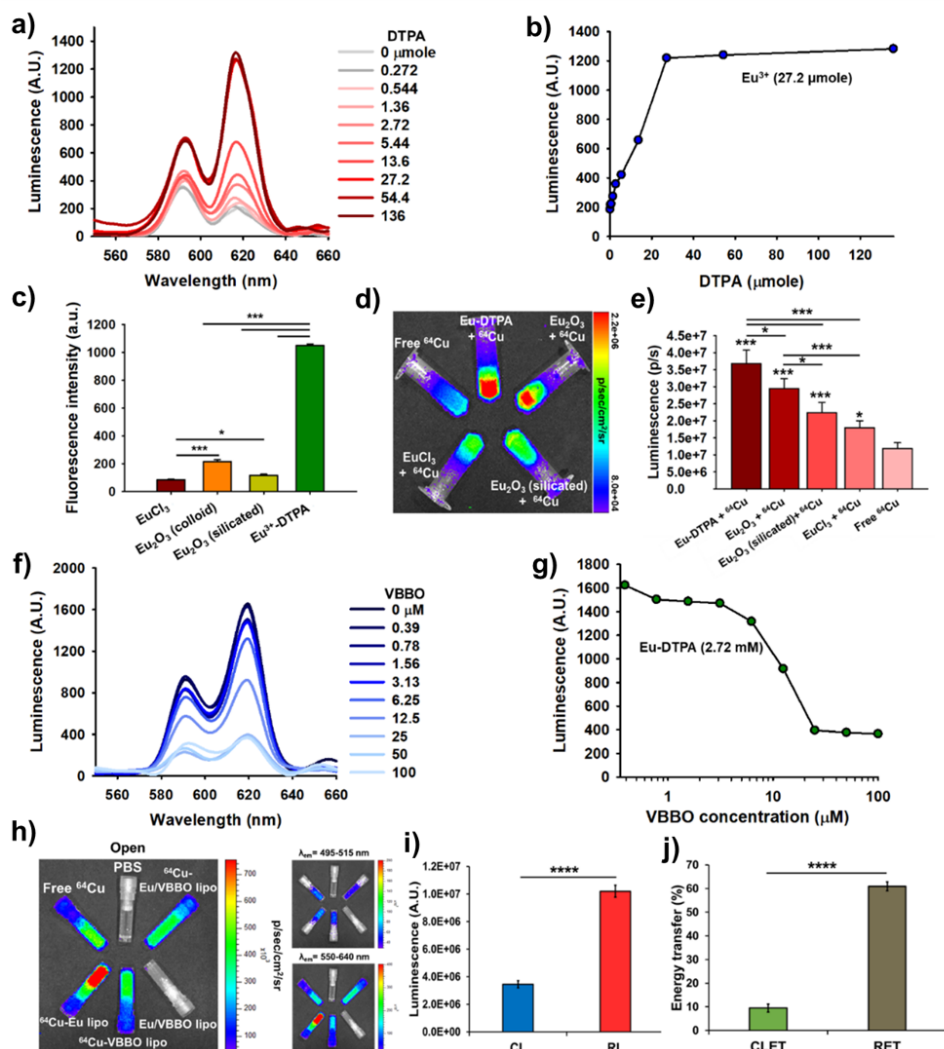


Figure 2.7 Radioluminescence and radioluminescence energy transfer. a) and b) Luminescence emission spectra of Eu^{3+} with the addition of diethylenetriamine pentaacetic acid (DTPA). c) Luminescent intensities in different forms of Eu^{3+} included NPs ($n = 5$, mean \pm s.d.). d) and e) Radioluminescence imaging and quantitative comparison with various Eu NPs in the presence of ^{64}Cu (500 μCi) ($n = 5$, mean \pm s.d.). Notably, the amount of Eu was the same (13.6 μmol) in the various Eu containing NPs. f) and g) Emission spectra of Eu-DTPA by adding VBBO with constant Eu-DTPA (2.72 μmol) concentration. h) Radioluminescence imaging in

different kinds of liposomes with and without ^{64}Cu labeling under open, green, and red emission filters by IVIS. The activity of ^{64}Cu in free ^{64}Cu , ^{64}Cu -Eu lipo, ^{64}Cu -VBBO lipo, ^{64}Cu -Eu/VBBO lipo was the same (500 μCi). The concentration of VBBO in ^{64}Cu -VBBO lipo, ^{64}Cu -Eu/VBBO lipo, and Eu/VBBO lipo was the same (12.5 μM). The amount of Eu in ^{64}Cu -Eu lipo, ^{64}Cu -Eu/VBBO lipo, and Eu/VBBO lipo was the same (5.44 μmol) i) Quantitative comparisons between Cerenkov luminescence (CL) and radioluminescence (RL) ($n = 6$, mean \pm s.d.). j) Quantitative comparisons between Cerenkov luminescence energy transfer (CLET) and radioluminescence energy transfer (RET) ($n = 6$, mean \pm s.d.). *: $P < 0.05$, **: $P < 0.01$, ***: $P < 0.001$, ****: $P < 0.0001$. The one-way ANOVA followed by Tukey post hoc test for (c, e) and Student's t test for (i, j) were conducted for statistical analysis.

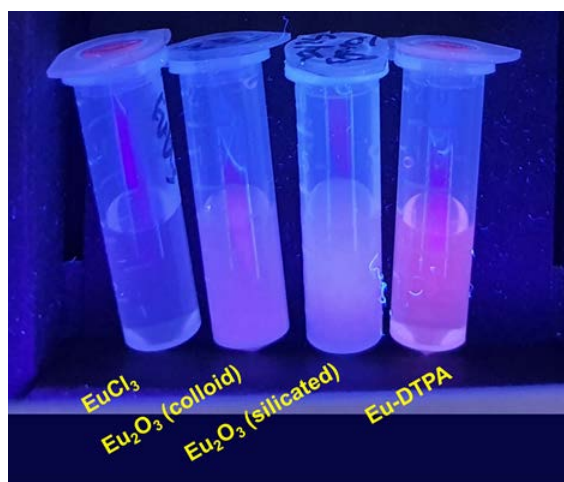


Figure 2.8 Fluorescence images of 4 different forms of Eu included NPs.

2.3.3 Radioluminescence and radioluminescence energy transfer of radiolabeled Eu/VBBO lipo

We utilized Eu-DTPA for radioluminescence emission and confirmed that luminescence from Eu^{3+} was enhanced by chelation with DTPA in a dose dependent manner and saturated when the amount of Eu^{3+} and DTPA were the same (**Figure 2.7 a-b**). Moreover, Eu-DTPA showed a significantly higher luminescence intensity under ultraviolet (UV) excitation than Eu_2O_3 NPs in colloid or silicated form, (5.1, 8.9 folds, respectively) (**Figure 2.7 c, Figure 2.8**).

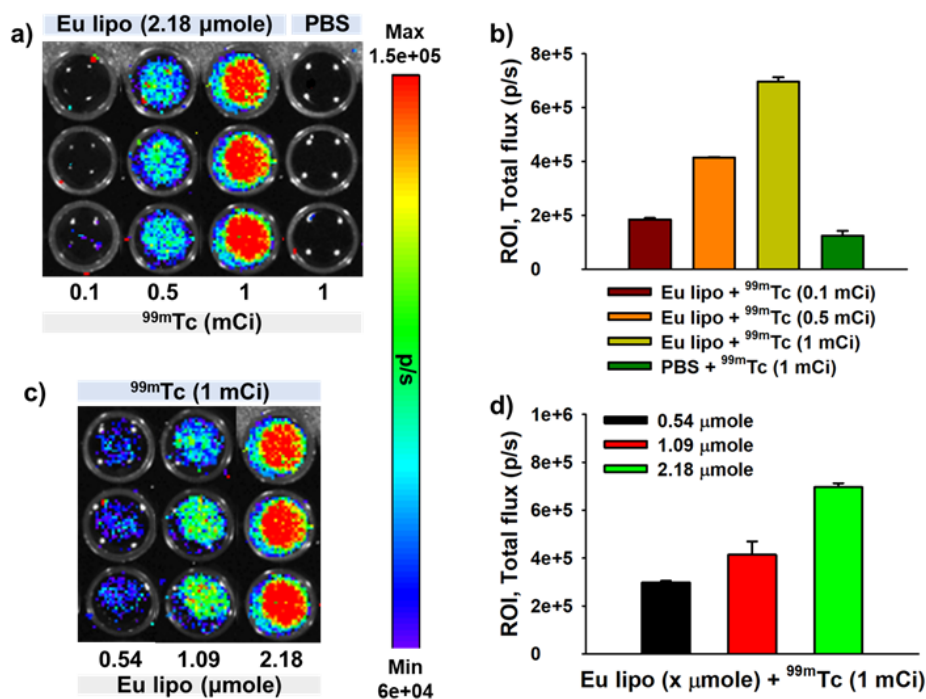


Figure 2.9 Radioluminescence test with different Eu^{3+} concentrations and activities of $^{99\text{m}}\text{Tc}$. The radioluminescence emission test was conducted with Eu lipo in the presence of $^{99\text{m}}\text{Tc}$. Constant concentrations of Eu lipo were treated into 96-well black plates to measure its radioluminescence. $^{99\text{m}}\text{Tc}$ with different activities (0.1, 0.5, and 1 mCi) were added into each well with Eu lipo (a) and b)). In contrast,

different concentrations of Eu lipo (0.54, 1.09, 2.18 μmol) were respectively added into a constant activity of $^{99\text{m}}\text{Tc}$ (1 mCi) (c) and d)). As the concentration of Eu lipo and $^{99\text{m}}\text{Tc}$ activity increased, radioluminescence intensity increased proportionally. The radioluminescence intensities of Eu lipo nanoparticles (NPs) with $^{99\text{m}}\text{Tc}$ groups were lower than those of NPs with ^{64}Cu because the $^{99\text{m}}\text{Tc}$ does not emit β or Cenrenkov luminescence like ^{64}Cu , but emits γ rays only.

When radioluminescence from the Eu-DTPA, Eu_2O_3 NPs, and Eu_2O_3 NPs (silicated) under ^{64}Cu were compared, the radioluminescence intensity of Eu-DTPA was significantly higher than Eu_2O_3 NPs, and Eu_2O_3 NPs (silicated) (**Figure 2.7 d-e**). Furthermore, the radioluminescence intensity of the Eu-DTPA was 7.16-fold higher than Eu_2O_3 NPs in colloid form and 8.9-fold higher than Eu_2O_3 NPs (silicated) in the presence of $^{99\text{m}}\text{Tc}$ (**Figure 2.10 a-b**).

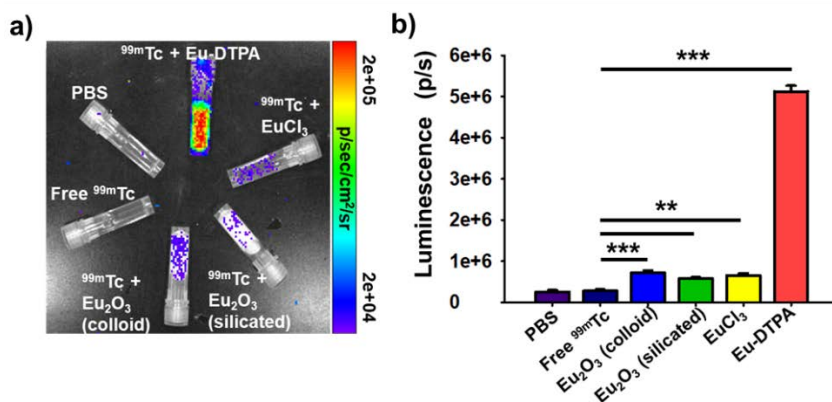


Figure 2.10 Radioluminescence observation of Eu-DTPA. a) Radioluminescence imaging and b) quantitative comparison with various Eu NPs in the presence of $^{99\text{m}}\text{Tc}$ (1 mCi) ($n = 3$, mean \pm s.d.). Notably, the amount of Eu was the same (13.6 μmol) in the various Eu containing NPs. Statistical analysis was conducted by ANOVA test.

Europium ion is a rare earth metal and has been used as a luminescent probe for various purposes because of its unique luminescence properties, including sharp emission bands, long luminescence life time, and large Stoke shift.³⁸⁻⁴⁰ The luminescence of Eu^{3+} is emitted from the electronic 4f-4f transitions from the $^5\text{D}_0$ level to $^7\text{F}_{J=0,1,2,3,4}$ ground state and the transition of $^5\text{D}_0 \rightarrow ^7\text{F}_2$ is responsible for the most intensive luminescence at 615 nm. In solution, Eu^{3+} emits a very low intensity luminescence because of the quenching effect of water molecules. To enhance the luminescence intensity, Eu^{3+} can be combined with chelators, such as DTPA derivatives or organic chromophores, including so called antenna like pyridine and bipyridine derivatives.⁴¹⁻⁴⁶ The luminescence intensity of Eu^{3+} can be enhanced by doping into hard-core NPs, such as sodium zinc molybdate NPs²⁸, zinc oxide NPs⁴⁷, yttrium oxide NPs⁴⁸, and cerium oxide NPs.⁴⁹ The Eu^{3+} doped hard-core NPs or Eu_2O_3 NPs are reported to produce strong luminescence emissions by ionizing radiation, including X-ray, gamma and beta rays.^{18, 50-53} Also, we found that Eu-DTPA showed the significantly higher radioluminescence than Eu_2O_3 NPs and Eu_2O_3 (silicated) NPs. We assume that the difference is caused by the concentration quenching effect in Eu_2O_3 NPs. Although the amount of Eu^{3+} was the same between the solutions containing Eu-DTPA and Eu_2O_3 NPs (13.6 μmol), Eu-DTPA is well dispersed in the solution while Eu_2O_3 NP has a high ion concentration in each NP (Calculated number of Eu^{3+} ions = 6.096×10^7 / NP, calculated from <https://materialsproject.org/materials/mp-647924/>). The concentration quenching effect of lanthanides based NPs has been reported in the literature.^{54, 55} For example, Eu^{3+} doped alumina displayed a much longer luminescence lifetime than Eu_2O_3 NPs.⁵⁶

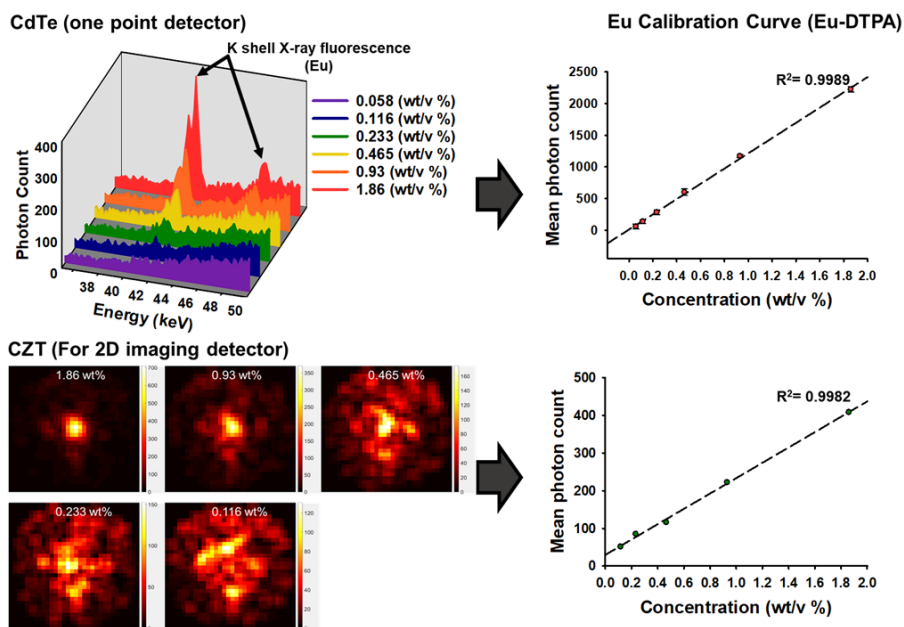


Figure 2.11 Quantitative analysis of Eu lipo by characteristic X-ray fluorescence detection with one point detector and CZT 2D imaging detector.

It has been reported that the luminescence of Eu can be enhanced by chelation using chelators with or without chromophores.^{57, 58} Chelator without chromophore can enhance the luminescence of Eu^{3+} because Eu^{3+} could be protected by the chelators from water molecules which can quench luminescence of Eu^{3+} dramatically by solvating Eu^{3+} in aqueous environment. Also, a chromophore in chelator can function as an 'antenna,' absorbing incident light then transferring this excitation to the Eu^{3+} ion to further enhance the luminescence of Eu^{3+} .⁵⁹ We used chelator without chromophore, DTPA, because DTPA is widely used chelator in the clinic based on its excellent safety profile. For example, Gd-DTPA is used for MRI contrast agent, and $^{99\text{m}}\text{Tc}$ -DTPA is used for renal function test in the clinic.

We found that Eu-DTPA had excellent radioluminescence abilities, and this is, to the best of our knowledge, the first study to utilize radioluminescence from Eu-chelates for in vivo PDT.

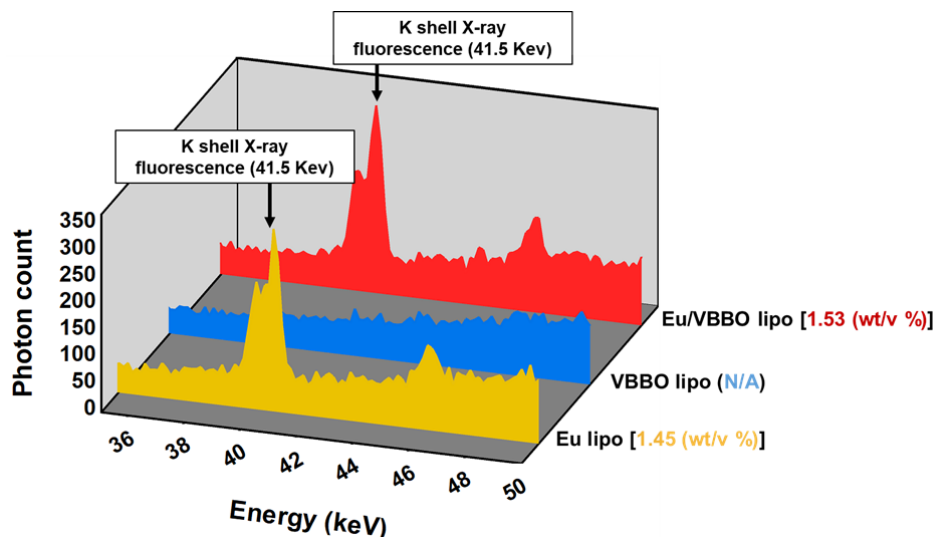


Figure 2.12 Quantitative analysis of Eu lipo, VBBO lipo, and Eu/VBBO lipo by characteristic X ray fluorescence detection.

Luminescence resonance energy transfer (LRET) between lanthanides, such as Eu^{3+} ion as a donor to the organic dyes or quantum dots as acceptors have been reported.^{60,}

⁶¹ We found that the luminescence intensity from Eu-DTPA could be efficiently reduced by adding VBBO, indicating the occurrence of LRET from Eu-DTPA to VBBO (**Figure 2.7 f-g**). Assuming that the presence of VBBO did not introduce another nonradiative de-excitation pathway for Eu-DTPA in addition to LRET, the LRET efficiency was quantified as $1 - L/L_0$, where L is the luminescence intensity of Eu-DTPA in the presence of VBBO and L_0 is the luminescence intensity of Eu-

DTPA without VBBO.⁶² From the results shown in **Figure 2.7 g**, the LRET efficiency between Eu-DTPA and VBBO could reach up to 0.78.

After synthesis of Eu lipo, loading efficiency of Eu-DTPA was confirmed to be about 31% by measuring luminescence from purified and unpurified Eu lipo (**Figure 2.8**). The radioluminescence ability of Eu lipo was confirmed by adding ^{99m}Tc, which has no luminescence itself. In vivo Imaging System (IVIS) imaging revealed that the radioluminescence was associated with ^{99m}Tc activity and Eu lipo concentration (**Figure 2.9**). Furthermore, Eu lipo emitted fluorescence X-rays *via* de-excitation processes caused by the interaction between external X-rays and Eu. Thus, Eu lipo can be imaged by an in-house X-ray fluorescence (XRF) imaging device (**Figure 2.11**).⁶³ These results suggest that radiolabeled Eu lipo could be used as a multimodal imaging agent, including PET, X-ray fluorescence imaging, multispectral SPECT imaging and radioluminescence imaging.⁵² We were also able to measure the amount of Eu³⁺ in Eu/VBBO lipo by the K-shell X-ray fluorescence (XRF) detection system (**Figure 2.12**).

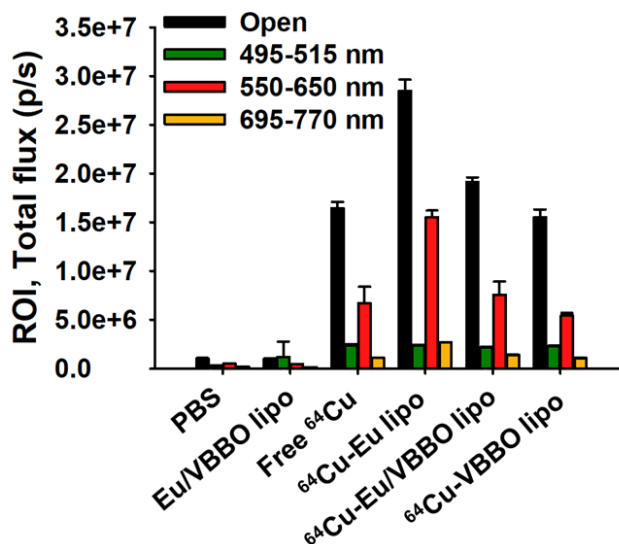


Figure 2.13 Quantitative comparison of RL and CL with ⁶⁴Cu radiolabeled liposomes under the different emission region filters. Luminescences predominantly emitted in the red spectrum region (550-650 nm).

To the radioluminescence liposome nanoplatform, ⁶⁴Cu was labeled for further in vivo imaging and therapy experiments. After radiolabeling of ⁶⁴Cu to the radioluminescence liposome nanoplatform, luminescence imaging of the free ⁶⁴Cu, ⁶⁴Cu-Eu lipo, ⁶⁴Cu-VBBO lipo, Eu/VBBO lipo, ⁶⁴Cu-Eu/VBBO lipo and PBS were performed using IVIS. We found that luminescence emitted by ⁶⁴Cu-Eu lipo was significantly higher than free ⁶⁴Cu (**Figure 2.7 h**). We compared the intensity of radioluminescence from the Eu-DTPA in ⁶⁴Cu-Eu lipo, quantified by the luminescence of ⁶⁴Cu-Eu lipo minus that of free ⁶⁴Cu, with the intensity of the Cerenkov luminescence from free ⁶⁴Cu and found that the radioluminescence was higher than the Cerenkov luminescence by more than a factor of 2 ($3.44 \times 10^6 \pm 2.6 \times 10^5$ p/s vs. $1.02 \times 10^7 \pm 4.30 \times 10^5$ p/s, $P < 0.0001$) (**Figure 2.7 i**). We also found

that the luminescence intensity of ^{64}Cu -VBBO was lower than that of free ^{64}Cu , and the intensity of ^{64}Cu -Eu/VBBO lipo was lower than that of ^{64}Cu -Eu lipo (**Figure 2.7 g**). These results indicate that VBBO co-loading can induce energy transfer to VBBO from Cerenkov luminescence or radioluminescence. Cerenkov luminescence from free ^{64}Cu showed a higher intensity at the red visible light region (550~640 nm wavelength) than the blue light region (400~450 nm) (**Figure 2.7 g, Figure 2.13**), because of the rapid light shift of Cerenkov luminescence.²⁷ The quantified Cerenkov luminescence energy transfer (CLET) and RET were compared and we found that RET of ^{64}Cu -Eu/VBBO lipo was about six-fold higher than CLET of ^{64}Cu -VBBO lipo ($9.5 \pm 1.69\%$ vs. $61.0 \pm 1.87\%$, $P < 0.0001$) (**Figure 2.7 j**).

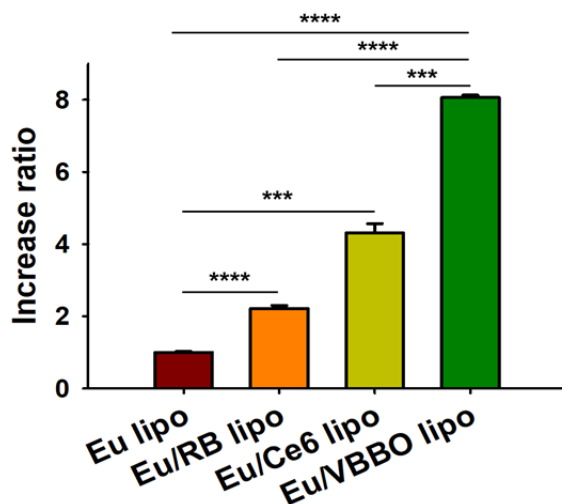


Figure 2.14 ROS generation test with $^{99\text{m}}\text{Tc}$. Levels of ROS production demonstration with Eu lipo and Eu/PS lipo series in the presence of $^{99\text{m}}\text{Tc}$. Europium lipo and Eu/PS lipo series loaded with 3 different kinds of PSs which were RB, VBBO, and Ce6 were mixed with $^{99\text{m}}\text{Tc}$ to excite Eu^{3+} for radioluminescence. Among these 3 types of PSs, a max absorption wavelength ($\lambda_{\text{max}} = 615\text{ nm}$) of VBBO overlapped more than those of the other 2 kinds of PSs with the radioluminescence

wavelength of Eu^{3+} according to the Eu^{3+} emission spectrum. The increase in ROS generation was the highest, about 8-fold higher, in VBBO loaded Eu lipo compared to the control, which was Eu lipo without PS. Therefore, Eu/VBBO lipo was selected as a main experimental liposomal nanoparticle platform for in vitro and in vivo imaging and PDT. Statistical analysis was conducted by ANOVA test.

The Förster radii between Eu-DTPA (donor) and various dyes (acceptor) have been reported to range from 5 to 10 nm.⁶¹ Since the diameter of our liposome nanoplatfrom is 78 nm, it is likely that an appreciable amount of VBBO (acceptor) was present within the Förster radius of Eu-DTPA in ^{64}Cu -Eu/VBBO lipo. As a result, the calculated RET efficiency in our liposome nanoplatfrom (64.2%) is high, approaching the calculated maximum LRET efficiency between Eu-DTPA and VBBO (78%) in solution (**Figure 2.7 g**), and is much larger than the efficiency of the ^{64}Cu -to-VBBO CLET (9.5%). It is unclear whether the CLET occurs by radiative energy transfer, *i.e.*, *via* absorption of photons emitted by Cerenkov luminescent, or resonantly, analogous to LRET. In either case, the lower efficiency of the CLET compared to the RET can be rationalized; in general, radiative energy transfer is much less efficient than resonant energy transfer⁶⁴; the Eu-DTPA emission spectrum, compared to broad Cerenkov luminescence, has a sharper peak and a better spectral matching with the VBBO absorption spectrum. Based on these results, we hypothesized that radioluminescence-induced PDT by ^{64}Cu -Eu/VBBO lipo will be more effective than Cerenkov luminescence-induced PDT by ^{64}Cu -VBBO lipo.

2.3.4 Effective ROS generation and in vitro PDT effect of ^{64}Cu -Eu/VBBO lipo

Reactive oxygen species generation and in vitro PDT tests were conducted using ^{64}Cu -Eu/VBBO lipo and ^{64}Cu -VBBO lipo; all studies were triplicated. Free ^{64}Cu or ^{64}Cu -Eu lipo were utilized as the control group. Singlet oxygen was detected by measuring a fluorescence of Singlet Oxygen Sensor Green (SOSG) reagent. In ^{64}Cu -VBBO lipo, the ROS levels with 100 and 200 μCi of ^{64}Cu , were 3.10 and 10.11 times higher than those with 0 μCi of ^{64}Cu , respectively ($P < 0.01$ and $P < 0.001$, respectively). In 30 μCi of ^{64}Cu , ^{64}Cu -VBBO lipo could not generate ROS, but ^{64}Cu -Eu/VBBO lipo could. The ROS fold increases of ^{64}Cu -Eu/VBBO lipo were significantly higher than those of ^{64}Cu -VBBO lipo at all ^{64}Cu activity points ($P < 0.001$). Free ^{64}Cu did not produce ROS up to 200 μCi (**Figure 2.15 a**). ROS generation in the FaDu cells after incubation with ^{64}Cu -Eu/VBBO lipo was also confirmed using the CellROX[®] reagent *via* the fluorescence microscopic image (**Figure 2.15 b**). In vitro PDT effects of ^{64}Cu -Eu lipo, ^{64}Cu -VBBO lipo, and ^{64}Cu -Eu/VBBO lipo were compared in the FaDu cell line (a human head and neck cancer cell line), by 3-(4,5-dimethylthiazol-2-yl)-2,5-diphenyltetrazolium bromide (MTT) assay. ^{64}Cu -VBBO lipo and ^{64}Cu -Eu/VBBO lipo showed tumor cell killing effects with ^{64}Cu activity of 30 and 100 μCi . ^{64}Cu -Eu lipo showed no significant cell killing effects. The cell killing effect was significantly higher in ^{64}Cu -Eu/VBBO lipo than ^{64}Cu -VBBO lipo (30 μCi ($P < 0.05$), 100 μCi ($P < 0.05$)) (**Figure 2.15 c**). Cell microscopic images after MTT assay were corroborated with the quantified results of MTT assays (**Figure 2.15 d**). Thus, ^{64}Cu -Eu/VBBO lipo had a higher ROS generation ability and in vitro PDT effect than ^{64}Cu -VBBO lipo, suggesting that radioluminescence-induced PDT was more efficient than Cerenkov luminescence-induced PDT.

It is noteworthy that ^{64}Cu has 38% of beta ray emissions, which is a type of cancer therapeutic ionizing radiation.⁶⁵ We found that there was neither ROS generation nor PDT effect under 200 μCi of free ^{64}Cu , but we were able to observe significant ROS generation and PDT effect with only one seventh (30 μCi) of ^{64}Cu with the addition of our radioluminescence liposome nanoplatform in in vitro PDT experiments. This indicates that our radioluminescence nanoplatform could be applied to enhance the treatment effect or lower the radiation dose of currently used targeted radioisotope therapy using beta ray emitters. Furthermore, $^{99\text{m}}\text{Tc}$, a pure gamma ray emitter, which is used for in vivo imaging⁶⁶⁻⁶⁸, was able to induce ROS generation from Eu/PS lipo (Figure 2.14), which further suggests the possibility of converting diagnostic radioisotopes into therapeutics by the addition of a radioluminescence liposome nanoplatform.

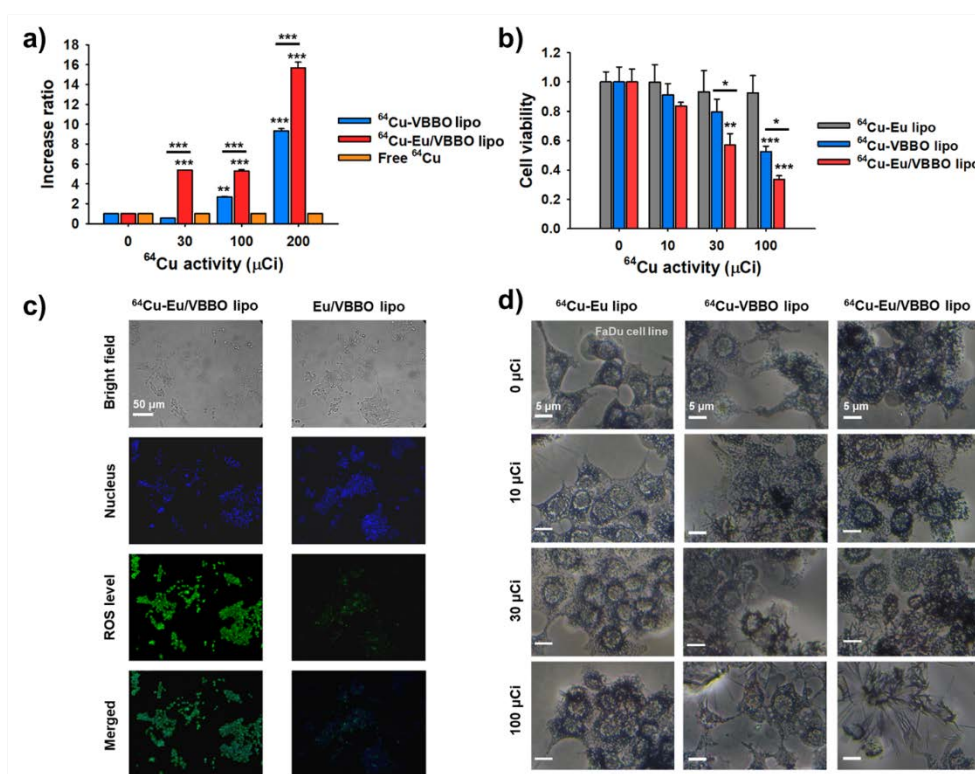


Figure 2.15 ROS generation test and in vitro radioisotope-induced photodynamic therapy. a) ROS generation by ^{64}Cu -Eu/VBBO lipo, ^{64}Cu -VBBO lipo, and free ^{64}Cu ($n = 6$, mean \pm s.d.) at different activities of ^{64}Cu . b) Fluorescence microscopic image of FaDu cells after incubation with ^{64}Cu -Eu/VBBO lipo or Eu/VBBO lipo (^{64}Cu activity: 100 μCi , Green: CellROX[®] for ROS detection, Blue: Hoechst 33342 for cell nuclei staining, scale bar: 50 μm). c) Tumor cell killing effect of ^{64}Cu -Eu lipo, ^{64}Cu -VBBO lipo, and ^{64}Cu -Eu/VBBO lipo at different activities of ^{64}Cu ($n = 6$, mean \pm s.d.). d) Microscopic cell images of ^{64}Cu -Eu lipo, ^{64}Cu -VBBO lipo, and ^{64}Cu -Eu/VBBO lipo at different activities of ^{64}Cu after the in vitro PDT (Scale bar: 5 μm). *: $P < 0.05$, **: $P < 0.01$, ***: $P < 0.001$. The one-way ANOVA followed by Tukey post hoc test was conducted for statistical analysis.

2.3.5 Efficient tumor targeting by EPR effect

In vivo positron emission tomography (PET) imaging was performed to demonstrate the imaging ability of ^{64}Cu -Eu/VBBO lipo and confirm the passive targeting efficiency of the NPs in FaDu xenograft tumor mouse model (**Figure 2.16 a**). The image revealed the substantially long circulation half-life and efficient tumor targeting ability of ^{64}Cu -Eu/VBBO lipo. Quantified PET uptakes of major organs are shown in **Figure 2.16 b**. The uptake of the tumor gradually increased to 19.29 ± 4.70 %ID/g 48 h after the injection. The circulation half-life of ^{64}Cu -Eu/VBBO lipo was 20.15 h (**Figure 2.16 c**). Tumor to background (muscle, blood pool, and liver) ratios increased gradually over time until 48 h after the injection up to 16.77, 2.53, and 0.55 folds, respectively (**Figure 2.16 d-f**). Additionally, ^{64}Cu -VBBO lipo showed a similar biodistribution with ^{64}Cu -Eu/VBBO lipo, and there was no

significant difference regarding tumor uptake between ^{64}Cu -VBBO lipo and ^{64}Cu -Eu/VBBO lipo at all time points ($P = 0.07, 0.788, 0.688, 0.625$, and 0.237) (**Figure 2.17**).

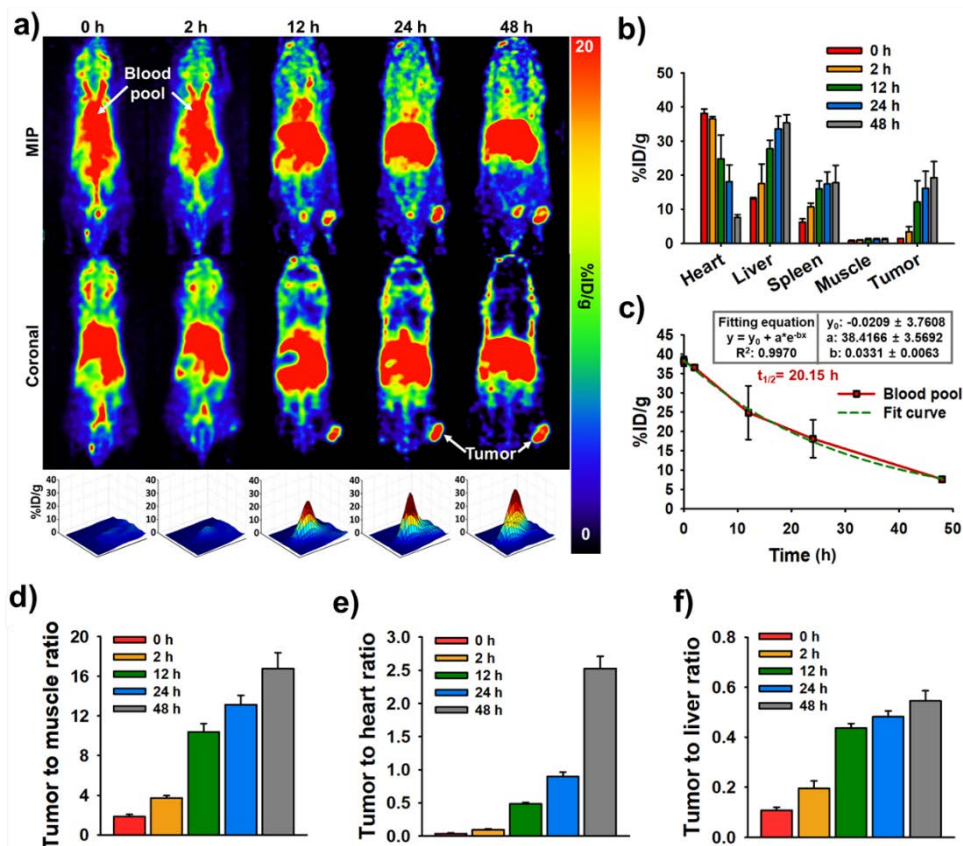


Figure 2.16 In vivo PET imaging and quantitative analysis for assessment of passive targeting efficiency of ^{64}Cu -Eu/VBBO lipo. a) PET images of FaDu tumor bearing xenograft mouse model (n = 4) at different time points (0, 2, 12, 24, and 48 h) after intravenous injection of ^{64}Cu -Eu/VBBO lipo (upper row: maximal intensity projection (MIP), middle row: coronal, lower row: surface plot for the tumor area from the coronal image, z axis: %ID/g). b) Quantification analysis of various organs and tumors at each time point (n = 4, mean \pm s.d.). c) Time activity curve of the

blood pool and circulation half-life ($n = 4$, mean \pm s.d.). d), e), and f) Tumor targeting efficiency compared to 3 non-target areas (muscle, heart and liver) ($n = 4$, mean \pm s.d.).

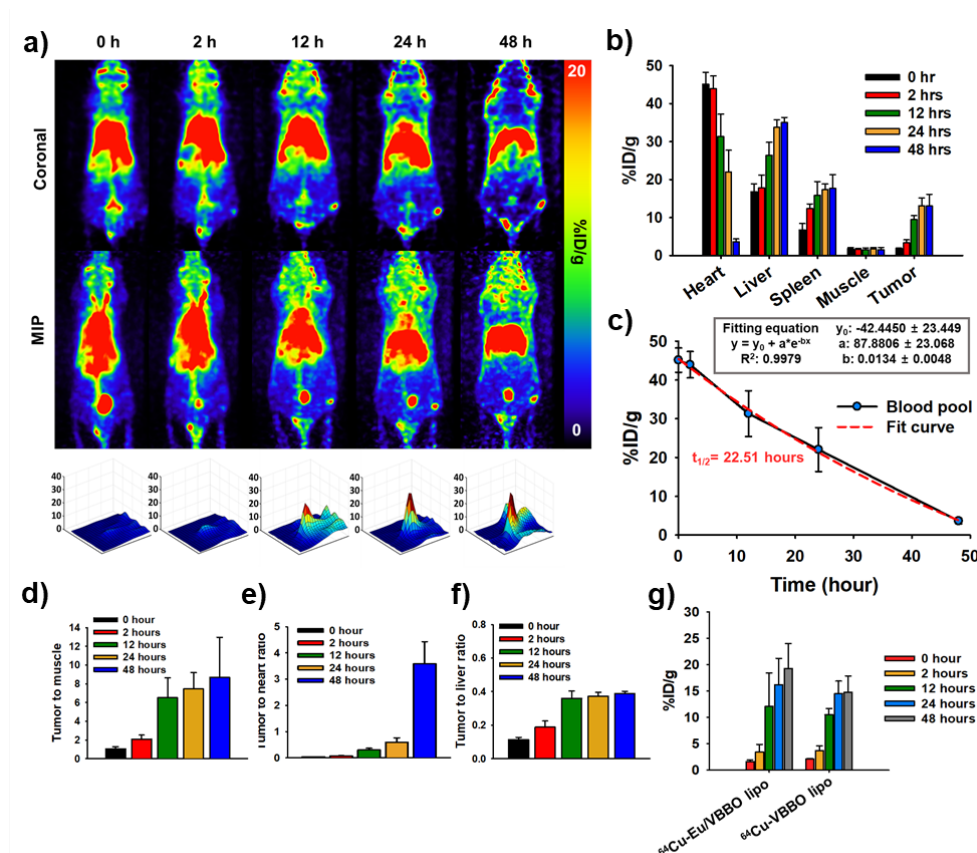


Figure 2.17 In vivo PET imaging for blood pool circulation and passive targeting efficiency of ^{64}Cu -VBBO lipo. a) PET scanned images at different time points (0, 2, 12, 24, and 48 h) and quantification analysis of tumor regions at each time point based on the PET scanned coronal images. b) Quantification analysis of various organs and tumor at each time point. c) Time activity curve of the blood pool at different time points. The circulation half-life ($t_{1/2}$) was about 22.51 h. d), e), and the f) tumor targeting efficiency compared to 3 different types of organs. g) The

tumor uptake at each time point between ^{64}Cu -Eu/VBBO lipo and ^{64}Cu -VBBO lipo was not statistically significant. ($P = 0.07, 0.788, 0.688, 0.625, \text{ and } 0.237$).

X-ray-induced PDT and Cerenkov luminescence-induced PDT have been shown to have good therapeutic effects in previous studies.^{18, 23, 24, 28} However, these NPs were injected intratumorally in most of the studies probably because of their low tumor targeting efficiency.^{18, 23, 28, 30} Kotagiri et al. reported that intravenously injected nanomicelles containing PS were utilized for Cerenkov radiation induced therapy. Although the quantitative tumor targeting efficiency was not reported, the circulation half-life of the nanomicelles was shorter than that of our liposome nanoplatform (123 min vs. 20 h).⁶⁹ In a recent study, magnetic NPs were intravenously injected for Cerenkov luminescence induced PDT and the tumor uptake was around 5 %ID/g without targeting and 15.2 %ID/g with the application of an additional magnetic field.¹⁰ We utilized a PEGylated liposome-based nanoplatform for enhanced EPR effects and found that our liposome nanoplatform had an excellent tumor targeting efficiency (~ 19 %ID/g) without any additional targeting strategy.

2.3.6 Effective in vivo PDT of ^{64}Cu -Eu/VBBO lipo

In vivo PDT was conducted by intravenous injection of ^{64}Cu -Eu/VBBO lipo ($n = 4$) and ^{64}Cu -VBBO lipo ($n = 4$) in a FaDu xenograft tumor mouse model. Normal saline ($n = 4$) and Eu/VBBO lipo ($n = 4$) were injected and these groups were used as the control groups. The ^{64}Cu -VBBO lipo and ^{64}Cu -Eu/VBBO lipo groups had higher therapeutic effects than the control groups. Furthermore, the ^{64}Cu -Eu/VBBO lipo had a better therapeutic effect than the ^{64}Cu -VBBO lipo group (**Figure 2.20 a-**

c). Thus, radioluminescence-induced PDT with ^{64}Cu -Eu/VBBO lipo had a higher tumor growth suppression ability than Cerenkov luminescence-induced PDT effect with ^{64}Cu -VBBO lipo in vivo. This difference can be attributed to the difference in efficiency between RET and CLET, because there was no significant difference in tumor uptake between ^{64}Cu -Eu/VBBO lipo and ^{64}Cu -VBBO lipo (**Figure 2.17**). Major organs and tumor tissues were collected 48 h after intravenous injection of ^{64}Cu -Eu/VBBO lipo. No significant histologic damage was found in the heart, liver, spleen and thigh muscle on histological observation (**Figure 2.20 c**).

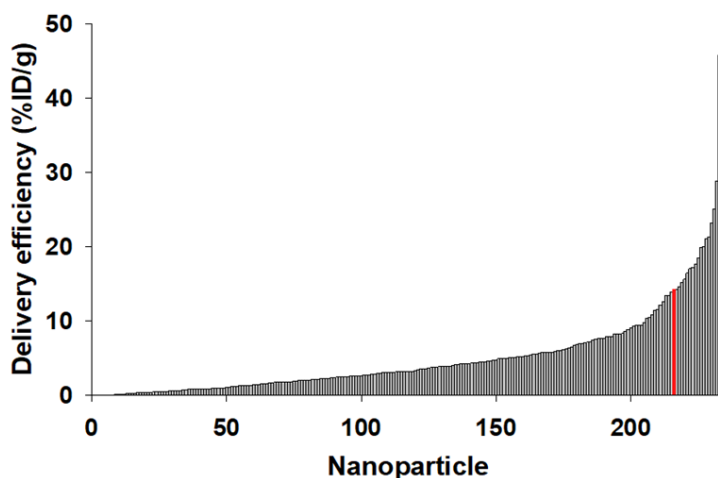


Figure 2.18 Delivery efficiency profile of various nanoparticles for in vivo targeting to the target tumor region. Red bar indicates Eu/VBBO lipo nanopatform (14.13 %ID/g, mean targeting efficiency: 4.91 %ID/g).

The effectiveness of PDT is normally determined by the targeting efficiency of PS, oxygen concentration of tissue and delivered energy of light.⁷⁰ The PS delivery system has been extensively studied and includes liposome based, polymer, silica, gold, and iron oxide NPs.^{71, 72} In our system, we utilized a PEGylated liposome

nanoplatform for efficient tumor targeting and we found that the tumor uptake of our nanoplatform reached up to 19 %ID/g. This targeting efficiency is considerably high, within top 10%, compared to the previously reported targeting efficiencies of various NPs especially with or without targeting moieties (median = 3.17 %ID/g) (**Figure 2.18-2.19**).⁷³

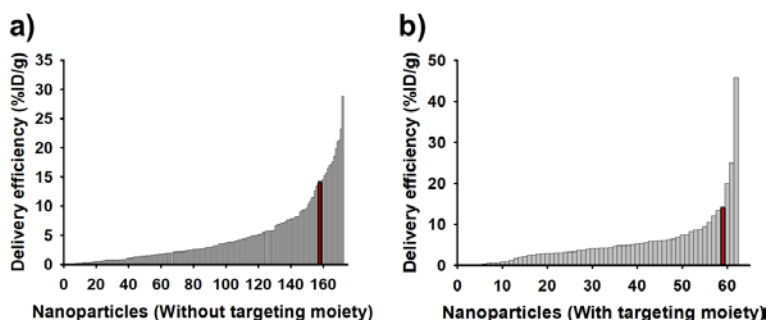


Figure 2.19 Delivery efficiencies of the nanoparticles with or without targeting moiety. a) Nanoparticles without targeting moiety for passive targeting. b) Nanoparticles with targeting moiety for active targeting. Red bars indicate Eu/VBBO lipo nanoparticles.

The effect of PDT is also dependent on the dose of light (J/cm^2), which is calculated by the multiplication of irradiance (W/cm^2) and time (second).⁷⁴ Currently two types of ionizing radiation-induced PDT strategies, X-ray- and radioisotope-induced PDT, are under investigation. The dose of light for these methods are dependent on the radiation dose. X-ray-induced PDT has the advantage of providing a high radiation dose at tumor focus within a short duration of time (1 ~10 Gy per minute).²⁵ However, such a large amount of energy may be harmful to the surrounding normal tissue, and the high fluence of radioluminescence from the NPs may deplete the oxygen within the tumor, which will lead to the decreased efficiency

of the PDT. However, radioisotope-induced PDT has the advantage of an emission of low fluence rates of light over a long period of time (half-lives of the utilized radioisotopes for PDT: ^{64}Cu = 12.7 h, ^{89}Zr = 78.4 h, ^{18}F = 110 min).⁷⁵ Previous studies on radioisotope-induced PDT have focused on the Cerenkov luminescence-induced PDT.^{52, 69, 76} In our study, we utilized the scintillating Eu-DTPA for radioluminescence-induced PDT and found that the radioluminescence had a 2-fold higher luminescence intensity and a transfer efficiency that was 6-fold higher in radioluminescence than Cerenkov luminescence (65% vs. 11%) mainly because of the efficient resonance energy transfer in RET. Above all, based on the in vivo PDT results, the therapeutic effect of ^{64}Cu -Eu/VBBO lipo was the highest through passive targeting ability to the tumor. However, although the liver and spleen, which are normal organs, showed high uptake of ^{64}Cu -Eu/VBBO lipo, the tissue sectioned image after treatment showed almost no damage to the normal organs based on the in vivo PET scanned images. These results appeared to be due to the genetic instability of cancer. Genetic instability is one of several cancer hallmarks in many types of cancers. In the case of normal cells, when DNA is damaged due to various factors such as free radicals, cellular metabolism, replication errors, ionizing radiation, UV-light, and toxic chemicals, they survive without leading to apoptosis through DNA repair called DNA damage response (DDR) pathway. Meanwhile, cancer cells lack DDR due to genetic instability, which leads to cell death without recovering DNA damage⁷⁷⁻⁸⁰. Therefore, when photodynamic therapy was performed through the ^{64}Cu -Eu/VBBO lipo developed in this study, the ROS generated from VBBO might cause the DNA damage in cancer cells. Because of the genetic instability of cancer cells, the absence of DRR leads to apoptosis, leading to the death of cancer cells. On the other hand, although ^{64}Cu -Eu/VBBO lipo showed a

high uptake rate in the liver and spleen, which are normal organs, it was expected that it would receive relatively less long-term damage through the DNA repair process through the DDR mechanism of normal cells. Thus, we believe radioluminescence-induced PDT holds promise for future ionizing radiation-induced PDT.

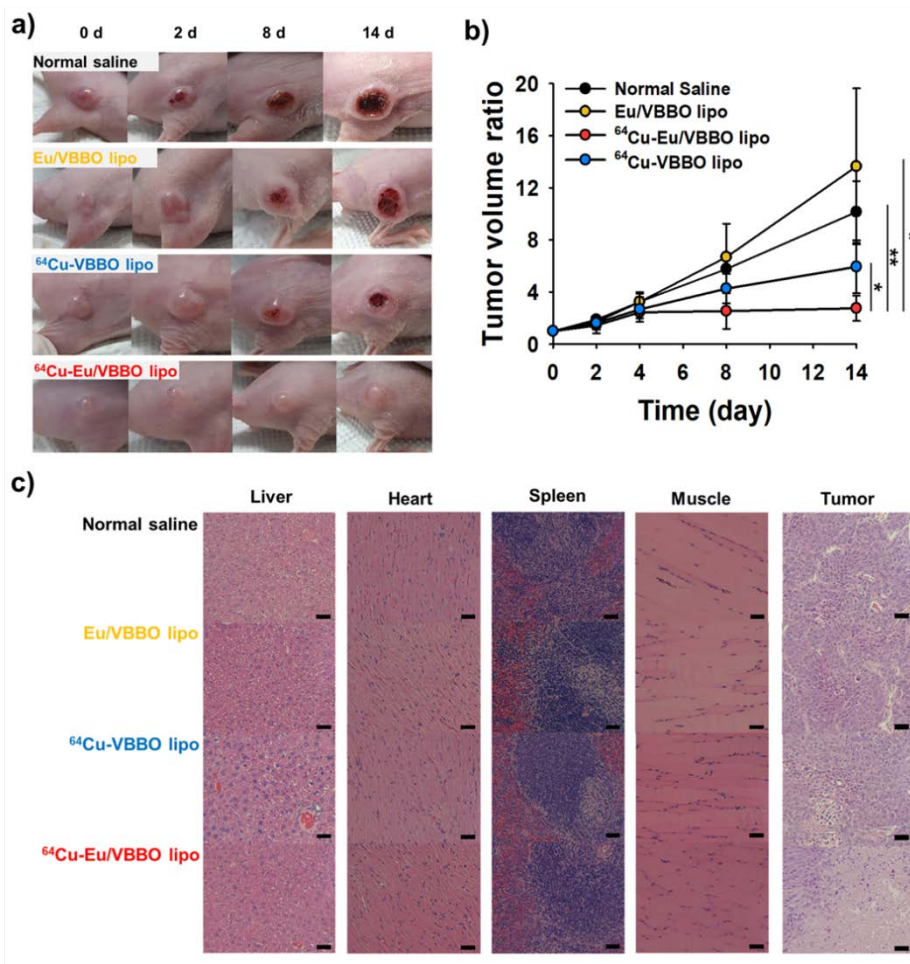


Figure 2.20 In vivo photodynamic therapy. a) Tumor follow-up images in FaDu tumor bearing xenograft mouse model after intravenous injection of ^{64}Cu -Eu/VBBO lipo (n = 4), ^{64}Cu -VBBO lipo (n = 4), Eu/VBBO lipo (n = 4), or normal saline (n = 4). b) Tumor volume ratio after the treatments (mean \pm s.d.). *: P < 0.05, **: P <

0.01. The Student's t test was conducted for statistical analysis. c) H&E stained major organs and tumor histological images at 14 d after the treatments.

Recently, there has been huge success in targeted radioisotope therapy in neuroendocrine tumor and castration resistant prostate cancer. In 2017, a phase 3 trial of ^{177}Lu -DOTATATE (Lutathera) for midgut neuroendocrine tumors showed markedly longer progression-free survival than octreotide treatment.⁸¹ Furthermore, ^{177}Lu -PSMA agents have shown significantly better therapeutic effects than the other third line therapeutics for castration resistant prostate cancer.⁸² These therapeutic radioisotope based therapeutics are found to be very effective, but have adverse effects including nephrotoxicity, hematologic toxicity, and salivary gland dysfunction caused by high radiation doses.⁸¹⁻⁸³ Radioisotopes for imaging purpose, such as ^{64}Cu and $^{99\text{m}}\text{Tc}$, can exert PDT effects by combination with our radioluminescence PS loaded liposome nanoplatform. In this study we created a radioluminescence liposome nanoplatform that could be combined with radioisotope-based therapy to reduce adverse effects of therapeutic radioisotopes by reducing the dose or using the less toxic diagnostic radioisotope for the therapy.

We explored if Eu^{3+} caused toxicity in vivo. The intraperitoneal LD50 of EuCl_3 is 550 mg/kg.⁸⁴ Also, Ogawa et al. reported that no-observed-effect level of EuCl_3 is 200 mg/kg/day.⁸⁵ In our experiment, Eu^{3+} was used 40 mg/kg in mouse, which is one fifth of the no-observed-effect dose. Furthermore, Eu^{3+} was chelated by DTPA in our experiment. It is known that lanthanide chelates are less toxic than lanthanide ions. For example, the toxicity of ScCl_3 is dramatically reduced when it is chelated with EDTA (LD50: ScCl_3 = 24, Sc-EDTA = 108 mg).²⁸ Also, Gd ion is toxic but Gd-chelates are safely used in the clinic for MRI contrast agents (LD50 of Gd is 0.5

mmol/kg while that of Gd-DTPA is 10 mmol/kg).^{86, 87} We further explored the metabolism of Eu^{3+} using Inductively Coupled Plasma Mass Spectrometry (ICP-MS) in the major organs at 2 and 14 days after the intravenous injection of Eu/VBBO lipo ($\text{Eu}^{3+} = 40 \text{ mg/kg}$). On day 2, ICP-MS measured Eu concentrations of liver ($298.67 \pm 82.86 \text{ ppm}$) and spleen ($189.33 \pm 22.14 \text{ ppm}$) were similar with the calculated concentration of Eu from the %ID/g in PET imaging ($283.04 \pm 8.81 \text{ ppm}$ and $142.64 \pm 23.72 \text{ ppm}$, respectively).

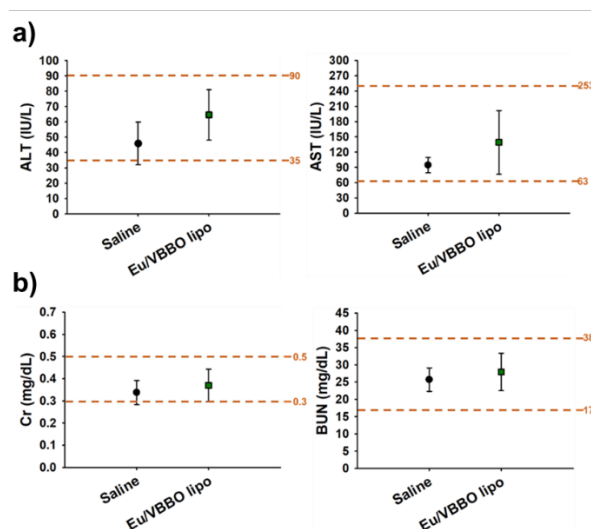


Figure 2.21 Blood test for the toxicity evaluation of the Eu/VBBO lipo. a) Alanine transaminase (ALT) and aspartate transaminase (AST) values in normal saline as a control and the Eu/VBBO lipo for the liver function. b) Creatinine (Cr) and blood urea nitrogen (BUN) values in the control and the Eu/VBBO lipo for the kidney function. Dash lines are indicated normal value ranges in normal mice.

On day 14, Eu concentrations of the liver and spleen dramatically decreased to less than one hundredth and one thirtieth, respectively, compared to those on day 2.

Also, Eu element was found in the kidney on day 2 but not detectable on day 14 (**Figure 2.22**). Thus, we assume that the Eu-DTPA was excreted efficiently through kidney after dissociation from the injected Eu/VBBO lipo.

Furthermore, the hepatic and renal toxicity of Eu/VBBO lipo were also assessed by measuring the blood urea nitrogen (BUN), creatinine (Cr), alanine transaminase (ALT) and aspartate transaminase (AST) 14 days after injection of Eu/VBBO lipo ($\text{Eu}^{3+} = 40 \text{ mg/kg}$) or normal saline in the normal BALB/c nude mouse ($n = 4$, and 4, respectively). The measured BUN, Cr, ALT and AST of all mice were within the normal range and there was no significant difference between saline and Eu/VBBO lipo injected groups, indicating that there is no observable renal or hepatic toxicity by Eu/VBBO lipo injection (**Figure 2.21**).

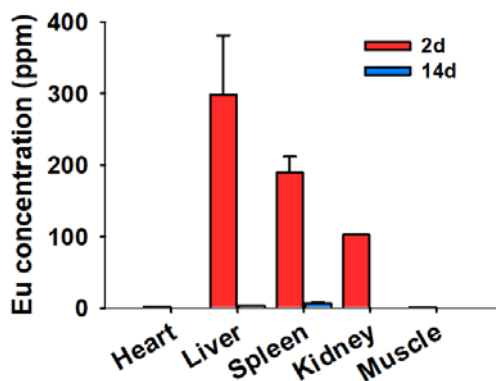


Figure 2.22 Quantitative analysis of the Eu in major organs at 2 and 14 days with ICP-MS.

Although we observed no overt tissue or biochemical toxicity in the major organs in our experiment, it is possible that ^{64}Cu -Eu/VBBO lipo accumulation may damage normal tissue. Thus, dividing switch (radiolabeled targeting tracer) and effector

(Eu/PS lipo) may provide further merits regarding the safe utilization of the radioluminescence liposome nanoplatform. One potential approach would be the combination of radioluminescence / PS liposome nanoplatform (effector) with established immunoPET agents (switch) to convert diagnostic PET agents into therapeutics. In this study, the liposome nanoplatform was produced by film method followed by sonication which is hard to be scaled-up.⁸⁸ The strategies for the large-scale production of the nanoplatform is warranted for the future translational research.

2.4 Summary

We developed, here, an Eu-DTPA and PS loaded liposome nanoplatform for effective in vivo imaging and radioisotope-induced PDT. We found that our liposome nanoplatform presented 1) strong radioluminescence and characteristic X-ray emission, 2) efficient energy transfer from Eu-DTPA to PS, 3) high tumor targeting efficiency, and 4) effective ROS generation and in vitro/in vivo PDT effect. Furthermore, we found that radioluminescence-induced PDT was superior to Cerenkov-induced PDT in our experimental setting. Thus, our nanoplatform may be a promising tool for radioisotope-induced PDT. We expect that our liposome nanoplatform can be further utilized to enhance the efficacies of X-ray therapy or targeted radioisotope therapy.

This paper was already published at ACS nano and selected as supplementary cover article. (Lee, Wooseung, et al. "Europium-diethylenetriaminepentaacetic acid loaded radioluminescence liposome nanoplatform for effective radioisotope-mediated photodynamic therapy." ACS nano 14.10 (2020): 13004-13015.)

Chapter 3. Photodynamic Therapy Induced by a Combination of Scintillating Liposome and Radiolabeled Antibody

3.1 Background

In previous studies, the nanoplatform for radio isotope-induced PDT using strong RL overcomes the light transmittance problem of the PDT initiator, which was a limitation of conventional PDT, by using radioisotopes, and also increased in vivo stability by embedding PS into liposomes. In addition, by designing a liposome structure as the main structure of the nanoplatform, high circulating ability in vivo and high passive cancer targeting ability were verified. Through strong radioluminescence emission in the presence of a radioisotope of a lanthanide metal called europium, the PDT effect was superior to that of Cerenkov luminescence induced PDT. However, although previous studies had excellent performance in nanomedicine-based radiation induced PDT, the developed liposome was highly accumulated not only in tumors but also in normal organs such as liver and spleen after in vivo injection.

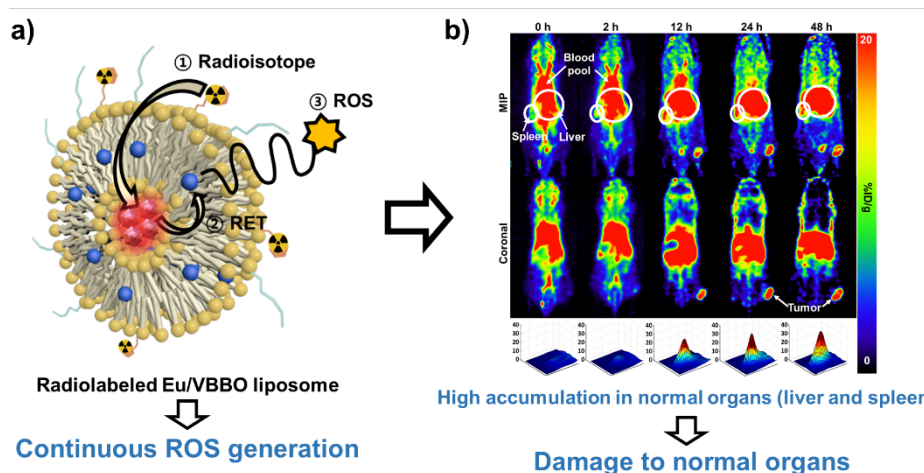


Figure 3.1 Previous developed radiolabeled nanoplatform and biodistribution images. a) Characteristics of ^{64}Cu -Eu/VBBO lipo. b) Biodistribution PET scanned images of ^{64}Cu -Eu/VBBO lipo.

The liposome clearance was occurred in the blood pool by reticuloendothelial system (RES) which was composed of resident phagocytic cells in local tissues such as liver and spleen. The developed ^{64}Cu -Eu/VBBO lipo had a structure in which ROS was always generated because ^{64}Cu was labeled on the surface of the liposome. Therefore, when ^{64}Cu -Eu/VBBO lipo was accumulated at a high rate in normal organs due to RES, it had a limitation in that it can damage the accumulated normal organs as in tumors. To overcome the adverse effect which had a potential to damage in normal organs due to the accumulation of radiolabeled Eu/VBBO lipo, antibody was selected as a carrier for the radioisotope delivery. Although the radioisotope is labeled with a cancer-specific antibody and separated from the previously developed liposome structure, it was expected that the ionizing radiation transfer efficiency to Eu^{3+} would be maintained because there is almost no limit to the tissue permeability of ionizing radiation. Radiolabeled antibodies have been extensively studied by

labeling the radioisotope such as ^{64}Cu , ^{111}In , and ^{177}Lu for diagnosis or treatment to tumors (**Figure 3.2**)⁸⁹⁻⁹¹.

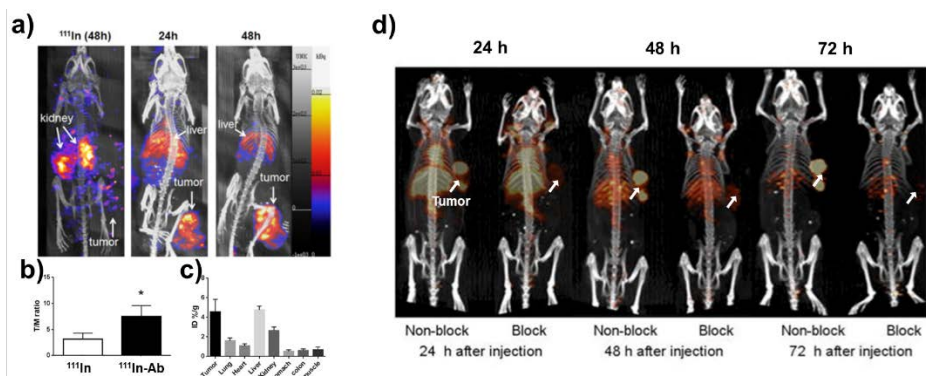


Figure 3.2 In vivo nuclear medicine imaging of radiolabeled antibody. a) In vivo PSECT /CT imaging of ^{111}In and ^{111}In labeled antibody (^{111}In -Ab). b) Tumor to muscle ratio comparison between free ^{111}In and ^{111}In -Ab. c) Quantitative analysis of ^{111}In -Ab in major organs and tumor. White arrows are indicated liver, kidney, and tumor, respectively (reproduced from Shih, et al.)⁹⁰. d) In vivo PET imaging of ^{64}Cu labeled antibodies with and without blocking at various time points (24, 48, and 72 h) (reproduced from Guo, et al.)⁹¹.

Radiolabeled antibodies are used for diagnostic or therapeutic research through its active targeting ability to specifically bind to an overexpressed receptor protein on the surface of target tumor. Moreover, antibodies have a significantly high active targeting ability against target tumors in vivo, and their uptake in other normal organs is relatively low, unlike the in vivo distribution of other nanoparticles. Therefore, to overcome the limitations of the existing liposome nanoplatform, we developed a combinatorial photodynamic therapy system using two nanoprobes and conducted a study aimed at increasing the therapeutic effect. One of the two nanoprobes was

Eu/VBBO lipo, and the other was designed as a radioisotope-labeled antibody and studies were conducted. In the case of the radioisotope used, in this study, ^{177}Lu , a radioisotope for treatment, was used to increase the effect of PDT. The quality of Eu/VBBO lipos was verified through size, uniformity, and dispersion stability as in previous studies. Trastuzumab and cetuximab were used as antibodies in the study, and the cancer-specific binding ability to each cancer cell line was verified for subsequent in vitro and in vivo studies. RL imaging and RL energy transfer efficiency studies were conducted through the combination of ^{177}Lu -Tz and Eu/VBBO lipo. Based on the RL imaging results, imaging on the degree of ROS generation and in vitro PDT were performed to confirm the therapeutic effect in cancer cell lines. Through fluorescence and nuclear medicine imaging, we confirmed and verified the effective circulation and cancer targeting ability of Eu/VBBO lipo and antibodies in xenograft mouse models. Finally, a study was conducted to confirm the effect of PDT in vivo in a xenogeneic tumor transplantation mouse model using a combinatorial photodynamic therapy system.

3.2 Experimental methods

3.2.1 Materials

Cholesterol, Europium chloride · 6H₂O, victoria blue-BO, and diethylene-triaminepentaacetic acid (DTPA) were purchased from Sigma-Aldrich (Missouri, USA). 1,2-distearoyl-sn-glycero-3-phosphocholine (DSPC) and 1,2-distearoyl-sn-glycero-3-phosphoethanolamine-N-[amino(polyethylene glycol)-2000] (DSPE-PEG(2000)-NH₂) were obtained from Avanti Polar Lipid, Inc (Alabama, USA). 1,2-distearoyl-sn-glycero-3-phosphoethanolamine (methyl(2-hydroxyethyl)polyethyleneglycol-5000) (DSPE-mPEG(5000)) was acquired from Creative PEGWorks (North Carolina, USA). Sodium acetate, citric acid, and 1X PBS tablet were purchased from Sigma-Aldrich (Missouri, USA). Dimethyl sulfoxide (DMSO) was purchased from DAEJUNG CHEMICALS & METALS Co., Ltd (Busan, Korea). 2-(p-Isothiocyanatobenzyl)-1,4,7-triazacyclononane-N,N',N'',N'''-triacetic acid trihydrochloride ((p-SCN-Bn)-NOTA) was also purchased by FUTURECHEM (Seoul, Korea). CellROX™ Green Reagent and Alexa Fluor™ 647 NHS Ester (Succinimidyl Ester) was obtained from Invitrogen (Carlsbad, CA, USA) for fluorescent labeling. Dulbecco's Modified Eagle Medium (DMEM), fetal bovine serum (FBS), and PD-10 desalting column were acquired from Cytiva, (Marlborough MA, USA). Hoechst 33342 was purchased from Thermo Fisher Scientific (Waltham, MA, USA). ViaFluor® 488 Live Cell Microtubule Staining Kit was purchased from Biotium (Fremont, CA, USA) to stain the cytoplasm of cancer cells. 1,1'-diiodo-3,3',3''-tetramethylindodicarbocyanine, 4-chlorobenzenesulfonate salt (DiI) and MitoTracker™ Red^{FM} (Mitotracker) were

obtained from Invitrogen (Carlsbad, CA, USA) for confocal fluorescence imaging. Female BALB/c nude mice (6-8 weeks) were obtained from Orient Bio (Seongnam, South Korea).

3.2.2 Instruments

All sizes of Eu/PS liposomes were measured using a dynamic light scattering instrument (DLS, ZETASIZER Nano ZS, Malvern Instrument Ltd., Worcestershire, UK). The TEM images of the liposomes were obtained using a Transmission Electron Microscope (TEM, TALOS L120C, FEI company, Oregon, USA) to confirm their morphologies and sizes. Fluorescence and absorbance signals were obtained using a microplate reader (SYNERGY H1, BioTek, Vermont, USA). For *in vitro* and *in vivo* Cerenkov and radioluminescence imaging, the *in vivo* imaging system (IVIS 100, Perkin Elmer, Massachusetts, USA) was used. The PET images were acquired by a PET scanner (GENISYS4, Sofie Bioscience, California, USA) after intravenous injection of ^{64}Cu labeled Eu lipo, VBBO lipo and Eu/VBBO lipo in tumor bearing mice. SPECT and CT scanned images were obtained by SPECT/CT scanner (NanoSPECT/CT plus, Mediso, Budapest, Hungary).

3.2.3 Preparation of Eu and VBBO co-loaded liposome nanoparticle (Eu/VBBO lipo)

The liposome loaded DTPA chelated Eu and VBBO into a hydrophilic core and a hydrophobic membrane part respectively was prepared by the previous report⁹². Briefly, Eu^{3+} dissolved in DI water was reacted with DTPA in 0.5 M NaOH solution. After pH adjustment as neutral pH, DTPA chelated Eu^{3+} (Eu-DTPA) was used for hydration media to assemble the liposomal nanoparticle. DSPC, DPSE-PEG5k, and

cholesterol were weighed in a ratio of 6.6:1.3:1.6 for the lipid film. The lipids were dissolved in methanol and chloroform mixed solution (v/v, 2:1), and mixed solvent with the lipids were evaporated by N₂ purging for arrangement of the lipid film. The VBBO was added during lipid dissolution. The arranged lipid thin film including VBBO was vacuumed for 24 hours in the vacuum chamber for removal of the residual solvent to ease the hydration procedure. VBBO containing lipid film was hydrated with Eu-DTPA solution before the ultra-sonication. The hydrated multilamellar vesicles were ultrasonicated with the pulse stimulation in each step to form unilamellar vesicles referred as the liposomal structure. After the sonication, the Eu/VBBO lipo was filtered by a syringe filter with 0.22- μ m pore size. The filtered Eu/VBBO lipo was purified with membrane filter tube by centrifugation to remove unencapsulated Eu-DTPA and excess free VBBO molecules.

3.2.4 Fluorescent dye and chelator modification with Eu/VBBO lipo and therapeutic antibodies (Tz and Ctx)

Therapeutic antibodies were modified with fluorescent molecules including amine reactive moiety such as Alexa Fluor™ 647 NHS ester or FITC for further in vitro and in vivo studies. The antibody was purified to remove preservative materials such as polysorbate 80, tween 20, and other surfactants before the reaction with Alexa Fluor™ 647 NHS ester. The purified antibody was collected by a diluted PBS solution. Alexa Fluor™ 647 NHS ester was simply mixed with the antibody solution at the neutral pH and reacted for overnight at 25°C. The Alexa Fluor™ 647 modified antibody was purified by a size exclusion chromatographical method after the reaction. For the fluorescent liposome, 1 mM DiD in ethanol was simply added into the Eu/VBBO lipo and reacted for 1 hour followed by purified with the size

exclusion chromatographical method. Chelators such as (p-SCN-Bn)-NOTA or (p-SCN-Bn)-DOTA were also proceeded in the same way as in the method of attaching fluorescent molecules. In case of the Eu/VBBO lipo, the liposome was prepared by adding an amine group as in the previous study to modified with the (p-SCN-Bn)-NOTA.

3.2.5 Size measurement and stability test of Eu/VBBO lipo under the physiological conditions

Hydrodynamic size and stability in the different media were demonstrated based on DLS measurement. The hydrodynamic size of Eu/VBBO lipo was measured after the purification with DI water. Stability study was conducted in PBS, human serum, and cell culture media (RPMI 1640). Photographic images of the stability demonstration were obtained up to 7 days. hydrodynamic size of the Eu/VBBO lipo in PBS solution was measured for 14 days by DLS to confirm long-term stability.

3.2.6 Radioisotope labeling of Eu/VBBO lipo and therapeutic antibodies (Tz and Ctx)

37 MBq of ^{177}Lu was adjusted to pH 5 with 2 M sodium acetate solution for the radiolabeling with the DOTA moieties. The pH 5 adjusted ^{177}Lu solution was added into the DOTA modified antibodies. The mixture was reacted for 1 hour at 37°C . ^{177}Lu labeled antibodies were purified by the size exclusion chromatographical method after the reaction. The purified sample was collected and conducted radio-thin layer chromatography (Radio-TLC) for radio-stability study up to 72 hours. ^{64}Cu labeling for in vivo PET imaging with Eu/VBBO lipo and antibodies was also carried out in the same manner as for ^{177}Lu labeling procedure.

3.2.7 Radioluminescence (RL) and RL energy transfer efficiency imaging

Radioluminescence imaging was conducted with various samples (DW, Eu lipo, Eu/VBBO lipo, ^{177}Lu -Tz (100 μCi), ^{177}Lu -Tz (100 μCi) + Eu lipo, and ^{177}Lu -Tz (100 μCi) + Eu/VBBO lipo) by IVIS. RL energy transfer imaging was also performed with increasing amounts of Eu and VBBO (Eu^{3+} : 0, 1.1, 2.75, 5.5 mg, VBBO: 0, 0.⁶⁴, 1.28, 2.56 μg) by IVIS. The numeric graph was obtained based upon the RL and RL energy transfer imaging.

Cerenkov luminescence (CL), radioluminescence (RL), and RL energy transfer (RET) were evaluated based on the quantitative analysis method of previous report as follows⁹²:

CL is free ^{177}Lu luminescence signal, and RL is luminescence intensity of (^{177}Lu -Eu lipo – free ^{177}Lu) corresponding to the RL1 for RET calculation.

$\text{RET} = 1 - \text{RL2}/\text{RL1}$, where RL1 means the light emission intensity of RL itself, and RL2 is luminescence signal of [^{177}Lu -Eu/VBBO lipo + (free ^{177}Lu - ^{177}Lu -VBBO lipo)].

3.2.8 In vitro active targeting fluorescence imaging of therapeutic antibodies with confocal microscope

Human epidermal growth factor receptor 2 (HER2) related cancer cell lines, SKOV-3 ovarian cancer cell line (HER2+) and 4T1 breast cancer cell line (HER2-), were seeded in confocal dishes respectively with 10^4 cells / dish and incubated at 5% CO_2 atmosphere and 37°C for 24 hours. FITC immobilized Tz (FITC-Tz) was treated to each cancer cell lines and incubated for 2 hours after the addition. The excess fluorescent Tz was removed by DPBS washing step and stained with Hoechst 33342 (5 μM) and mitotracker (1 μM) for 30 minutes. The staining dyes were removed by

DPBS for several times before the confocal microscope imaging. CT-26 colon cancer cell line known as epidermal growth factor receptor (EGFR) overexpressed cancer cell line was cultured and seeded in confocal dish with 10^4 cells / dish and incubated at 5% CO₂ atmosphere and 37°C for 24 hours. Alexa Fluor™ 647 immobilized Ctx (Alexa Fluor™ 647-Ctx) treatment was conducted in the same procedure as FITC-Tz fluorescence imaging. Alexa Fluor™ 647-IgG was utilized as a control. Hoechst 33342 (5 µM) and ViaFluor® (1 µM) were added for nuclei and cytoplasm staining.

3.2.9 In vitro active targeting fluorescence imaging of therapeutic antibodies by flow cytometry

SKOV-3 (HER2+) and 4T1 (HER2-) were cultured and collected respectively with 10^3 cells in each sample. All the sample preparation was conducted at 4°C environments. 1% of BSA containing 1X PBS solution was added into each sample and incubated for 30 minutes at 4°C. Tz was treated into both cell lines for primary antibody treatment after the BSA blocking. Alexa Fluor™ 647 modified secondary antibody was treated for conjugating with Tz and conducting the flow cytometry. EGFR overexpressed CT-26 was cultured and collected respectively with 10^3 cells. Sample preparation before and after the Alexa Fluor™ 647-Ctx and Alexa Fluor™ 647-IgG treatment step was in the same way as in the method with the Tz.

3.2.10 In vitro ROS production study

SKOV-3 (HER2+) was cultured and seeded in confocal dishes with 10^4 cells / dish and incubated at 5% CO₂ atmosphere and 37°C for 24 hours. Different kinds of nanoprobe; Eu/VBBO lipo, ¹⁷⁷Lu-Tz (10 µCi), ¹⁷⁷Lu-Tz (100 µCi), ¹⁷⁷Lu-Tz (10 µCi) + Eu/VBBO lipo were treated into the cell attached confocal dishes respectively after

the cell incubation and exchanging with fresh cell media. All the sample was further incubated for 4 hours at 5% CO₂ atmosphere and 37°C condition and added 1 µM Cell ROX reagent and Hoechst 33342 for the ROS detection and nuclei staining. Optical fluorescence microscope imaging was conducted with 20x objective magnification after DPBS washing for several times.

3.2.11 Cytotoxicity study without therapeutic radioisotope

SKOV-3 (HER2+) was cultured and seeded into a 96-well microplate with 10³ cells / well and incubated for overnight to attach the cells at 5% CO₂ atmosphere and 37°C. Eu/VBBO lipo with free Tz while increasing the concentration of VBBO (0, 1.56 x 10⁻⁷, 1.56 x 10⁻⁶, 1.56 x 10⁻⁵, 1.56 x 10⁻⁴, 6.25 x 10⁻⁴, 2.50 x 10⁻³, 1.00 x 10⁻², 2.00 x 10⁻², 4.00 x 10⁻², 8.00 x 10⁻², 1.60 x 10⁻¹ µg) was treated in each well respectively (n=3). Eu/VBBO lipo with free Tz treated cells were further incubated for 24 hours followed by conducting DPBS washing. 0.5 mg/mL of MTT solution was added and incubated for 2 hours at 37°C. DMSO was treated into all samples after removal of MTT solution and washing for 3 times with DPBS. All the samples were measured their absorbance at 540 nm and evaluated cell viability based on the absorbance value.

3.2.12 In vitro PDT study

SKOV-3 (HER2+) was cultured and seeded into a 96-well microplate with 10³ cells / well and incubated for the cell attachment. After the cell incubation, various samples as in the Table 1. below were treated into the cells respectively (n=3) and incubated for 24 hours. 0.5 mg/mL of MTT solution was added and incubated for 2 hours at 37°C after the DPBS washing for complete removal of the residual ¹⁷⁷Lu-

Tz or Eu/VBBO lipo. The samples were measured the absorbance at 540 nm by the 96-well microplate reader after the DMSO treatment and evaluated cell viability based on the absorbance value.

Table 1.

Eu³⁺ (mg)	0	0.8	0	0	0.8	0.8	0.8
VBBO (μg)	0	0.16	0	0	0.016	0.08	0.16
¹⁷⁷Lu (μCi)	0	0	10	50	10	10	10

3.2.13 Preparation of mouse tumor model

SKOV-3 and CT-26 cancer cells were cultured and collected in DPBS solution with a concentration of 10^5 cells / 10 μL. Each collected cell line was injected subcutaneously into the right thigh of BALB/c nude mice respectively. In vivo imaging was carried out 3 weeks after the injection of cancer cells, and in the case of the treatment experiment, the size of the tumor was about 50 to 100 mm³ and it was performed on the 9 days after injection.

3.2.14 In vivo fluorescence imaging with Eu/VBBO lipo and therapeutic antibodies

Alexa Fluor™ 647-Tz and Alexa Fluor™ 647-Ctx were separately injected intravenously into the SKOV-3 and CT-26 tumor bearing BALB/c nude mice. In vivo fluorescence imaging was conducted by IVIS at different time points (0, 2, 24, 48 hours). After the 48-hour time point imaging, major organs including tumor tissue were collected and performed ex vivo imaging. The DiD labeled Eu/VBBO lipo was injected intravenously both SKOV-3 and CT-26 tumor bearing mouse models and conducted in vivo and ex vivo imaging in the same as the imaging of Tz and Ctx.

3.2.15 In vivo PET imaging of ^{64}Cu labeled Eu/VBBO lipo and Ctx

^{64}Cu labeled Eu/VBBO lipo and ^{64}Cu labeled Ctx were injected respectively into the BALB/c nude CT-26 tumor bearing mice. The in vivo PET imaging was performed at various time points (0, 2, 18, 48 hours) by the PET scanner. After the imaging, quantitative analysis was conducted by MIM software based on the PET scanned images.

3.2.16 In vivo SPECT/CT imaging of ^{177}Lu labeled Ctx

^{177}Lu labeled Ctx was injected intravenously into the BALB/c nude CT-26 tumor bearing mice. Control group for the Ctx specific targeting imaging was injected intravenously bare Ctx 24 hours before the in vivo SPECT/CT imaging. The in vivo SPECT/CT imaging was performed in the order of SPECT followed by CT at various time points (0, 24, 48 hours). The quantitative analysis was conducted by MIM software based on the SPECT scanned images

3.2.17 In vivo PDT study

CT-26 cancer cells were injected subcutaneously into the right thigh of BALB/c nude mice 9 days before the in vivo PDT. Different kinds of samples (Normal saline, Eu/VBBO lipo, ^{177}Lu -Ctx (120 μCi), ^{177}Lu -Ctx (400 μCi), ^{177}Lu -Ctx (120 μCi) + Eu/VBBO lipo) were treated intravenously for the in vivo PDT study. In case of ^{177}Lu -Ctx (120 μCi) and Eu/VBBO lipo sequential injection, ^{177}Lu -Ctx was first injected 24 hours before the Eu/VBBO lipo injection. Follow-up was conducted up to 18 days by measuring the tumor size and weights of the mice. The size of the tumor was calculated by measuring the long axis and the short axis.

3.3 Results and discussion

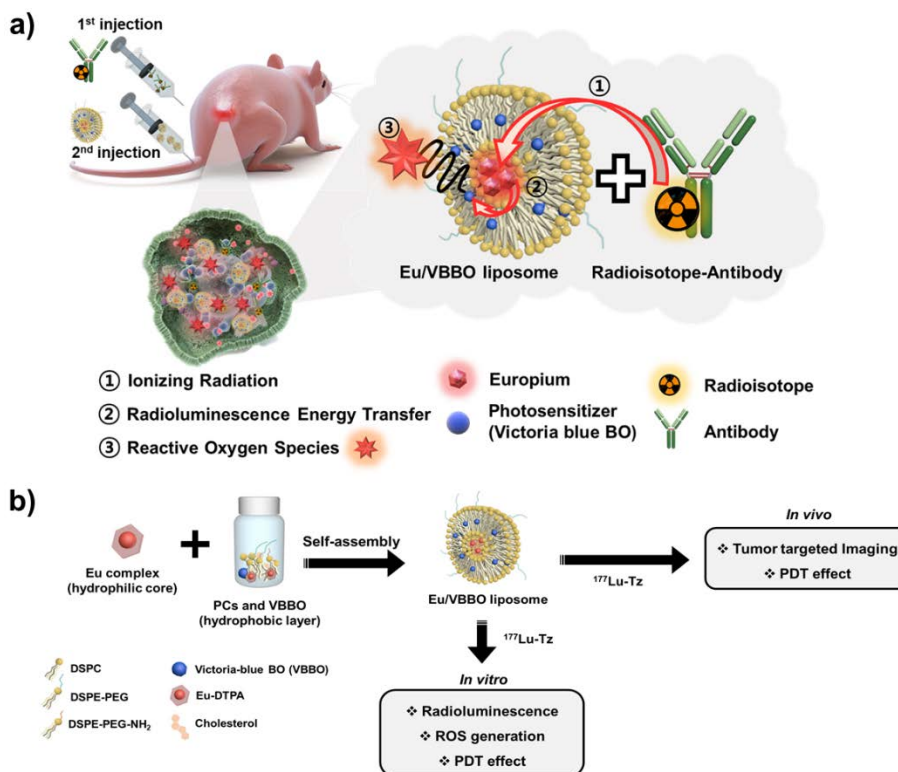


Figure 3.3 Schematic diagram. a) Concept of study and b) experimental scheme of the experimental illustration of combinatory photodynamic therapy.

3.3.1 Experimental scheme

The radioluminescence induced PDT nano-platform was divided previous radio labeled Eu/VBBO lipo into radioisotope labeled antibody as a donor for PDT trigger and Eu-DTPA and VBBO co-loaded liposome as a scintillator and acceptor for PDT activation by the ROS generation (**Figure 3.3 a**). For the liposome, VBBO was intercalated into the lipid thin film and Eu³⁺ was chelated to DTPA in an aqueous solution for the hydration step. The hydrated precursor was tip-sonicated for homogenous mono layered liposome structure and purified with buffered solution

for further in vitro and in vivo studies. Therapeutic antibodies, trastuzumab (Tz) and cetuximab (Ctx), were modified with chelators or fluorescent molecules such as NOTA and DOTA for the radioisotope (^{64}Cu , ^{177}Lu) labeling or Alexa FluorTM 647 and FITC for in vitro and in vivo active targeting fluorescence imaging. Fluorescent Tz and Ctx were validated their specific targeting abilities to target receptor expressed cancer cells by the confocal fluorescence imaging and flow cytometry. RL and RL energy transfer imaging was conducted by the combinatory therapy system of ^{177}Lu -Tz and Eu/VBBO lipo to optimize and determine the concentration of Eu and VBBO. In vitro ROS production and in vitro PDT studies were performed with SKOV-3, HER2+ and Tz specific targeted cancer cell line, based on RL imaging to confirm in vitro therapeutic effect of the combinatory therapy system. For the in vivo studies, in vivo fluorescence imaging and nuclear medicine imaging were conducted to xenograft mouse tumor models by IVIS, PET, or SPECT/CT with fluorescence dye modified or radiolabeled therapeutic antibodies and Eu/VBBO lipo. In vivo PDT was performed to a CT-26 xenograft mouse tumor model by conducting follow-up up to 18 days after the post injection of the ^{177}Lu -Ctx and Eu/VBBO lipo. **(Figure 3.3 b)**

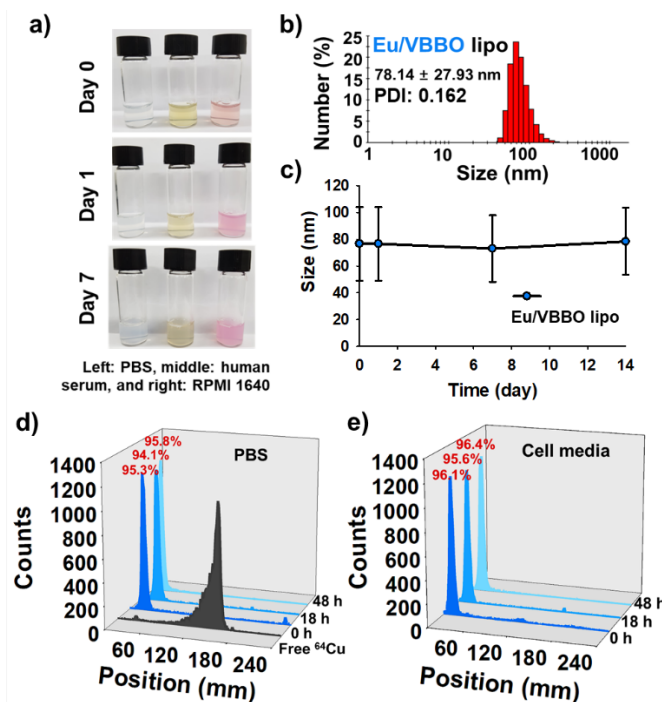


Figure 3.4 Hydrodynamic size measurement, stability, and radiostability tests of Eu/VBBO lipo . a) Photographic image of stability test with Eu/VBBO lipo under the physiological conditions (PBS, human serum, and RPMI 1640) at various time points (0, 1, 7 days). b) DLS measurement of Eu/VBBO lipo (n=3). c) Numeric graph of stability test in PBS up to 14 days. ^{64}Cu labeling efficiency and stability up to 48 h in d) PBS and e) cell media.

3.3.2 Hydrodynamic size measurement, stability, and radiostability tests of Eu/VBBO lipo and radiolabeling efficiency and radiostability of Ctx

The Eu/VBBO lipo was evaluated its structure, morphology, and size in the previous study. Uniformity and stability of the Eu/VBBO lipo were mainly confirmed by measuring the size by DLS in this study. The hydrodynamic size of Eu/VBBO lipo was 78.14 ± 27.93 nm, and polydispersity index (PDI) value was 0.162 according to the triplicate measurement (**Figure 3.4 b**). It was clearly observed that

low PDI value indicates that it was uniformly present in the aqueous solution with a size of about 80 nm. The stability test was demonstrated by acquiring photographic images up to 7 days under the physiological conditions such as PBS, human serum, and cell media (RPMI 1640) in **Figure 3.4 a** followed by measuring the hydrodynamic size up to 14 days in 1X PBS (**Figure 3.4 c**). There were no observable precipitates during the stability test in 3 different kinds of environment. It was also confirmed that the hydrodynamic size through DLS remained almost unchanged until the 14th day which means that it can be kept stable for the further in vitro and in vivo experiments especially in the stable circulation in the blood pool in vivo.

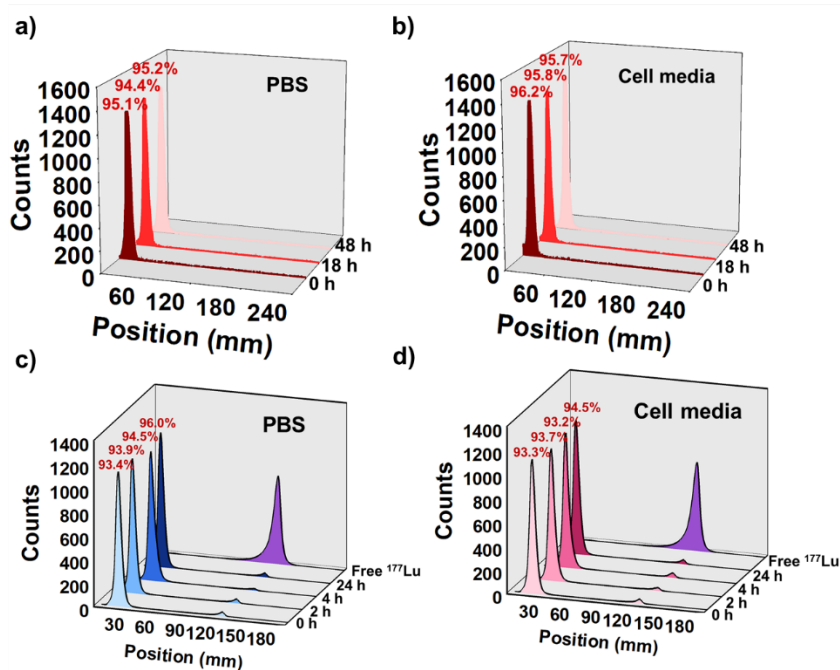


Figure 3.5 Radiolabeling efficiency and radiostability of Ctx. ^{64}Cu labeling efficiency and stability up to 48 h in a) PBS (n=3) and b) cell media (n=3). ^{177}Lu labeling efficiency and stability up to 24 h in a) PBS (n=3) and b) cell media (n=3).

For in vivo nuclear medicine imaging and in vitro and in vivo studies, Eu/VBBO lipo and Ctx were radiolabeled with ^{64}Cu or ^{177}Lu . Eu/VBBO lipo and Ctx were radiolabeled with ^{64}Cu for in vivo PET imaging. ^{64}Cu labeled Eu/VBBO lipo (^{64}Cu -Eu/VBBO lipo) and ^{64}Cu -Ctx maintained high radiolabeling efficiency in PBS (^{64}Cu -Eu/VBBO lipo: 98.8% / ^{64}Cu -Ctx: 95.2%) (**Figure 3.4 d, Figure 3.5 a**) and cell media (^{64}Cu -Eu/VBBO lipo: 96.4% / ^{64}Cu -Ctx: 95.7%) (**Figure 3.4 e, Figure 3.5 b**) for up to 48 hours. For in vitro and in vivo studies, Tz and Ctx were labeled with ^{177}Lu , a therapeutic radioisotope. ^{177}Lu -Tz showed radiolabeling efficiencies of 93.4% and 93.3%, respectively, in physiological conditions such as PBS and cell media, and showed significantly high radiolabeling stability of more than 90% up to 24 hours (**Figure 3.5 c-d**). These results indicated that the antibody-labeled ^{177}Lu guarantees high labeling stability for in vivo imaging and PDT studies.

3.3.3 In vitro specific targeting efficiencies of therapeutic antibodies

The FITC modified Tz and Alexa Fluor™ 647 modified Ctx were validated their active targeting abilities by conducting confocal fluorescence imaging and flow cytometry with antibody specific targeted cancer cell lines. SKOV-3 and 4T1 were selected for Tz specific cancer cell lines which were represented HER2 protein overexpressed (HER2+) cancer cell and cancer cells with low levels of HER2 protein expression (HER2-) respectively. CT26, an EGFR overexpressed cancer cell, was also selected as a Ctx antibody-specific cancer cell. In the case of IgG, it was used as a control group for the active targeting ability of Ctx. FITC-Tz was treated with SKOV-3 and 4T1 cancer cell lines corresponding to HER2+ and HER2- cell lines, respectively, and then confocal fluorescence imaging was performed. As shown in the green fluorescence filter ($\lambda_{\text{ex}} / \lambda_{\text{em}}$: 485 / 520 nm) image corresponding to Tz, it

was confirmed that the fluorescence signal was emitted only from SKOV-3 in which HER2 was overexpressed. In 4T1 cancer cells, almost no green fluorescence signal of Tz was observed. it was clearly confirmed that Tz was specifically bound only to SKOV-3, in which the HER2 protein was overexpressed (**Figure 3.6 a**). Even when flow cytometry was performed to confirm the specific binding ability of Tz to the HER2 protein, in the SKOV-3 group, only the cell and the secondary antibody with Alexa Fluor™ 647 without Tz as the primary antibody were added and reacted. It could not be confirmed that the SKOV-3 was bound to the cell surface. On the other hand, the group that responded to the secondary antibody to which Alexa Fluor™ 647 was bound after the reaction with the primary antibody Tz bound to the surface of SKOV-3 cancer cells significantly differently from other controls. In the case of HER2-, 4T1 breast cancer cells, the results of binding to the 4T1 cell surface could not be confirmed in all groups (**Figure 3.3 b-c**).

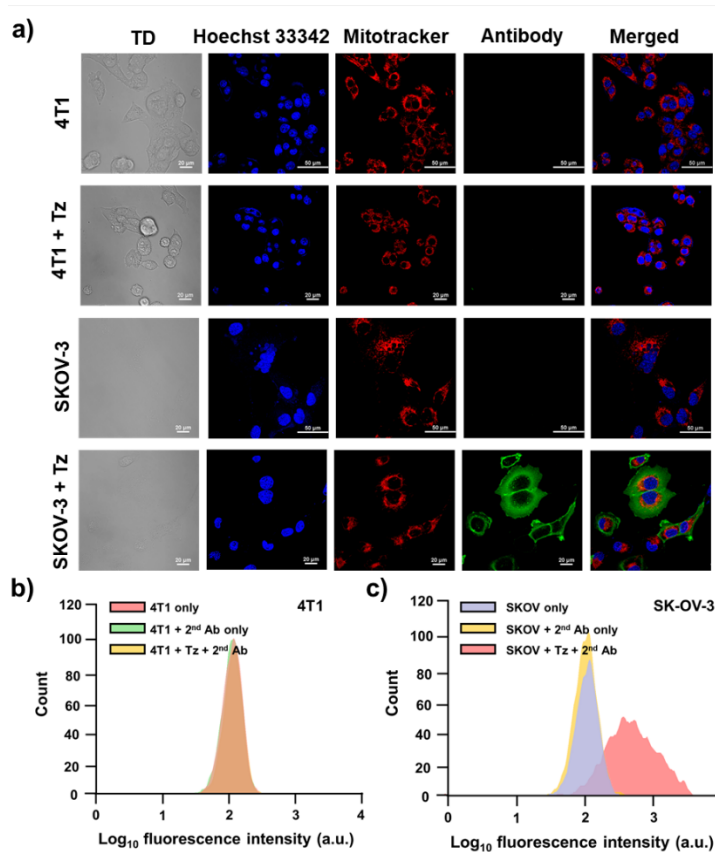


Figure 3.6 In vitro specific targeting efficiencies of Tz. a) Confocal microscope imaging with Tz in 4T1 and SKOV-3 cancer cell lines (Hoechst 33342: nucleus, Mitotracker: mitochondria, and Antibody: FITC-Tz). Flow cytometry analysis of Tz in b) 4T1 and c) SKOV-3.

In the case of Ctx, after labeling with Alexa Fluor™ 647 fluorescent molecule, the CT-26 colorectal cancer cell line overexpressing the EGFR protein was treated for confocal imaging. IgG labeled with Alexa Fluor™ 647 was used as a control for Alexa Fluor™ 647-Ctx. In the deep red fluorescence filter ($\lambda_{\text{ex}} / \lambda_{\text{em}}$: 600 / 650 nm) corresponding to each antibody, specific targeting ability was confirmed only in Ctx. Meanwhile, in the case of IgG, it was confirmed that almost no fluorescence signal was displayed in the same fluorescence filter (**Figure 3.7 a**).

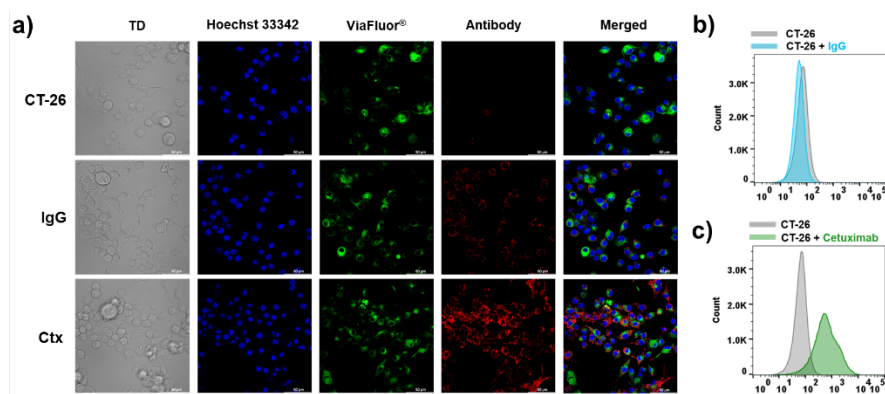


Figure 3.7 In vitro specific targeting efficiencies of Ctx. a) Confocal microscope imaging with Ctx and IgG in CT-26 cancer cell lines (Hoechst 33342: nucleus, ViaFluor®: cytoplasm, and Antibody: Alexa Fluor™ 647-Ctx). Flow cytometry analysis of b) Ctx and c) IgG in CT-26.

As a result of flow cytometry analysis of the two antibodies labeled with the same fluorescence, only Ctx specifically bound to the EGFR protein on the surface of CT-26 in the same manner as for fluorescence imaging. This means that only Ctx showed specific binding ability with EGFR on the surface of CT-26, an EGFR protein overexpressed cancer cell (**Figure 3.7 b-c**). Based on the above active targeting activity confirmation, the corresponding target antibodies have excellent active targeting ability for proteins that are specifically overexpressed on the surface of cancer cells. It could be referred that it was effective as a vehicle that had an ability to deliver elements to cancer tissues by active targeting.

3.3.4 Radioluminescence (RL) and radioluminescence energy transfer (RET) imaging of combinatorial therapeutic system

The radioisotope carrier antibody was labeled with ^{177}Lu , a therapeutic radioisotope to perform subsequent in vitro and in vivo studies with the combinatorial photodynamic therapy system. After ^{177}Lu radiolabeling on the Tz surface, which is a therapeutic antibody, the following groups were designed for RL imaging in a combination treatment system with a radiolabeled antibody and Eu/VBBO lipo, and RL imaging was performed with IVIS; DI water, Eu lipo, Eu/VBBO lipo, free ^{177}Lu -Tz (100 μCi), ^{177}Lu -Tz (100 μCi) + Eu lipo, and ^{177}Lu -Tz (100 μCi) + Eu/VBBO lipo (**Figure 3.8 a**). As in RL imaging, the RL by ^{177}Lu -Eu lipo generated a significantly higher luminescence signal than CL by free ^{177}Lu . Since luminescence by ^{177}Lu -Eu lipo is a signal including RL and CL, the value obtained by subtracting CL by free ^{177}Lu from luminescence intensity of ^{177}Lu -Eu lipo becomes the intensity of RL, which is 9 times higher than CL by ^{177}Lu (**Figure 3.8 b**). It was confirmed through an imaging-based luminescence intensity numerical graph (6.16×10^6 p/s vs. 6.65×10^5 p/s, $P < 0.001$). The RL intensity of ^{177}Lu -Tz + Eu/VBBO lipo was lower than that of ^{177}Lu -Tz + Eu lipo because the RL intensity was reduced due to the energy transfer to the VBBO.

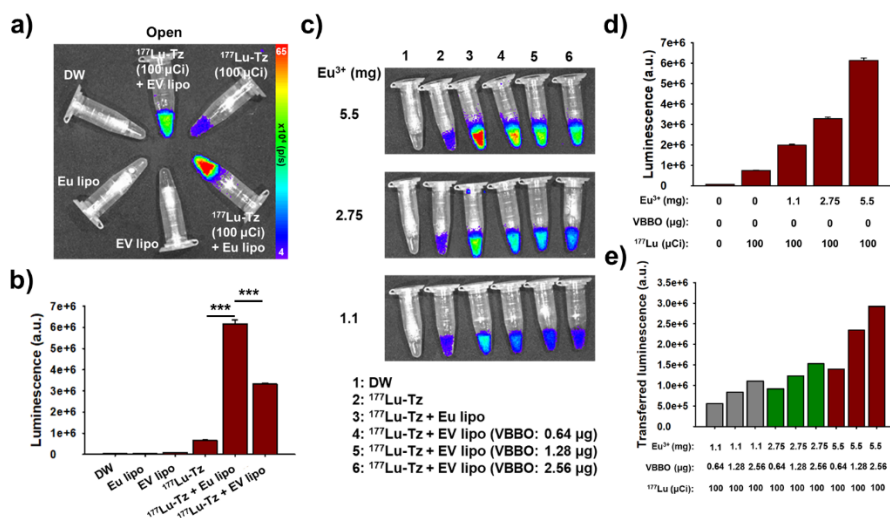


Figure 3.8 Radioluminescence (RL) and radioluminescence energy transfer (RET) imaging of combinatorial therapeutic system. a) RL imaging by IVIS in different types of liposomes or ¹⁷⁷Lu labeled Tz. b) Numerical analysis and comparison based on the RL imaging (n=3, *P < 0.05, **P < 0.01, ***P < 0.001). c) RL and RET imaging of combinatorial PDT system according to the concentration of Eu³⁺ and VBBO. d) Numeric graph of RL intensity increase with Eu³⁺ concentration gradient in the presence of ¹⁷⁷Lu (100 μCi) (n=3). e) RET efficiency comparison by calculating the transferred luminescence according to the amounts of Eu³⁺ and VBBO. Statistical analysis was conducted by t test.

The RL energy transfer (RET) according to the amount of Eu and VBBO was demonstrated to quantify the RET efficiency: Eu³⁺: 0, 1.1, 2.75, and 5.5 mg / VBBO: 0, 0.64, 1.28, and 2.56 μg (**Figure 3.8 c**). In the case of ¹⁷⁷Lu-Tz + Eu lipo indicating RL without VBBO, when the luminescence intensity was quantified based on RL imaging, the total luminescence intensity increased in proportion as the amount of Eu³⁺ increased (**Figure 3.8 d**). The ¹⁷⁷Lu dose maintained at 100 μCi to confirm the RL imaging and RET according to the amount of Eu and VBBO. As a result of

quantifying the luminescence intensity according to the amount of the two materials, the amounts of Eu^{3+} and VBBO showed the highest RET efficiency of 47.6% at 5.5 mg and 2.56 μg , respectively (**Figure 3.8 e**). Although a radioisotope was separated from the previously developed liposome platform and divided into two combinatorial systems, RL from Eu^{3+} was properly released by being induced by ^{177}Lu -Tz. Comparing that the RET efficiency (47.6%) in the combination treatment system of ^{177}Lu -Tz and Eu/VBBO lipo is 13.4% lower than that of the ^{64}Cu -labeled Eu/VBBO lipo in the previous study (RET efficiency = 61.0%). Although the RET efficiency was lower when ^{177}Lu was radiolabeled to the antibody instead of radiolabeling with ^{64}Cu , the half-life of ^{177}Lu (6.65 days) is 12.6 times longer than that of ^{64}Cu (12.7 hours), and the degree of ROS generation can last longer than that of ^{64}Cu , which could be expected to be more effective in the PDT effect. Furthermore, ^{177}Lu is well known as a therapeutic radioisotope⁹³⁻⁹⁶. β - rays from ^{177}Lu used for radiation therapy account for most of the emitted radiation at about 78%, whereas ^{64}Cu also emits β - rays, but the ratio is about 38%, so β - rays emission from ^{177}Lu is about 2.05-fold higher.

3.3.5 In vitro ROS production imaging and effective in vitro PDT effect of combinatory therapeutic system

ROS production imaging was conducted to observe ROS generation of VBBO by RET via a combinatorial PDT system (**Figure 3.9 a**). The low dose and high dose of ^{177}Lu were set to 10 and 100 μCi , respectively, and the experimental group was designed as follows: SKOV-3, Eu/VBBO lipo, ^{177}Lu -Tz (10 μCi), ^{177}Lu -Tz (100 μCi), ^{177}Lu -Tz (10 μCi) + Eu/VBBO lipo. As shown in the imaging, it was found that the ROS was significantly higher at the high dose of ^{177}Lu (100 μCi) than at the low dose of ^{177}Lu (10 μCi). In other words, the higher the dose of the therapeutic radioisotope, the more ROS was produced by specific binding to the cancer cell surface by Tz. In contrast, in the low-dose ^{177}Lu -Tz (10 μCi) and Eu/VBBO lipo combination system, it was confirmed that a clear signal was obtained from the green fluorescence filter corresponding to the ROS signal as shown in fluorescence imaging. Compared with the high dose of ^{177}Lu -Tz (100 μCi), it showed almost the same degree of ROS generation.

For cytotoxic effect demonstration, Eu/VBBO lipo and Tz were co-treated into the SKOV-3 cancer cell line (**Figure 3.9 b**). Eu^{3+} was maintained based on the dose (0.8 mg) of the previous study, and the used antibody, Tz, was maintained at 80 μg (clinical dose: 4 mg/kg). In the case of VBBO, which is PS, the amount of VBBO was gradually increased due to its own toxicity. As the amount of VBBO increased, the cell viability of SKOV-3 did not change significantly, and even in the VBBO concentration range of 0.16 μg , the maximum treatment concentration of Eu/VBBO lipo, the cell viability maintained at the level of viability of normal cells. In addition, there was no clear degree of cytotoxicity with respect to the fixed amounts of Eu^{3+} and Tz. Based on this result, the amount of VBBO was set to 0.16 μg , and further

PDT studies were conducted at this concentration.

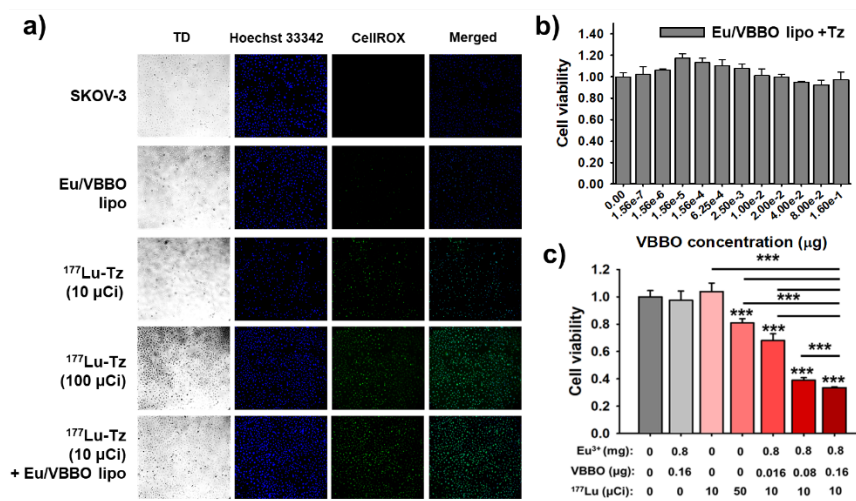


Figure 3.9 In vitro ROS production imaging and effective in vitro PDT effect of combinatory therapeutic system. a) Optical fluorescence microscope imaging of ROS generation level (Hoechst 33342: nucleus, CellROX: ROS detecting molecule). b) Cytotoxicity effect of Eu/VBBO lipo and Tz in SKOV-3 cancer cell line (n=3). c) In vitro PDT effect demonstration of combinatorial PDT system (n=3, *P < 0.05, **P < 0.01, ***P < 0.001). Statistical analysis was conducted by ANOVA test.

Based on the cytotoxicity test, the in vitro PDT effect of the combination PDT system was confirmed under the conditions shown in Table 1 (**Figure 3.9 c**). After treating nanoparticles for each treatment group and incubating for 24 hours, the degree of cancer cell removal was compared based on cell viability through MTT assay. Among the group treated only with ¹⁷⁷Lu-Tz, the group treated with ¹⁷⁷Lu at a low dose, that is, 10 µCi, showed viability almost the same as the cell viability of the control SKOV-3 cancer cell line untreated (cell viability: 1.04). The ¹⁷⁷Lu-Tz group

(50 μCi) treated with a high dose of ^{177}Lu had a cell viability of 0.81, which was about 19% of the cancer cell removal ability. Meanwhile, the low-dose ^{177}Lu -Tz (10 μCi) + Eu/VBBO lipo group showed the lowest level compared to other groups with about 67% of cell killing effect. In addition, as the amount of VBBO gradually increased from 0.016 μg to 0.16 μg , the cancer cell removal ability also increased in proportion to the concentration of VBBO. This means that the RL released by Eu^{3+} is transferred to VBBO, and the higher the concentration of VBBO that can absorb it, the higher the ROS generation and the PDT effect through it. Comparison of the PDT effect (19% vs. 67%, *** $P < 0.001$) of ^{177}Lu -Tz (50 μCi) and ^{177}Lu -Tz (10 μCi) + Eu/VBBO lipo in SKOV-3 cancer cell line. It was confirmed that the PDT effect of the system ^{177}Lu -Tz (10 μCi) + Eu/VBBO lipo was 3.5 times better than that of ^{177}Lu -Tz (50 μCi). Based on these results, it meant that a more enhanced photodynamic treatment effect could be achieved than in the low-dose combination treatment system.

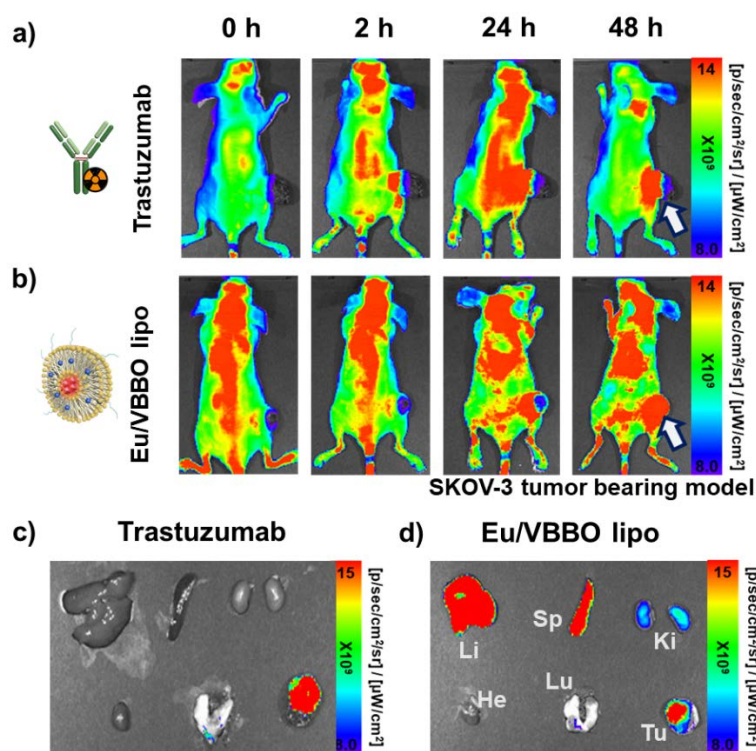


Figure 3.10 In vivo fluorescence imaging of Eu/VBBO lipo and Tz. In vivo fluorescence images of a) Tz and b) Eu/VBBO lipo in SKOV-3 tumor bearing mouse model at various time points (0, 2, 24, and 48 h) (n=3). Ex vivo fluorescence images of major organs with c) Tz and d) Eu/VBBO lipo at 48 h post injection in SKOV-3 tumor bearing mouse model.

3.3.6 In vivo fluorescence and in vivo nuclear medicine imaging of Eu/VBBO lipo and therapeutic antibodies

For in vivo fluorescence imaging of Eu/VBBO lipo, Tz, and Ctx, each nanomaterial was labeled with Alexa Fluor™ 647 fluorescent dye. As a mouse cancer model, SKOV-3 and CT-26 cancer cell lines specific for Tz and Ctx, respectively, were injected subcutaneously into the right thigh to prepare a cancer model. When the tumor of each mouse cancer model was 3 weeks after subcutaneous injection, Eu/VBBO lipo, Tz, and Ctx were injected into the tail vein to perform fluorescence imaging at various time points (0, 2, 24, 48 hours). Based on the in vivo fluorescence images, Tz and Ctx which specifically bound to each cancer tissue were ingested into the tumor 2 hours after injection. There was a significant tumor uptake over time after antibody injection in each mouse cancer model based on in vivo imaging, and when the uptake level of each antibody into major organs was observed ex vivo after 48 hours of fluorescence imaging, both antibodies were specifically ingested only in the tumor, resulting in a significantly high fluorescence signal (**Figure 3.10 a, Figure 3.11 a**). In the case of an antibody, it had an excellent active targeting ability against cancer tissues in which antibody-specific receptor proteins (HER2 for Tz, EGFR for Ctx) were overexpressed in cancer tissues, and was the most suitable nanoprobe as a carrier for delivering radioisotopes to tumor region. In addition, Tz and Ctx were specifically bound through active targeting only in tumors, and both antibodies to other major normal organs (heart, liver, spleen, lung, and kidney) resulted in little uptake (**Figure 3.10 c, Figure 3.11 c**).

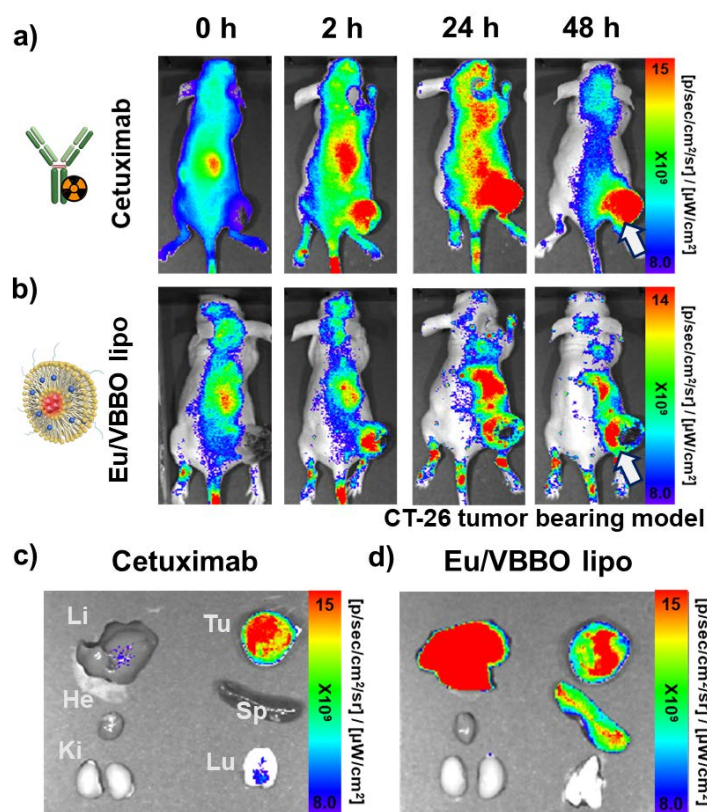


Figure 3.11 In vivo fluorescence imaging of Eu/VBBO lipo and Ctx. In vivo fluorescence images of a) Ctx and b) Eu/VBBO lipo in CT-26 tumor bearing mouse model at various time points (0, 2, 24, and 48 h) (n=3). Ex vivo fluorescence images of major organs with c) Ctx and d) Eu/VBBO lipo at 48 h post injection in CT-26 tumor bearing mouse model.

Therefore, it was expected that the problem of organ damage caused by normal organ accumulation of radioisotope-labeled antibody could be overcome. Eu/VBBO lipo also increased significantly in tumor uptake in both cancer models over time through in vivo fluorescence imaging, similar to the antibody (Figure 3.10 b, Figure 3.11 b). When the uptake into major organs and tumors through ex vivo was conducted after 48 hours of imaging, a high uptake was observed in the liver and

spleen as well as a substantial uptake in the tumor (**Figure 3.10 d**, **Figure 3.11 d**). This phenomenon is the biodistribution mainly seen in nanomaterials. For nanomaterials injected from the outside, the reticuloendothelial system (RES) removes these materials from the phagocytic cells in the circulatory system, and the liver and spleen are mainly included in this system.

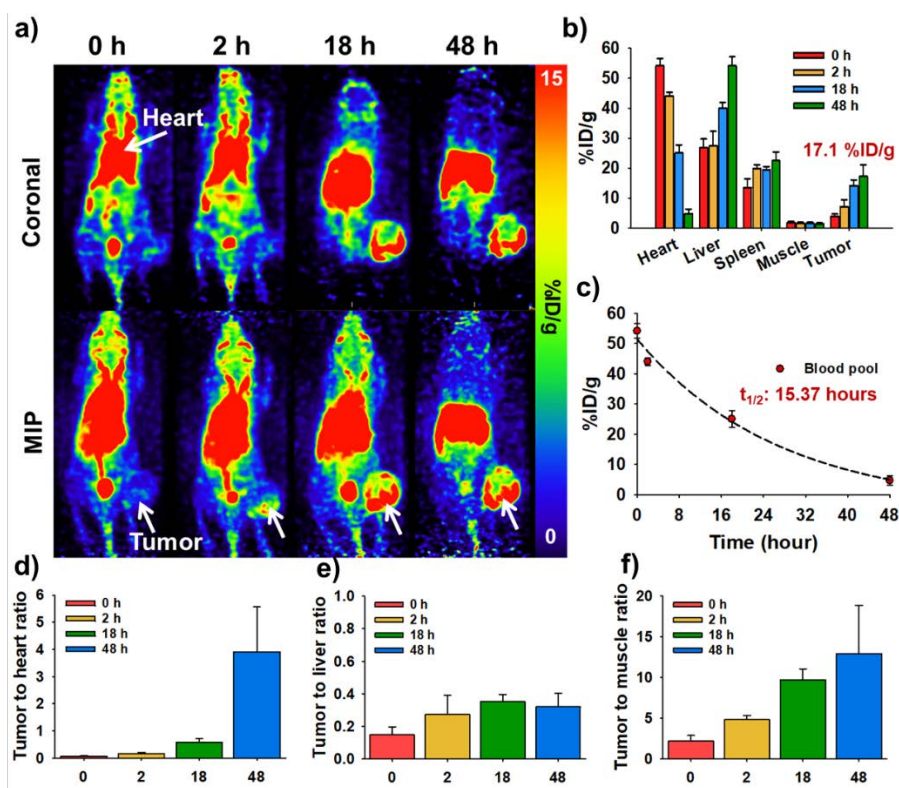


Figure 3.12 In vivo PET imaging and quantitative analysis of $^{64}\text{Cu-Eu/VBBO}$ lipo. a) In vivo PET scanned coronal and MIP images at different time series (0, 2, 18, and 48 h) (n=3). White arrows are indicated tumor sites. b) Biodistribution quantitative analysis of $^{64}\text{Cu-Eu/VBBO}$ lipo in major organs and tumor over time (n=3, mean \pm s.d.). c) Circulation half-life in blood pool of $^{64}\text{Cu-Eu/VBBO}$ lipo (n=3, mean \pm s.d.). Tumor to organ ratio at various time points (d) tumor to heart,

e) tumor to liver, and f) tumor to muscle) (n=3, mean \pm s.d.).

In vivo PET imaging was performed to observe the passive and active targeting efficiencies of ^{64}Cu labeled Eu/VBBO lipo (^{64}Cu -Eu/VBBO lipo) (**Figure 3.12 a**) and ^{64}Cu labeled Ctx (^{64}Cu -Ctx) (**Figure 3.13 a**) in CT-26 xenograft tumor bearing mice model. The blood pool showed a long circulation and a significant uptake in the tumor over time was confirmed through in vivo PET scanned images of ^{64}Cu -Eu/VBBO lipo and ^{64}Cu -Ctx. According to the quantitative analysis of tumors and major organs based on PET scanned images, the uptake of Eu/VBBO lipo and Ctx into tumors gradually increased to 17.1 %ID/g (**Figure 3.12 b**) and 25.1 %ID/g (**Figure 3.13 b**), respectively, up to 48 hours after intravenous injection. When fitting from the blood pool based on the quantitative analysis values in the heart, the circulating half-life of Eu/VBBO lipo was 15.37 hours (**Figure 3.12 c**) and the circulating half-life of Ctx was 4.05 hours up to the first 2 hours and 160.38 hours up to 48 hours (**Figure 3.13 c**). The ratios for tumor and major normal organs (heart, liver, and muscle) also increased gradually over time. At 48 hours after injection, the ratios of Eu/VBBO lipo were 3.92, 0.32, and 12.93 folds, respectively (**Figure 3.12 d-f**). For Ctx, the ratios were 0.88, 0.87, and 8.86 folds, respectively (**Figure 3.13 d-f**).

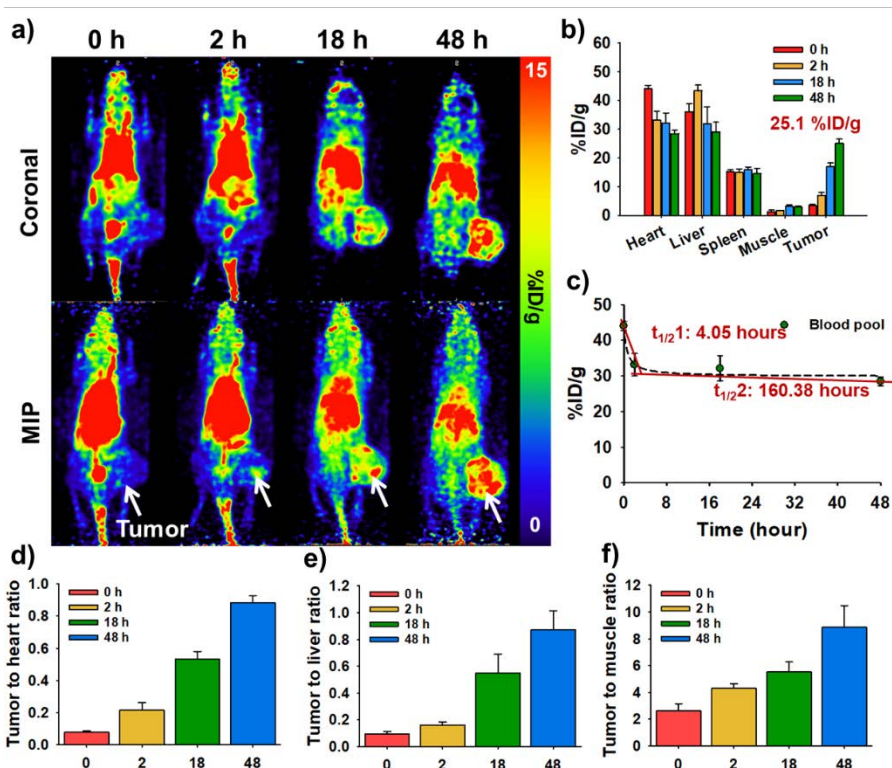


Figure 3.13 In vivo PET imaging and quantitative analysis of ^{64}Cu -Ctx. a) In vivo PET scanned coronal and MIP images at different time series (0, 2, 18, and 48 h) (n=3). White arrows are indicated tumor sites. b) Biodistribution quantitative analysis of ^{64}Cu -Ctx in major organs and tumor over time (n=3, mean \pm s.d.). c) Circulation half-life in blood pool of ^{64}Cu -Ctx (n=3, mean \pm s.d.). Tumor to organ ratio at various time points (d) tumor to heart, e) tumor to liver, and f) tumor to muscle) (n=3, mean \pm s.d.).

In vivo SPECT/CT imaging was further studied to verify the tumor-specific active targeting ability of ^{177}Lu -Ctx in CT-26 tumor bearing mice model, which is essential for in vivo PDT. To confirm the active targeting ability of ^{177}Lu -Ctx to CT-26 tumors, free Ctx as a blocking control was pre-injected intravenously 24 hours before the

SPECT/CT imaging (**Figure 3.14 b**). The tumor targeting ability of ^{177}Lu -Ctx was significantly higher as time passed up to 48 hours after injection (**Figure 3.14 a**). Although the control group also showed tumor uptake over time, it was compared to be much lower than tumor targeting of ^{177}Lu -Ctx alone. ^{177}Lu -Ctx had also substantially long blood pool circulation according to the acquired images.

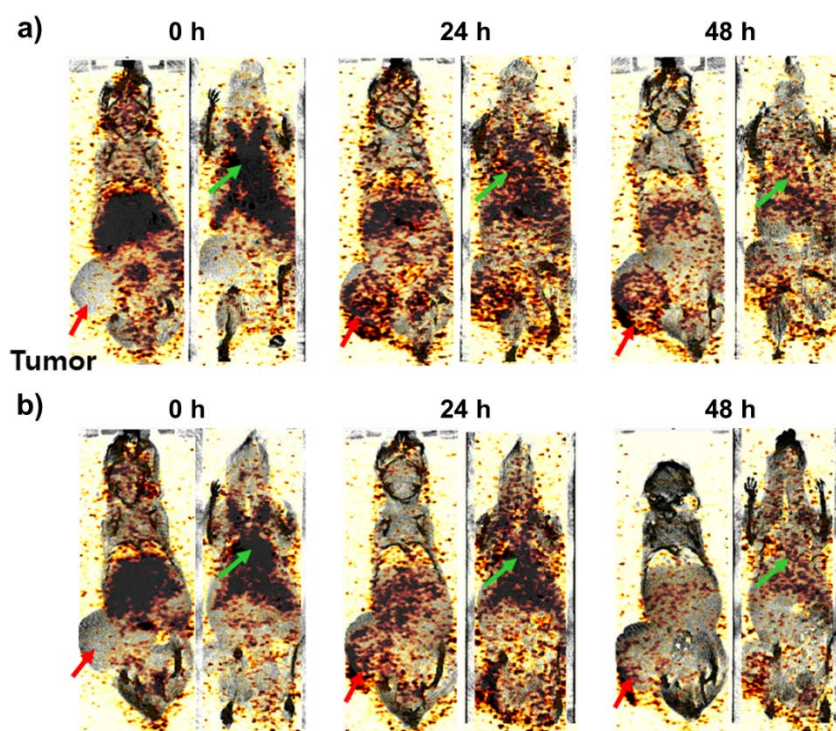


Figure 3.14 In vivo SPECT/CT imaging and quantitative analysis of ^{177}Lu -Ctx.

In vivo SPECT/CT scanned coronal images of a) ^{177}Lu -Ctx and b) ^{177}Lu -Ctx with blocking (pre-injection of free Ctx) at different time series (0, 24, and 48 h) (n=3). Red and green arrows are indicated tumor and heart, respectively.

Based on these in vivo fluorescence and nuclear medicine imaging, this was the most suitable nanoprobe for tumor delivery as the liposome structure that can

simultaneously contain Eu^{3+} and VBBO, two substances essential in a short distance for ROS generation, showed high passive targeting ability in vivo. Eu/VBBO lipo showed high accumulation in the liver and spleen which are indicated normal organs. However, despite the high uptake in the normal organs, it was assumed that there was little damage to normal tissues because ROS generation by Eu/VBBO lipo was difficult due to the absence of radioisotopes. In the case of Ctx, it showed a much higher active targeting ability against tumors than liposomes, and the uptake into tumors increased over time in fluorescence and SPECT/CT scanned images by radiolabeling with ^{177}Lu , and uptake into normal organs was relatively low. According to these in vivo imaging, our combinatorial PDT system reduced the possibility of damage to normal tissues because ROS generation by Eu/VBBO lipo was difficult because radioisotopes were separated from existing liposomes into antibodies. Furthermore, it was expected that the high targeting ability of the two nanoprobe to the tumor would show a high therapeutic effect at the tumor site.

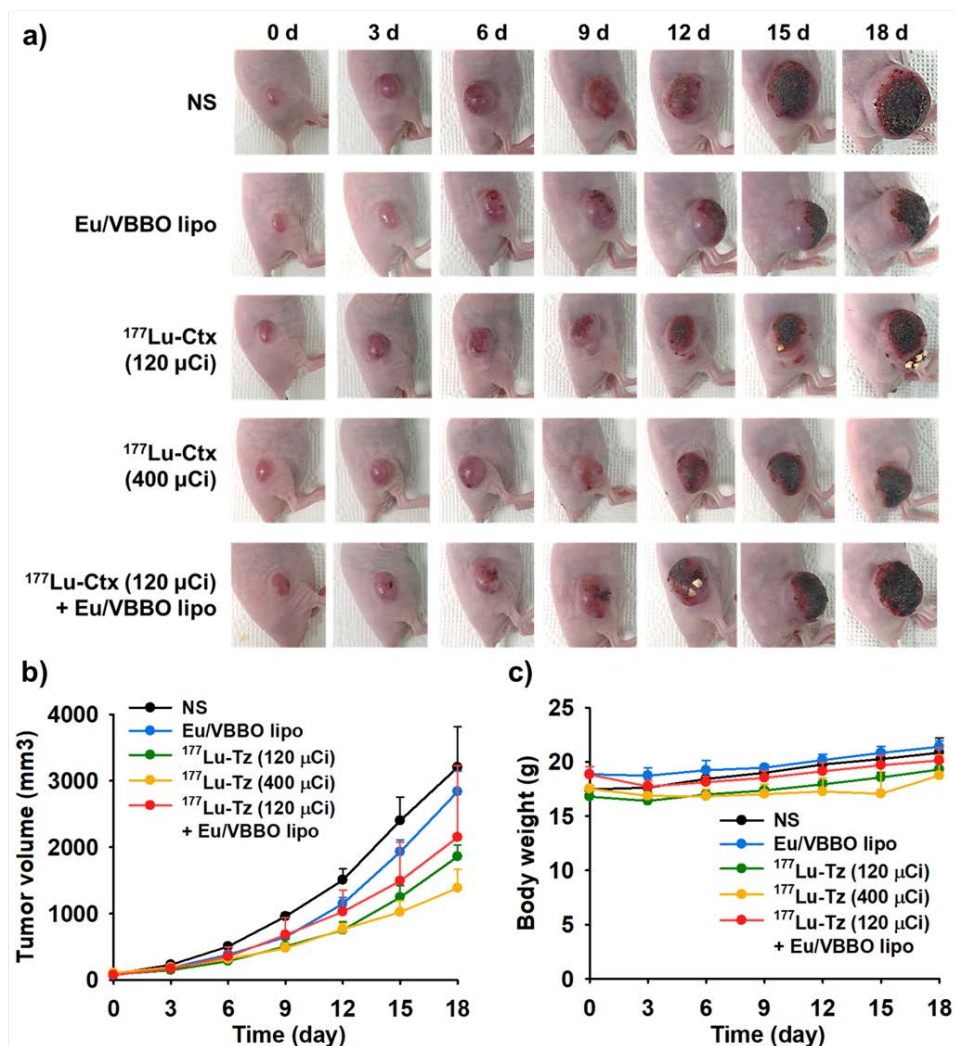


Figure 3.15 In vivo PDT of combinatorial PDT system. a) Tumor follow-up images in CT-26 tumor bearing mouse model after intravenous injection of NS, Eu/VBBO lipo, ^{177}Lu -Ctx (120 μCi), ^{177}Lu -Ctx (400 μCi), and ^{177}Lu -Ctx (120 μCi) + Eu/VBBO lipo (n=3 for each group). b) Tumor volume profiles up to 18 days (n=3, mean \pm s.d.). c) Body weight changes follow-up for 18 days (n=3, mean \pm s.d.).

3.3.7 In vivo PDT of combinatorial therapeutic system

In vivo PDT was performed with the combinatory photodynamic therapy system composing Eu/VBBO lipo and ^{177}Lu -Ctx in CT-26 xenograft mouse model which was specific to the Ctx. The in vivo PDT was performed in the following groups: NS, Eu/VBBO lipo, ^{177}Lu -Ctx (120 μCi), ^{177}Lu -Ctx (400 μCi), and ^{177}Lu -Ctx (120 μCi) + Eu/VBBO lipo. The combinatorial PDT system, ^{177}Lu -Ctx (120 μCi) + Eu/VBBO lipo, was first injected with ^{177}Lu -Ctx at an interval of 24 hours, considering that the circulating and tumor targeting efficacies of Ctx is higher than those of liposomes based on in vivo imaging demonstrations. In vivo PDT was performed by injecting Eu/VBBO lipo intravenously post ^{177}Lu -Ctx injection. As for the low dose of ^{177}Lu , ^{177}Lu -Ctx (120 μCi), the tumor size gradually increased over time, and there was no significant difference in tumor size compared with other control groups such as NS and Eu/VBBO lipo. In the group injected with ^{177}Lu -Ctx (400 μCi) corresponding to a high dose of ^{177}Lu , it was confirmed that the tumor size increased slowly for 18 days compared to the other control groups. When the CT-26 tumor treatment effect according to the dose of ^{177}Lu was compared, the tumor growth inhibitory ability was higher as the dose of ^{177}Lu was higher. Meanwhile, the combination treatment system, ^{177}Lu -Ctx (120 μCi) + Eu/VBBO lipo, continued to increase tumor size as a result of follow-up until day 18, and there was no significant difference in tumor size compared to any other group based on the acquired photographic images and tumor volume numeric graph (**Figure 3.15 a-b**). During the 18-day follow-up, there was no significant change in body weight in any group (**Figure 3.15 c**). Although Eu/VBBO lipo and Ctx showed significant tumor targeting ability reaching 17.1 %ID/g and 25.1 %ID/g, respectively and the in vitro PDT effect based on RLET imaging also had a cancer cell killing effect of 67%,

which is more than twice that of the high dose of ^{177}Lu , the synergistic PDT effect in vivo using combination of ^{177}Lu -Ctx and Eu/VBBO lipo was significantly low.

The following two factors could be attributed to the low therapeutic effect. One reason was that although the active targeting efficiency of Ctx on tumor was 25.1% ID/g in the CT-26 tumor bearing mouse model based on the PET scanned image labeled with ^{64}Cu , it was not sufficient to show a therapeutic effect using the combinatorial PDT system. Another reason was that the target sites of the liposome and the antibody on the tumor were different from each other. Regarding the in vivo PDT effect different from the previous studies, Eu/VBBO lipo and ^{177}Lu -Ctx both had excellent tumor targeting ability, but it could be suggested the possibility that the location of uptake of the two nanoprobe into the tumor might be different. This is because ^{177}Lu -Ctx is an active target to the tumor because Ctx mainly binds to overexpressed EGFR on the surface of CT-26 cancer cells, but in the case of Eu/VBBO lipo, it entered the cancer cell through the high passive targeting ability of the liposome structure and enhanced permeability and retention (EPR) effect around the tumor region. Due to the difference in the target location on the tumor, it could be inferred that the energy transfer effect and the ROS generation process between the two combination PDT systems were not properly performed, resulting in a low therapeutic effect on the tumor. This low in vivo PDT effect could be improved by making the two nanoprobe at the same tumor target location. By conjugating the surface of Eu/VBBO lipo with Ctx for the identification of the target site, the PDT effect could be enhanced by designing an active targeting liposome in the same way as the Ctx.

3.4 Summary

We tried to enhance the therapeutic effect through a combination photodynamic therapy system with Eu^{3+} and VBBO co-loaded liposomal nanoplatform and a therapeutic radioisotope-labeled antibody. In addition, it was attempted to solve the possibility of damage due to accumulation in normal organs, which is a limitation of the radiolabeled liposomal nanoplatform developed in previous studies. In this study, the combinatorial PDT system was verified its strong radioluminescence emission and energy transfer to VBBO by Eu^{3+} , effective ROS generation of VBBO due to radioluminescence, excellent in vitro PDT effect, and high passive and active targeting efficacies of the liposome and the antibody. However, in vivo PDT with the combinatorial PDT system showed a low therapeutic effect on the tumor because of the low targeting efficiency of ^{177}Lu -Ctx or different target positions between Eu/VBBO lipo and Ctx. Therefore, immuno-Eu/VBBO liposome which was the Eu/VBBO lipo immobilized with Ctx on the surface of the liposome for the active targeting to the tumors in the same manner of the Ctx might be a possible way to improve the low therapeutic effect of the combinatorial PDT system.

Chapter 4. Conclusion

This study dealt with the design and development of a new type of nanoplatform incorporating the concept of radioluminescence for radiation-induced photodynamic therapy among cancer therapies. Photodynamic therapy is one of the treatments that are already being applied clinically in various fields ranging from acne, fungus, and cancer treatment. Studies on photodynamic therapy focusing on cancer treatment have been intensely studied in recent years. In particular, studies have been conducted in recent years to overcome the problem of bio-transmittance of light sources, which is the biggest limitation of conventional PDT. Cancer therapy using radiation-induced PDT is an innovative design that overcomes the limitation of the penetration depth of the light source by using radiation as the initiating role of the treatment. As representative research, many PDT studies using X-ray and Cerenkov radiation have been reported. Despite overcoming the limitations of the light source, other limitations of the use of radiation such as additional external X-ray irradiation or relatively weak Cerenkov luminescence intensity were being revealed. Herein, a study was conducted on the development of a nano-platform for strong radioluminescence emission mediated PDT based on radioisotopes for more efficient radiation-induced PDT.

In Chapter 2, the development of a nano-platform using radioluminescence triggered from radioisotope was performed for radiation-induced PDT. The radioluminescent nanoplatform was highlighted that ROS could be generated by the PS in a single nanoparticle structure itself for treatment cancer by grafting Eu^{3+} which was the main material of radioluminescence and energy transfer to PS. In addition, a liposome nanostructure for the radiation induced PDT which was capable

of labeling of radioisotope on the surface of the liposome and co-loading both Eu^{3+} and PS was selected for the effective passive targeting ability to the tumor region. The ^{64}Cu -Eu/VBBO lipo developed in this study showed much stronger radioluminescence emission than Cerenkov luminescence. In addition, we verified that the radiolabeled radioluminescent nanoplatfrom was significantly superior to the Cerenkov-induced PDT effect in LET, ROS generation, and in vitro/in vivo PDT effects. Furthermore, it showed effective passive targeting through the results of in vivo PET imaging. We successfully invented theranostic radiation induced PDT nanoplatfrom for effective cancer therapy strategy based on these results.

In Chapter 3, we tried to demonstrate improved research to increase the therapeutic effect of the developed nano-platform and minimize organ damage. The previously developed nanoplatfrom for radioluminescence mediated PDT showed high accumulation in normal organs according to in vivo PET images. This phenomenon had emerged as a limiting point that could cause damage to normal organs. To minimize damage to normal organs, a combinatorial PDT system in which the developed nanoplatfrom was divided into two nanoprobess was newly designed as follows: 1) a radiolabeled antibody (donor) and 2) a scintillator and acceptor co-loaded liposome. As in previous studies, Eu/VBBO lipo was demonstrated high dispersion stability under the physiological conditions, uniformity, and high passive targeting ability in a mouse tumor model. Antibodies, Tz and Ctx, were verified to have high active targeting efficacy in antibody-specific cancer cell lines and mouse tumor models, respectively. Subsequently, the two combination PDT systems showed high RLET efficiency according to the amount of Eu^{3+} and PS, effective ROS generation, and excellent in vitro PDT effect. However, in vivo PDT effect was insignificant despite verification of the excellent function and effectiveness of the

combinatorial PDT system. This result suggested that the synergistic effect between the two nanomaterials was significantly lowered because the target location of the liposome and the antibody used for the combination treatment was different at the tumor site. In order to increase the effect of such a combination PDT, it is considered that improvement study such as identification of cancer-targeting ability through introduction of an immuno-liposome conjugated with the same antibody as the radiolabeled antibody is necessary to enhance in vivo therapeutic effect. This nanoplatform development study is the first devised method for effective radiation-based cancer treatment, and although there is room for improvement, it can be referred that it is a nanomaterial with high prospects for the future radiation-induced PDT field.

References

1. Dolmans, D. E. J. G. J.; Fukumura, D.; Jain, R. K., Photodynamic therapy for cancer. *Nat. Rev. Cancer* **2003**, *3* (5), 380-387.
2. Castano, A. P.; Mroz, P.; Hamblin, M. R., Photodynamic therapy and anti-tumour immunity. *Nat. Rev. Cancer* **2006**, *6* (7), 535-545.
3. van Straten, D.; Mashayekhi, V.; de Bruijn, H. S.; Oliveira, S.; Robinson, D. J., Oncologic Photodynamic Therapy: Basic Principles, Current Clinical Status and Future Directions. *Cancers* **2017**, *9* (2), 19.
4. Shafirstein, G.; Battoo, A.; Harris, K.; Baumann, H.; Gollnick, S. O.; Lindenmann, J.; Nwogu, C. E., Photodynamic Therapy of Non-Small Cell Lung Cancer. Narrative Review and Future Directions. *Ann. Am. Thorac Soc.* **2016**, *13* (2), 265-275.
5. Li, X.; Lovell, J. F.; Yoon, J.; Chen, X., Clinical development and potential of photothermal and photodynamic therapies for cancer. *Nature Reviews Clinical Oncology* **2020**, *17* (11), 657-674.
6. Dąbrowski, J. M.; Pucelik, B.; Regiel-Futyra, A.; Brindell, M.; Mazuryk, O.; Kyzioł, A.; Stochel, G.; Macyk, W.; Arnaut, L. G., Engineering of relevant photodynamic processes through structural modifications of metallotetrapyrrolic photosensitizers. *Coordination Chemistry Reviews* **2016**, *325*, 67-101.
7. Park, J.; Lee, Y.-K.; Park, I.-K.; Hwang, S. R., Current Limitations and Recent Progress in Nanomedicine for Clinically Available Photodynamic Therapy. *Biomedicines* **2021**, *9* (1), 85.

8. Calixto, G. M. F.; Bernegossi, J.; De Freitas, L. M.; Fontana, C. R.; Chorilli, M., Nanotechnology-based drug delivery systems for photodynamic therapy of cancer: a review. *Molecules* **2016**, *21* (3), 342.
9. Yin, R.; Dai, T.; Avci, P.; Jorge, A. E. S.; de Melo, W. C.; Vecchio, D.; Huang, Y.-Y.; Gupta, A.; Hamblin, M. R., Light based anti-infectives: ultraviolet C irradiation, photodynamic therapy, blue light, and beyond. *Current opinion in pharmacology* **2013**, *13* (5), 731-762.
10. de Freitas, L. F.; Hamblin, M. R., Antimicrobial photoinactivation with functionalized fullerenes. In *Nanobiomaterials in Antimicrobial Therapy*, Elsevier: 2016; pp 1-27.
11. Mfouo-Tynga, I. S.; Dias, L. D.; Inada, N. M.; Kurachi, C., Biophysical and Biological Features of Third Generation Photosensitizers Used in Anticancer Photodynamic Therapy. *Photodiagnosis and Photodynamic Therapy* **2021**, 102091.
12. Zhou, Z.; Song, J.; Nie, L.; Chen, X., Reactive oxygen species generating systems meeting challenges of photodynamic cancer therapy. *Chem. Soc. Rev.* **2016**, *45* (23), 6597-6626.
13. Gunaydin, G.; Gedik, M. E.; Ayan, S., Photodynamic Therapy—Current Limitations and Novel Approaches. *Frontiers in Chemistry* **2021**, *9*, 400.
14. Organization, W. H., Ionizing radiation, health effects and protective measures. *World Health Organization* **2016**.
15. Omeodu, M. D.; Utuh, B. N., Effect of cooperative learning strategy on secondary school physics students' understanding of the concept of radioactivity. *Galili, R., Mohammed, MA, Nwachukwu, CO (Eds.)* **2018**.
16. Stabin, M. G., *Radiation protection and dosimetry: an introduction to health physics*. Springer Science & Business Media: 2007.

17. Cline, B.; Delahunty, I.; Xie, J., Nanoparticles to mediate X-ray-induced photodynamic therapy and Cherenkov radiation photodynamic therapy. *Wiley Interdisciplinary Reviews: Nanomedicine and Nanobiotechnology* **2019**, *11* (2), e1541.
18. Wang, G. D.; Nguyen, H. T.; Chen, H.; Cox, P. B.; Wang, L.; Nagata, K.; Hao, Z.; Wang, A.; Li, Z.; Xie, J., X-Ray Induced Photodynamic Therapy: A Combination of Radiotherapy and Photodynamic Therapy. *Theranostics* **2016**, *6* (13), 2295-2305.
19. Larue, L.; Ben Mihoub, A.; Youssef, Z.; Colombeau, L.; Acherar, S.; Andre, J. C.; Arnoux, P.; Baros, F.; Vermandel, M.; Frochot, C., Using X-rays in photodynamic therapy: an overview. *Photochem. Photobiol. Sci.* **2018**, *17* (11), 1612-1650.
20. Tang, Y.; Hu, J.; Elmenoufy, A. H.; Yang, X., Highly Efficient FRET System Capable of Deep Photodynamic Therapy Established on X-ray Excited Mesoporous LaF₃:Tb Scintillating Nanoparticles. *ACS Appl. Mater. Interfaces* **2015**, *7* (22), 12261-9.
21. Wang, G. D.; Nguyen, H. T.; Chen, H.; Cox, P. B.; Wang, L.; Nagata, K.; Hao, Z.; Wang, A.; Li, Z.; Xie, J., X-ray induced photodynamic therapy: a combination of radiotherapy and photodynamic therapy. *Theranostics* **2016**, *6* (13), 2295.
22. Ni, D.; Ferreira, C. A.; Barnhart, T. E.; Quach, V.; Yu, B.; Jiang, D.; Wei, W.; Liu, H.; Engle, J. W.; Hu, P., Magnetic targeting of nanotheranostics enhances cerenkov radiation-induced photodynamic therapy. *Journal of the American Chemical Society* **2018**, *140* (44), 14971-14979.

23. Kamkaew, A.; Cheng, L.; Goel, S.; Valdovinos, H. F.; Barnhart, T. E.; Liu, Z.; Cai, W., Cerenkov Radiation Induced Photodynamic Therapy Using Chlorin e6-Loaded Hollow Mesoporous Silica Nanoparticles. *ACS Appl. Mater. Interfaces* **2016**, 8 (40), 26630-26637.
24. Ni, D.; Ferreira, C. A.; Barnhart, T. E.; Quach, V.; Yu, B.; Jiang, D.; Wei, W.; Liu, H.; Engle, J. W.; Hu, P.; Cai, W., Magnetic Targeting of Nanotheranostics Enhances Cerenkov Radiation-Induced Photodynamic Therapy. *J. Am. Chem. Soc.* **2018**, 140 (44), 14971-14979.
25. Cline, B.; Delahunty, I.; Xie, J., Nanoparticles to mediate X-ray-induced photodynamic therapy and Cherenkov radiation photodynamic therapy. *Wiley Interdiscip. Rev. Nanomed. Nanobiotechnol.* **2019**, 11 (2), e1541.
26. Pratz, G.; Kapp, D. S., Is Cherenkov luminescence bright enough for photodynamic therapy? *Nat. Nanotechnol.* **2018**, 13 (5), 354-354.
27. Ciarrocchi, E.; Belcari, N., Cerenkov luminescence imaging: physics principles and potential applications in biomedical sciences. *EJNMMI Phys.* **2017**, 4 (1), 14.
28. Shrestha, S.; Wu, J.; Sah, B.; Vanasse, A.; Cooper, L. N.; Ma, L.; Li, G.; Zheng, H.; Chen, W.; Antosh, M. P., X-ray induced photodynamic therapy with copper-cysteamine nanoparticles in mice tumors. *Proc. Natl Acad. Sci. USA* **2019**, 116 (34), 16823-16828.
29. Elmenoufy, A. H.; Tang, Y. a.; Hu, J.; Xu, H.; Yang, X., A novel deep photodynamic therapy modality combined with CT imaging established via X-ray stimulated silica-modified lanthanide scintillating nanoparticles. *Chem. Commun.* **2015**, 51 (61), 12247-12250.

30. Lan, G.; Ni, K.; Xu, R.; Lu, K.; Lin, Z.; Chan, C.; Lin, W., Nanoscale Metal–Organic Layers for Deeply Penetrating X-ray-Induced Photodynamic Therapy. *Angew. Chem. Int. Ed.* **2017**, *56* (40), 12102-12106.
31. Chen, H.; Sun, X.; Wang, G. D.; Nagata, K.; Hao, Z.; Wang, A.; Li, Z.; Xie, J.; Shen, B., LiGa₅O₈:Cr-based theranostic nanoparticles for imaging-guided X-ray induced photodynamic therapy of deep-seated tumors. *Mater. Horiz.* **2017**, *4* (6), 1092-1101.
32. Im, H.-J., Excretion and Clearance. In *Radionanomedicine: Combined Nuclear and Nanomedicine*, Lee, D. S., Ed. Springer International Publishing: Cham, 2018; pp 347-368.
33. Khlebtsov, N.; Dykman, L., Biodistribution and toxicity of engineered gold nanoparticles: a review of in vitro and in vivo studies. *Chem. Soc. Rev.* **2011**, *40* (3), 1647-71.
34. Yong, K. T.; Law, W. C.; Hu, R.; Ye, L.; Liu, L.; Swihart, M. T.; Prasad, P. N., Nanotoxicity assessment of quantum dots: from cellular to primate studies. *Chem. Soc. Rev.* **2013**, *42* (3), 1236-50.
35. Lee, W.; Im, H. J., Theranostics Based on Liposome: Looking Back and Forward. *Nucl. Med. Mol. Imaging* **2019**, *53* (4), 242-246.
36. Mallick, S.; Choi, J. S., Liposomes: versatile and biocompatible nanovesicles for efficient biomolecules delivery. *J. Nanosci. Nanotechnol.* **2014**, *14* (1), 755-65.
37. Küçük, C.; Jiang, B.; Hu, X.; Zhang, W.; Chan, J. K.; Xiao, W.; Lack, N.; Alkan, C.; Williams, J. C.; Avery, K. N., Activating mutations of STAT5B and STAT3 in lymphomas derived from $\gamma\delta$ -T or NK cells. *Nature communications* **2015**, *6* (1), 1-12.

38. Bunzli, J. C., Benefiting from the unique properties of lanthanide ions. *Acc. Chem. Res.* **2006**, *39* (1), 53-61.
39. Chen, Y.; Guo, W.; Ye, Z.; Wang, G.; Yuan, J., A europium(III) chelate as an efficient time-gated luminescent probe for nitric oxide. *Chem. Commun.* **2011**, *47* (22), 6266-8.
40. Song, B.; Wang, G.; Tan, M.; Yuan, J., A Europium(III) Complex as an Efficient Singlet Oxygen Luminescence Probe. *J. Am. Chem. Soc.* **2006**, *128* (41), 13442-13450.
41. Binnemans, K., Lanthanide-Based Luminescent Hybrid Materials. *Chem. Rev.* **2009**, *109* (9), 4283-4374.
42. Nishioka, T.; Yuan, J.; Yamamoto, Y.; Sumitomo, K.; Wang, Z.; Hashino, K.; Hosoya, C.; Ikawa, K.; Wang, G.; Matsumoto, K., New Luminescent Europium(III) Chelates for DNA Labeling. *Inorg. Chem.* **2006**, *45* (10), 4088-4096.
43. Berezin, M. Y.; Achilefu, S., Fluorescence lifetime measurements and biological imaging. *Chem. Rev.* **2010**, *110* (5), 2641-2684.
44. Selvin, P. R., Principles and biophysical applications of lanthanide-based probes. *Annu. Rev. Biophys. Biomol. Struct.* **2002**, *31*, 275-302.
45. Selvin, P. R.; Hearst, J. E., Luminescence energy transfer using a terbium chelate: improvements on fluorescence energy transfer. *Proc. Natl. Acad. Sci. U.S.A* **1994**, *91* (21), 10024-10028.
46. Hemmila, I.; Laitala, V., Progress in lanthanides as luminescent probes. *J. Fluoresc.* **2005**, *15* (4), 529-42.

47. Pandey, P.; Kurchania, R.; Haque, F., Optical Studies of Europium-Doped ZnO Nanoparticles Prepared by Sol–Gel Technique. *J. Adv. Phys.* **2014**, *3*, 104-110.
48. Ramasamy, S.; Yogamalar, N.; Elanchezhian, J.; Joseyphus, J.; Bose, A., Structural and optical properties of europium doped yttrium oxide nanoparticles for phosphor applications. *J. Alloys Compd.* **2010**, *496*, 472-477.
49. Kumar, A.; Babu, S.; Karakoti, A. S.; Schulte, A.; Seal, S., Luminescence Properties of Europium-Doped Cerium Oxide Nanoparticles: Role of Vacancy and Oxidation States. *Langmuir* **2009**, *25* (18), 10998-11007.
50. Chen, H.; Wang, G. D.; Chuang, Y.-J.; Zhen, Z.; Chen, X.; Biddinger, P.; Hao, Z.; Liu, F.; Shen, B.; Pan, Z.; Xie, J., Nanoscintillator-Mediated X-ray Inducible Photodynamic Therapy for In Vivo Cancer Treatment. *Nano Lett.* **2015**, *15* (4), 2249-2256.
51. Hsu, C.-C.; Lin, S.-L.; Chang, C. A., Lanthanide-Doped Core–Shell–Shell Nanocomposite for Dual Photodynamic Therapy and Luminescence Imaging by a Single X-ray Excitation Source. *ACS Appl. Mater. Interfaces* **2018**, *10* (9), 7859-7870.
52. Pratt, E. C.; Shaffer, T. M.; Zhang, Q.; Drain, C. M.; Grimm, J., Nanoparticles as multimodal photon transducers of ionizing radiation. *Nat. Nanotechnol.* **2018**, *13* (5), 418-426.
53. Sun, C.; Pratz, G.; Carpenter, C. M.; Liu, H.; Cheng, Z.; Gambhir, S. S.; Xing, L., Synthesis and radioluminescence of PEGylated Eu(3+) -doped nanophosphors as bioimaging probes. *Adv. Mater.* **2011**, *23* (24), H195-H199.

54. Hansen, P.-A.; Granerød, C. S.; Prytz, Ø.; Nilsen, O., Controlling luminescence and quenching mechanisms in subnanometer multilayer structure of europium titanium oxide thin films. *Journal of Luminescence* **2019**, *215*, 116618.
55. Ronda, C., Luminescence loss mechanisms. *Journal of Luminescence* **2009**, *129* (12), 1824-1826.
56. Gedanken, A.; Reisfeld, R.; Sominski, L.; Zhong, Z.; Kolytyn, Y.; Panczer, G.; Gaft, M.; Minti, H., Time-dependence of luminescence of nanoparticles of Eu₂O₃ and Tb₂O₃ deposited on and doped in alumina. *Applied Physics Letters* **2000**, *77* (7), 945-947.
57. Larsson, K.; Mezyk, S. P., Employing Luminescence to Determine Eu-DTPA Complex Formation Rate Constants in Lactate and Citrate Media: Experiment and Aggregate-Species Kinetic Modelling. *Solvent Extraction and Ion Exchange* **2019**, *37* (1), 53-64.
58. Nishioka, T.; Yuan, J.; Yamamoto, Y.; Sumitomo, K.; Wang, Z.; Hashino, K.; Hosoya, C.; Ikawa, K.; Wang, G.; Matsumoto, K., New Luminescent Europium(III) Chelates for DNA Labeling. *Inorganic Chemistry* **2006**, *45* (20), 8460-8460.
59. Seitz, M.; Moore, E. G.; Ingram, A. J.; Muller, G.; Raymond, K. N., Enantiopure, Octadentate Ligands as Sensitizers for Europium and Terbium Circularly Polarized Luminescence in Aqueous Solution. *Journal of the American Chemical Society* **2007**, *129* (50), 15468-15470.
60. Heyduk, T., Luminescence resonance energy transfer analysis of RNA polymerase complexes. *Methods* **2001**, *25* (1), 44-53.

61. Kokko, T. Lanthanide Chelates as Donors in Fluorescence Resonance Energy Transfer: Exciting Prospects for Bioaffinity Assay Detection. University of Turku, 2009.
62. Hu, D.; Sheng, Z.; Zhu, M.; Wang, X.; Yan, F.; Liu, C.; Song, L.; Qian, M.; Liu, X.; Zheng, H., Förster Resonance Energy Transfer-Based Dual-Modal Theranostic Nanoprobe for In Situ Visualization of Cancer Photothermal Therapy. *Theranostics* **2018**, 8 (2), 410.
63. Jung, S.; Kim, T.; Lee, W.; Kim, H.; Kim, H. S.; Im, H. J.; Ye, S. J., Dynamic in vivo X-ray Fluorescence Imaging of Gold in Living Mice Exposed to Gold Nanoparticles. *IEEE Trans. Med. Imaging* **2019**.
64. Jones, G.; Bradshaw, D., Resonance energy transfer: From fundamental theory to recent applications. *Frontiers in Physics* **2019**, 7.
65. Niccoli Asabella, A.; Cascini, G. L.; Altini, C.; Paparella, D.; Notaristefano, A.; Rubini, G., The copper radioisotopes: a systematic review with special interest to ^{64}Cu . *Biomed. Res. Int.* **2014**, 2014, 786463-786463.
66. Love, C.; Din, A. S.; Tomas, M. B.; Kalapparambath, T. P.; Palestro, C. J., Radionuclide Bone Imaging: An Illustrative Review. *Radiographics* **2003**, 23 (2), 341-358.
67. Taylor, A. T., Radionuclides in nephrourology, part 1: Radiopharmaceuticals, quality control, and quantitative indices. *J. Nucl. Med.* **2014**, 55 (4), 608-615.
68. Baggish, A. L.; Boucher, C. A., Radiopharmaceutical agents for myocardial perfusion imaging. *Circulation* **2008**, 118 (16), 1668-74.
69. Kotagiri, N.; Cooper, M. L.; Rettig, M.; Egbulefu, C.; Prior, J.; Cui, G.; Karmakar, P.; Zhou, M.; Yang, X.; Sudlow, G.; Marsala, L.; Chanswangphuwana,

- C.; Lu, L.; Habimana-Griffin, L.; Shokeen, M.; Xu, X.; Weilbaecher, K.; Tomasson, M.; Lanza, G.; DiPersio, J. F.; Achilefu, S., Radionuclides transform chemotherapeutics into phototherapeutics for precise treatment of disseminated cancer. *Nat. Commun.* **2018**, *9* (1), 275.
70. Unger, E.; Cardenas, D.; Zerella, A.; Fajardo, L. L.; Tilcock, C., Biodistribution and clearance of liposomal gadolinium-DTPA. *Invest. Radiol.* **1990**, *25* (6), 638-44.
71. Chatterjee, D. K.; Fong, L. S.; Zhang, Y., Nanoparticles in photodynamic therapy: an emerging paradigm. *Adv. Drug. Deliv. Rev.* **2008**, *60* (15), 1627-37.
72. Jin, C. S.; Zheng, G., Liposomal nanostructures for photosensitizer delivery. *Lasers Surg. Med.* **2011**, *43* (7), 734-748.
73. Wilhelm, S.; Tavares, A. J.; Dai, Q.; Ohta, S.; Audet, J.; Dvorak, H. F.; Chan, W. C. W., Analysis of nanoparticle delivery to tumours. *Nat. Rev. Mater.* **2016**, *1*, 16014.
74. de Souza, A. L. R.; LaRochelle, E.; Marra, K.; Gunn, J.; Davis, S. C.; Samkoe, K. S.; Chapman, M. S.; Maytin, E. V.; Hasan, T.; Pogue, B. W., Assessing daylight & low-dose rate photodynamic therapy efficacy, using biomarkers of photophysical, biochemical and biological damage metrics in situ. *Photodiagn. Photodyn.* **2017**, *20*, 227-233.
75. Conti, M.; Eriksson, L., Physics of pure and non-pure positron emitters for PET: a review and a discussion. *EJNMMI Phys.* **2016**, *3* (1), 8-8.
76. Kotagiri, N.; Sudlow, G. P.; Akers, W. J.; Achilefu, S., Breaking the depth dependency of phototherapy with Cerenkov radiation and low-radiance-responsive nanophotosensitizers. *Nat. Nanotechnol.* **2015**, *10*, 370.

77. Sahan, A. Z.; Hazra, T. K.; Das, S., The pivotal role of DNA repair in infection mediated-inflammation and cancer. *Frontiers in microbiology* **2018**, *9*, 663.
78. Jackson, S. P.; Bartek, J., The DNA-damage response in human biology and disease. *Nature* **2009**, *461* (7267), 1071-1078.
79. O'Connor, M. J., Targeting the DNA damage response in cancer. *Molecular cell* **2015**, *60* (4), 547-560.
80. Huang, R.; Zhou, P.-K., DNA damage repair: historical perspectives, mechanistic pathways and clinical translation for targeted cancer therapy. *Signal Transduction and Targeted Therapy* **2021**, *6* (1), 1-35.
81. Strosberg, J.; El-Haddad, G.; Wolin, E.; Hendifar, A.; Yao, J.; Chasen, B.; Mittra, E.; Kunz, P. L.; Kulke, M. H.; Jacene, H.; Bushnell, D.; O'Dorisio, T. M.; Baum, R. P.; Kulkarni, H. R.; Caplin, M.; Lebtahi, R.; Hobday, T.; Delpassand, E.; Van Cutsem, E.; Benson, A.; Srirajaskanthan, R.; Pavel, M.; Mora, J.; Berlin, J.; Grande, E.; Reed, N.; Seregni, E.; Öberg, K.; Lopera Sierra, M.; Santoro, P.; Thevenet, T.; Erion, J. L.; Ruzsiewski, P.; Kwekkeboom, D.; Krenning, E., Phase 3 Trial of ¹⁷⁷Lu-Dotatate for Midgut Neuroendocrine Tumors. *N. Engl. J. Med.* **2017**, *376* (2), 125-135.
82. von Eyben, F. E.; Roviello, G.; Kiljunen, T.; Uprimny, C.; Virgolini, I.; Kairemo, K.; Joensuu, T., Third-line treatment and (177)Lu-PSMA radioligand therapy of metastatic castration-resistant prostate cancer: a systematic review. *Eur. J. Nucl. Med. Mol. Imaging* **2018**, *45* (3), 496-508.
83. Hofman, M. S.; Violet, J.; Hicks, R. J.; Ferdinandus, J.; Thang, S. P.; Akhurst, T.; Iravani, A.; Kong, G.; Ravi Kumar, A.; Murphy, D. G.; Eu, P.; Jackson, P.; Scalzo, M.; Williams, S. G.; Sandhu, S., [(177)Lu]-PSMA-617

radionuclide treatment in patients with metastatic castration-resistant prostate cancer (LuPSMA trial): a single-centre, single-arm, phase 2 study. *Lancet Oncol.* **2018**, *19* (6), 825-833.

84. Haley, T. J.; Komesu, N.; Colvin, G.; Koste, L.; Upham, H. C., Pharmacology and Toxicology of Europium Chloride. *Journal of Pharmaceutical Sciences* **1965**, *54* (4), 643-645.

85. Ogawa, Y.; Suzuki, S.; Naito, K.; Saito, M.; Kamata, E.; Hirose, A.; Ono, A.; Kaneko, T.; Chiba, M.; Inaba, Y.; et al., Toxicity study of europium chloride in rats. *J Environ Pathol Toxicol Oncol* **1995**, *14* (1), 1-9.

86. Rim, K. T.; Koo, K. H.; Park, J. S., Toxicological evaluations of rare earths and their health impacts to workers: a literature review. *Saf Health Work* **2013**, *4* (1), 12-26.

87. Weinmann, H. J.; Brasch, R. C.; Press, W. R.; Wesbey, G. E., Characteristics of gadolinium-DTPA complex: a potential NMR contrast agent. *AJR Am J Roentgenol* **1984**, *142* (3), 619-24.

88. Wagner, A.; Vorauer-Uhl, K., Liposome technology for industrial purposes. *Journal of drug delivery* **2011**, *2011*.

89. Liu, Z.; Ma, T.; Liu, H.; Jin, Z.; Sun, X.; Zhao, H.; Shi, J.; Jia, B.; Li, F.; Wang, F., ¹⁷⁷Lu-labeled antibodies for EGFR-targeted SPECT/CT imaging and radioimmunotherapy in a preclinical head and neck carcinoma model. *Molecular pharmaceutics* **2014**, *11* (3), 800-807.

90. Shih, B.-B.; Chang, Y.-F.; Cheng, C.-C.; Yang, H.-J.; Chang, K.-W.; Ho, A.-S.; Lin, H.-C.; Yeh, C.; Chang, C.-C., SPECT imaging evaluation of ¹¹¹indium-chelated cetuximab for diagnosing EGFR-positive tumor in an HCT-

15-induced colorectal xenograft. *Journal of the Chinese Medical Association* **2017**, *80* (12), 766-773.

91. Guo, Y.; Parry, J. J.; Laforest, R.; Rogers, B. E.; Anderson, C. J., The role of p53 in combination radioimmunotherapy with ⁶⁴Cu-DOTA-cetuximab and cisplatin in a mouse model of colorectal cancer. *Journal of Nuclear Medicine* **2013**, *54* (9), 1621-1629.

92. Lee, W.; Jeon, M.; Choi, J.; Oh, C.; Kim, G.; Jung, S.; Kim, C.; Ye, S.-J.; Im, H.-J., Europium-diethylenetriaminepentaacetic acid loaded radioluminescence liposome nanoplatform for effective radioisotope-mediated photodynamic therapy. *ACS nano* **2020**, *14* (10), 13004-13015.

93. Sgouros, G.; Bodei, L.; McDevitt, M. R.; Nedrow, J. R., Radiopharmaceutical therapy in cancer: clinical advances and challenges. *Nature Reviews Drug Discovery* **2020**, *19* (9), 589-608.

94. Wu, T.-J.; Chiu, H.-Y.; Yu, J.; Cautela, M. P.; Sarmiento, B.; das Neves, J.; Catala, C.; Pazos-Perez, N.; Guerrini, L.; Alvarez-Puebla, R. A., Nanotechnologies for early diagnosis, in situ disease monitoring, and prevention. In *Nanotechnologies in preventive and regenerative medicine*, Elsevier: 2018; pp 1-92.

95. Ahmadzadehfar, H.; Eppard, E.; Kürpig, S.; Fimmers, R.; Yordanova, A.; Schlenkhoff, C. D.; Gärtner, F.; Rogenhofer, S.; Essler, M., Therapeutic response and side effects of repeated radioligand therapy with ¹⁷⁷Lu-PSMA-DKFZ-617 of castrate-resistant metastatic prostate cancer. *Oncotarget* **2016**, *7* (11), 12477.

96. Kendi, A. T.; Halfdanarson, T. R.; Packard, A.; Dundar, A.; Subramaniam, R. M., Therapy With ¹⁷⁷Lu-DOTATATE: clinical implementation

and impact on care of patients with neuroendocrine tumors. *American Journal of Roentgenology* **2019**, 213 (2), 309-317.

Abstract in Korean

PDT (Photodynamic Therapy, 광역동 치료)는 기존 치료법보다 선택성이 높고 부작용이 적은 효과적인 항암 전략을 가진 치료법이고 광감작제(photosensitizer, PS)와 광감작제를 자극하여 활성산소(ROS) 생성을 통해 국소적으로 표적 종양 조직을 제거할 수 있는 빛에 의해 그 치료가 이루어진다. 그러나 조사되는 빛의 경우 피부 투과를 위해 보통 적색의 가시광선이나 근적외선이 주로 사용되는데 이 광원들의 경우 빛의 투과도가 피부로부터 1 cm가 채 되지 않기 때문에 PDT의 광범위한 임상 유용성 및 적용에 한계를 가지고 있다. 이러한 기존 PDT의 한계점을 극복하기 위해 방사선 기반 PDT에 대한 연구가 수년간 진행되고 있다. 최근 보고에 따르면 방사성 동위원소 기반 Cerenkov 발광 유도 PDT는 기존 PDT의 조직 침투 한계를 극복하고 외부 방사선 조사 없이도 자체 플랫폼으로도 치료가 가능한 특징점을 가지고 있다. 하지만 이 치료법은 Cerenkov 발광 강도가 상대적으로 낮아 그 효율성에 대해 논란이 되고 있다.

따라서 본 연구의 첫번째 파트 (Chapter 2)를 통해 효과적인 생체 내 이미징 및 방사선 발광 유도 PDT를 위해 방사성 동위원소의 이온화 방사선을 활용하는 방사성 표지 DTPA 킬레이트화된 Eu^{3+} (Eu-DTPA)/광감제(PS)가 탑재된 리포솜 나노플랫폼 (Eu/PS-lipo)을 개발하였다. 전리방사선의 신틸레이션을 위해 고안한 리포솜 구조에 Eu-DTPA 를 내재한 결과, 일반적으로 사용되는 신틸레이팅 나노입자인 Eu_2O_3 나노 입자보다 약 7배 높은 방사선 발광 강도를 나타냈다. 본

연구에서 개발한 방사선발광 리포솜 나노플랫폼의 Eu-DTPA에서 VBBO로의 방사선발광 에너지 전달(RET)은 Cerenkov 발광 에너지 전달(CLET)보다 6배 더 높은 에너지 전달 효율을 보였다. ^{64}Cu 로 방사성 표지된 Eu/VBBO lipo (^{64}Cu -Eu/VBBO lipo)에 대한 생체 내 양전자 방출 단층 촬영을 한 결과 향상된 투과성 및 체류 효과 (enhanced permeability and retention effect, EPR effect)에 의해 최대 19.3%ID/g의 높은 종양 섭취를 보였다. 이어서 실시한 in vitro 및 in vivo 치료 효과 검증 연구에서 ^{64}Cu -Eu/VBBO lipo를 사용한 PDT가 본 연구에서 Cerenkov 발광 유도 PDT에 해당하는 ^{64}Cu -VBBO lipo를 사용한 PDT 효과보다 훨씬 더 높은 치료 효과를 보였다는 것을 확인하였다.

두번째 파트 (Chapter 3)에서는 기존에 개발했던 리포솜 나노플랫폼 (^{64}Cu -Eu/VBBO lipo)의 잠재적 한계인 정상 장기への 손상 최소화를 위한 개선 연구를 진행하였다. 본 연구의 효과적인 PDT 효과를 위해 두 종류의 나노 프로브를 사용한 조합적 PDT 시스템을 고안하였다: 1) 방사성 동위원소가 배제된 리포솜 나노플랫폼 (Eu/VBBO lipo), 2) ^{177}Lu 방사성 표지 항체 (트라스투주맵, 세톡시맵). Eu/VBBO lipo는 생체 유사 조건에서 높은 분산 안정도와 수용액 상에서의 높은 균일도를 보였다. 항체들의 경우, 각 항체 특이 암세포주에 대해 우수한 특이적 결합능을 보였다. 다음으로, 리포솜과 방사성 표지 항체의 조합적 PDT 시스템에서의 방사성 발광은 ^{177}Lu 에 의한 Cerenkov luminescence 보다 대략 6배 높은 세기의 발광 효과를 보였다. 더 나아가, Eu^{3+} 과

VBBO 양에 따른 Eu^{3+} 에서 VBBO로의 방사선발광의 에너지 전달 효율을 확인하는 연구를 진행하였고, Eu^{3+} : 0.8 mg 과 VBBO: 2.56 μg 의 조건에서 약 50%의 최대 에너지 전달 효율을 보였다. 생체 내 형광 영상 및 핵의학 영상을 촬영한 결과, Eu/VBBO lipo 와 항체들은 대해 마우스 암 모델에서 각각 수동 표적능과 능동 표적능에 의한 상당한 종양에의 섭취를 보였다. 특히 ^{64}Cu 를 표지한 PET 영상을 기반으로 하였을 때, Eu/VBBO lipo 와 세특시맵은 각각 최대 17.1 %ID/g 과 25.1 %ID/g까지 매우 높은 종양에의 섭취를 보였다. 생체 내 PDT 효과에 대한 연구를 진행했을 때, 조합적 PDT 시스템에 의한 치료 효과가 고용량의 ^{177}Lu -트라스투주맵에 의한 치료보다 약 3.5배 더 높은 것으로 나타났다(치료 효과: 67% 대 19%). 이어서 조합적 PDT 시스템의 생체 외 PDT 효과를 검증하기 위해 CT-26 이종이식 마우스 암 모델에서 연구를 진행하였다. 하지만 생체 외 조건에서의 연구에서 조합적 PDT 시스템이 우수한 효과를 보였음에도 생체 내 PDT 효과는 대조군과 비교하였을 때 그 효과가 미비하였다. 위와 같은 시험관 내 실험과 생체 내 실험의 차이에 대한 정확한 원인을 찾고 이 새로운 치료법의 생체 내 효능을 개선하기 위한 연구가 앞으로 더 필요하다. 종양에 대한 효과적 치료 효과와 정상 장기 손상의 최소화를 위한 체내 치료 실험 연구에는 개선의 여지가 있지만 본 연구는 높은 종양 표적화 및 방사성 동위원소로부터의 효율적인 에너지 전달 능력을 갖는 방사선 발광 리포솜 나노플랫폼을 확립함으로써 PDT의 광범위한 임상 적용이 가능할 것이라 전망된다.

주요어 : 광역학 요법, 방사선 발광, 섬광, 유로퓸, 리포솜, 양전자 방출
단층 촬영

학 번 : 2018-38662